NONLINEAR ANALYSIS OF HIGH-STRENGTH CONCRETE SLABS

CENTRE FOR NEWFOUNDLAND STUDIES

TOTAL OF 10 PAGES ONLY
MAY BE XEROXED

(Without Author's Permission)

ZHIWEI CHEN

CENTRE FOR NFLD. STUDIES
JUN 20 1994
MEMORIAL UNIVERSITY
OF NEWFOUNDLAND

Nonlinear Analysis of High-Strength Concrete Slabs

By

© Zhiwei Chen, B.Sc.(Eng.), M.Sc.(Eng.)

A thesis submitted to the School of Graduate Studies in partial fulfillment of the requirements for the Degree of Master of Engineering

March 1993

Faculty of Engineering and Applied Science

Memorial University of Newfoundland

St. John's Newfoundland Canada

To **Rong Yu**

Abstract

High-strength concrete slabs are frequently used in various structural engineering systems and a wide variety of civil engineering applications. A research program on the structural behaviour of such slabs is being carried out both experimentally and numerically at Memorial University of Newfoundland (M.U.N.). The work reported herein includes the experimental investigation on the tensile behaviour of high-strength concrete and finite element (F.E.) analysis of its slabs. The emphasis is placed upon the importance of the realistic material properties and the need of a valid concrete model in the F.E. analysis. Particular attention has been focused on the post-cracking tensile behaviour of high-strength concrete.

The complete load-deformation behaviour of high-strength concrete in direct tension, including post-cracking softening response, was obtained by developing direct tension test technique. The test measurements were then characterized into a rational tension softening model. The understanding of the unique tension softening nature of high-strength concrete was enhanced by comparison to that of normal strength concrete in terms of fracture energy, mechanical properties and entire load-deformation response. In addition, the effect of the cold ocean water on the tensile properties of high-strength concrete was examined. The variability and relations of tensile strengths and compressive strength were also studied.

Appropriate representation of post-cracking behaviour of reinforced high-strength concrete was developed for the F.E. analysis of its slabs. The developed models and measured stress-strain characteristics of high-strength concrete and reinforcing bars

were then incorporated into a proposed plasticity-based concrete model implemented in the context of the 8-node quadrilateral shear-flexible thick shell element. The material model allows realistic concrete strain softening after both cracking and crushing. The validity of the model was established by comparison of F.E. numerical predictions to experimental results of sixteen slabs tested at M.U.N. The model performed satisfactorily in all the cases, with respect to the entire load-deflection response, ultimate load carrying capacity, ductility, and failure mode.

The F.E. model was then used to carry out a parametric study to examine the structural behaviour of reinforced high-strength concrete slabs. The parameters under investigation include various material properties, slab boundary conditions, loading stub-column, and loading type and sequence. In addition, a tension stiffening model was approximately formulated, based on the fracture energy concept and comparison of F.E. predictions to experimental results of the tested slabs. The importance of the concrete tension stiffening behaviour was highlighted in the F.E. analysis of the slab selected.

Acknowledgements

The author wishes to express his deep gratitude and appreciation to Dr. H. Marzouk, Professor of civil engineering with Memorial University, for his supervision and guidance. Financial support in the form of graduate fellowship and teaching assistantship from Memorial University is also gratefully acknowledged.

Special thanks are due to Amgad, Austin, Calvin and Ron for their support in the laboratory work.

Last, but not the least, the author would like to take this chance to express his profound gratitude to all his family members, specifically his parents, for their permanent support and affection.

Contents

List of Figures

List of Tables

List of Symbols

a	=	side dimension of square slabs
A_w	=	strain energy density, the area under the complete tensile stress-strain diagram of reinforced high-strength concrete
A_{wi}	=	strain energy density, the area under the complete tensile stress-strain diagram of plain high-strength concrete
d_{max}	=	maximum nominal aggregate size used in the concrete mix
E_c	=	secant modulus of elasticity
E_o	=	initial modulus of elasticity
E_p	=	secant modulus of elasticity at peak stress
E_t	=	initial tangential modulus of concrete
E_{ts}	=	tagent modulus of elasticity associated with the direction normal to the crack (Eq. 5.19)
F_c	=	concrete compression yield surface (Eq. 5.3)
F_t	=	concrete tension yield surface (Eq. 5.14)
G	=	shear modulus of concrete
G_o	=	initial shear modulus of concrete
G_f	=	fracture energy required to form a unit area of crack surface
K_{IC}	=	critical stress intensity factor

h = slab thickness

HS = high-strength concrete

$\mathbf{I}$ = unity matrix

I_m = relative magnitude of in-plane axial load

k = material constant in Eq. 4.6

n = positive direction normal to shell element reference surface

NS = normal strength concrete

P = axial in-plane load along two opposite slab edges

p, δ = concrete tensile load and deformation

p = concrete first stress invariant

q = concrete second stress invariant

Q = lateral load at slab center

Q_u = ultimate lateral load at slab center

r = failure stress ratio ($r = \sigma_2/f'_t$, Eq. 5.15)

r_f = failure stress ratio ($r_f = f'_{bc}/f'_c$)

r_{tc} = failure stress ratio ($r_{tc} = f'_t/f'_c$)

r_ϵ = plastic strain ratio ($r_\epsilon = \epsilon_{pb}/\epsilon_p$)

$\mathbf{S}$ = deviatoric stress components of the stress tensor σ

S_1 = local axis 1 of shell element reference surface

S_2 = local axis 2 of shell element reference surface

u = concrete displacement as shown in Fig. 5.3

u^{el} = concrete elastic displacement as defined in Fig. 5.3

u^{cr} = concrete crack opening displacement as defined in Fig. 5.3

f_c = concrete compressive stress

f'_{bc} = concrete failure principal stress under equal biaxial stresses

f'_c = ultimate concrete compressive strength

f'_{ct} = splitting tensile strength

f'_r = modulus of rupture

f_t = concrete tensile stress

f'_t = ultimate concrete tensile strength

f_y = steel yield strength

f_s = steel stress

df_n = direct stress rate in the direction parallel to the crack

df_{tn} = shear stress associated with the cracked plane

ϵ_s = steel strain

ϵ_c = concrete compressive strain

ϵ_{co} = concrete compressive strain at f'_c

ϵ_{cr} = concrete cracking strain

ϵ_{max} = maximum tensile effective (cracking) strain

ϵ_p = concrete plastic strain in a monotonically loaded uniaxial compression specimen

ϵ_{pb} = concrete plastic strain in a monotonically loaded biaxial compression specimen

ϵ_t = concrete tensile strain

ϵ_{to} = concrete tensile strain at f_t'

$\bar{\epsilon}_t$ = concrete average crack opening strain as defined in Eq. 5.25

ϵ_{sr} = total average shear-effective crack opening strain in concrete as defined in Eq. 5.24

ϵ_{ts}^u = ultimate tensile-effective strain in concrete

ϵ_{sr}^u = ultimate shear-effective tensile strain in concrete

$d\epsilon$ = total strain rate of concrete

$d\epsilon_e$ = elastic strain rate of concrete

$d\epsilon_{et}$ = elastic strain rate for crack detection

$d\epsilon_n$ = direct strain rate in the direction parallel to the crack

$d\epsilon_p$ = plastic strain rate of concrete

$d\epsilon_{pt}$ = plastic strain rate associated with crack detection surface

δ_{max} = maximum tensile effective (cracking) deformation

δ_p = concrete tensile deformation at peak load

δ_t = concrete tensile deformation

Δ_u = deflection at slab center at the ultimate load

D = deflection at slab center

ω = crack width

ω_c = width of fracture process zone

ω_o = crack width when f_t reaches zero

ω_t = $\omega+\delta_p$

σ = stress tensor of concrete

σ_1 = concrete first principal stress

σ_2 = concrete second principal stress

τ_c = concrete hardening parameter in compression

ρ = reinforcement ratio

ϱ = linear shear degradation function

ϱ^{close} = shear degradation factor when crack closes

α = material parameter in Eq. 7.2

β = material parameter in Eq. 7.2

θ = rebar orientation (angle)

λ = material constant in Eq. 4.6

$d\lambda_c$ = scalar proportionality factor (Eq. 5.8)

$d\lambda_t$ = scalar proportionality factor (Eq. 5.16)

Chapter 1

Introduction

1.1 High-strength structural concrete

High-strength structural concrete is a state-of-the-art material. Its development has been gradual over many years. In recent years, the application of high-strength structural concrete has increased, and now it has been used in many parts of the world as a result of recent developments in material technology and an ever growing demand. The use of concrete superstructures in long span cable-stayed bridges such as East Huntington, W.V., bridge over Ohio River would not have taken place without the availability of high-strength concrete.

At the present, high-strength concrete has been widely used in exploratory drilling structures, marine structures, tall buildings, grandstand roofs and parking garages. It has also been specified for applications in warehouses, bridge deck overlays, dam spillways, and heavy duty industrial floors. In these applications, high-strength structural concrete is being used to provide a concrete with improved resistance to chemical attack, better abrasion resistance, improved freeze-thaw durability, reduced permeability, increased modulus of elasticity and decreased creep and shrinkage. Hence, high-strength structural concrete offers great promise for problems associated with

unconventional structures and structures in severe adverse environment and in heavy duty construction.

A gravity based structure utilizing high-strength structural concrete has been recommended for the Hibernia oil development off the eastern coast of Newfoundland (Mobil, 1985), as illustrated in Fig. 1.1.

High-strength concrete slabs supported on four edges and loaded transversely and axially frequently occur in various structural systems. High-strength concrete slabs are widely used in offshore applications. It has been proven that offshore high-strength concrete platforms have survived the harsh North Sea environment for the past decade. Offshore structures frequently have a concrete perimeter wall normally designed to resist the impact of ice and ocean wave on the structure (Cammaert and Muggeridge, 1988). Both flat and curved exterior walls have been used. Thus, the concrete plates and shells represents the most predominant structural element in the walls of concrete offshore platforms (Fig. 1.2b).

In many cases, the inplane load is small with respect to the lateral load and can often be neglected. In addition, the two loads can be treated separately when the slenderness of the slab is not critical. However, there are some situations such as offshore structures, bridges decks, etc. (Figs. 1.1-1.2) where the two loading types have to be taken into account simultaneously. Transverse loads can be applied as point loads, hydrostatic pressures or uniform pressures whereas inplane loads are usually uniformly distributed along slab edges, and can be either uniaxial or biaxial.

The sequence of application of combined inplane and lateral loads varies. However two extreme cases can be identified: the inplane load may be applied first and kept constant followed by a variable lateral load or, inversely, the lateral load may be

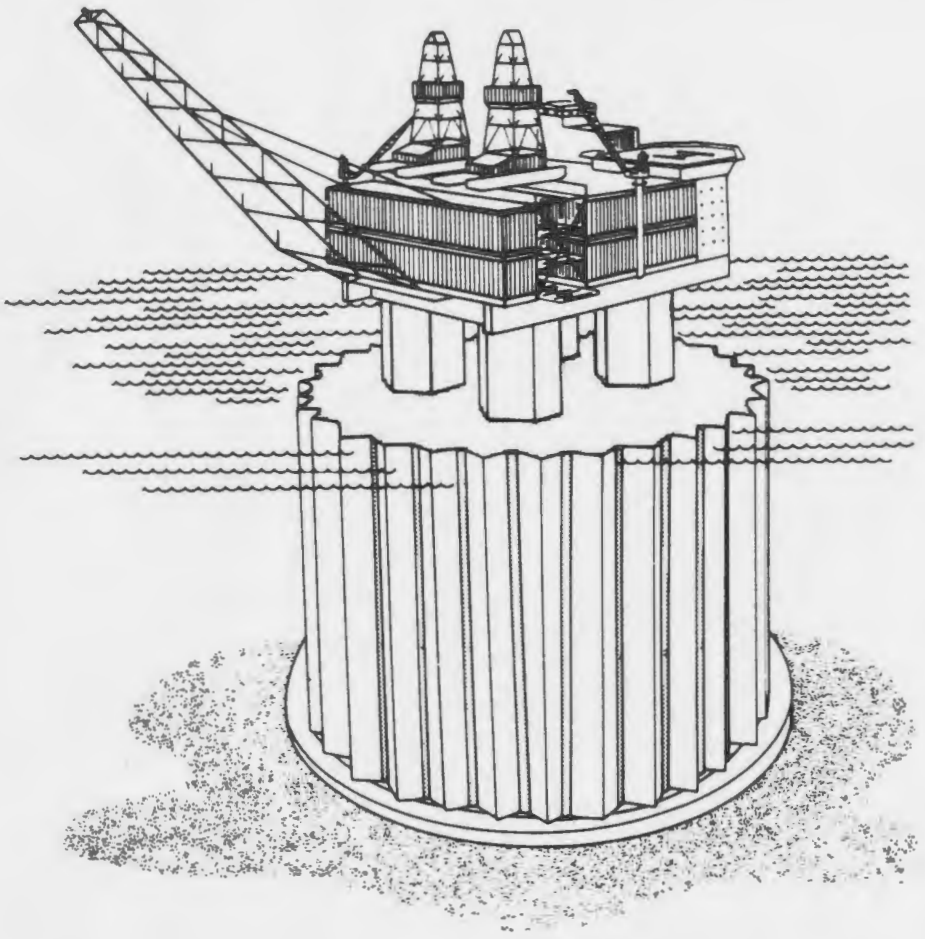

Figure 1.1: Proposed gravity based concrete cylindrical large-diameter oil production platform for the Hibernia Development (Mobil, 1985)

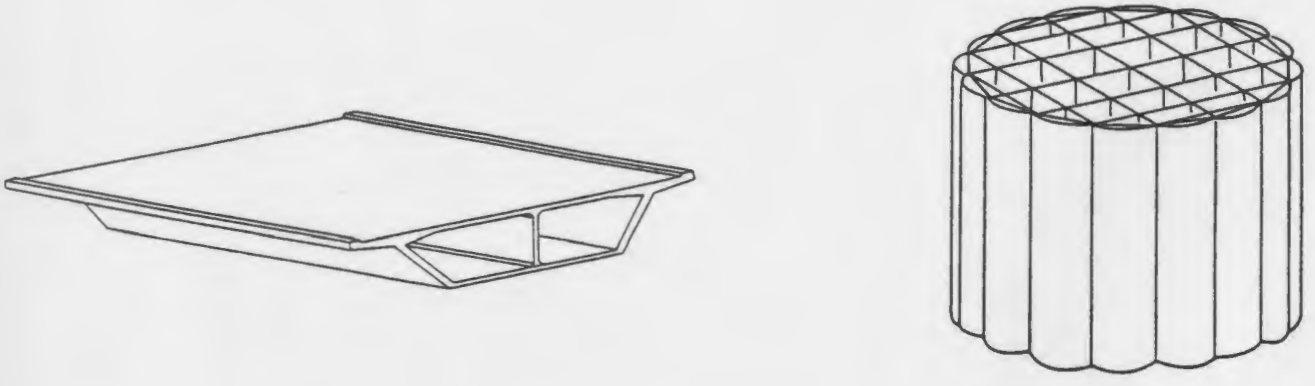

(a) (b)

Figure 1.2: Examples of typical structural elements of high-strength concrete (a) bridge deck (b) curved (shell) wall in the "Honeycomb" offshore structures

applied first and maintained constant followed by a variable inplane load. In between the two extreme cases, any load application sequence can be imagined. The interaction between the two load types is a function of relative importance of these loads and slab response to their combination. The types of slab failure can also vary, being either by instability for slender slabs with large axial loads, or by material failure, which would be expected in stocky slabs or in slabs with high lateral load.

1.2 Finite element analysis of reinforced concrete structures

In the past, nonlinear solution techniques were usually employed in the design and analysis of unusual structures, such as offshore structures, nuclear power plants, defence installations, and structures withstanding earthquake excitations. For these structures, an exceptionally high safety standard is required and analyses by conventional methods are frequently considered inadequate. Also, the nonlinear response over the whole load range up to ultimate collapse has to be modelled accurately.

At the present, increasing complexity in modern structures, in terms of special loading and high standards, has often required the use of nonlinear analysis methods in design.

Nonlinear analysis techniques for reinforced concrete structures prove to be invaluable to set numerical models for parametric studies and to develop and assess simplified methods of analysis and design.

As a result, there has been much development in the use of the finite element method in nonlinear analysis of reinforced concrete structures, attributable to the research undertaken over the last two decades. Nevertheless difficulties remains,

restricting widespread application of the technique. The major problems are the inadequate description of material properties and the high computing costs.

Accurate material constitutive relationships are crucial to any sophisticated finite element program and determine its efficiency and reliability. Reinforced concrete is a highly complex material which exhibits nonlinear responses due to microcracking, concrete compressive crushing and tensile cracking, reinforcement yielding, dowel action and aggregate interlock, reinforcement bone-slip, and time and history dependent effects. Among these, concrete cracking under tensile stresses is the most significant factor. Unfortunately, a generally accepted constitutive model for this material does not yet exist. Moreover, all material models available are derived based on tests using concrete with compressive strengths less than about 41 MPa. Reassessment of these models is required to determine their applicability for high-strength concretes. Consequently, caution should be exercised in extrapolating data from normal strength to high-strength concretes. More research work is needed in this area.

A variety of material models are available for steel and concrete, as summarized in chapter 2. They are normally adapted from experimental observations with idealization and simplifications before input into a numerical model.

1.3 Research scope

In contrast to the ever growing demand of high-strength concrete, there is little information on this state-of-the-art material and its structural behaviour. In the last decade, some research efforts were directed towards the structural behaviour of high-strength concrete beams. However, to the best of the author's knowledge, there is no documented research on the tension softening response of high-strength concrete and

its applications for finite element analysis of high-strength concrete slabs.

Triggered by the development of Hibernia offshore oil exploration, an ongoing research program on high-strength concrete and its slabs with relative heavy reinforcement is being carried out both experimentally and numerically at M.U.N. The work reported herein includes the experimental investigation on the tensile behaviour of high-strength concrete and finite element analysis of its slabs. Particular attention has been focused on the post-cracking tensile behaviour of high-strength concrete.

The material tension softening behaviour is first sought through an experimental programme. The constitutive relationship of high-strength concrete in uniaxial tension is thereafter developed, based on the test evidence. The developed tension relation including post-cracking softening response and other material properties recorded from laboratory testing are then incorporated into a plasticity based material model implemented in a general purpose finite element analysis code selected to model the slab load-deflection response through entire load range, including ultimate collapse. Contribution is intended towards the static finite element analysis of high-strength concrete slabs, with emphasis placed upon the importance of realistic material properties and the need of a valid concrete model.

1.4 Research objectives

The research objective of this thesis is to provide a suitable finite element modelling of high-strength concrete slabs, which in turn improves the relevant design procedure. Particular attention has been focused on the adequate representation of the post-cracking tensile behaviour of high-strength concrete.

After formulation of a finite element model with proper material constitutive re-

lationships including post-cracking behaviour for high-strength concrete, its validity is established by comparison to the experimental results. Once the numerical model is verified, it becomes a powerful research tool which can be used to study aspects related to the slab behaviour, to verify the test results and to strengthen the analytical procedure. Moreover, it should be possible to extend the finite element analysis to various structural members other than slabs, provided a suitable type of element and its versatility is utilized.

The research objectives of this investigation can be summarized as follows:

1. To develop a special test method in order to obtain a reliable load-deformation behaviour of high-strength concrete in tension, including the post-peak softening response.

2. To characterize the tension softening response analytically by development of a realistic tension softening model to adequately describe the entire tensile response of high-strength concrete.

3. To investigate the mechanical properties of high-strength concrete in tension, with all three tension test methods employed: direct tension, split tensile and modulus of rupture.

4. To study the effects of cold ocean water (temperature and concrete exposure time), simulated under laboratory conditions, on the mechanical properties of high-strength concrete in tension.

5. To enhance the understanding of high-strength concrete by comparison to normal strength concrete in terms of fracture energy, tensile properties and entire load-deformation response under the direct tensile load.

6. To verify the formulated finite element model by comparison to the experimental results of high-strength concrete slabs with varing parameters of concrete strength, geometry, reinforcement ratio and yielding stress, etc., obtained from this study and from previous studies conducted at M.U.N.

7. To derive a tension stiffening model of reinforced high-strength concrete for slab analysis, based on experimentally observed tesion softening behaviour of plain high-strength concrete, and comparison of the predictions of numerical model to test results of high-strength concrete slabs.

8. To initiate a parametric study on the structural behaviour of high-strength concrete slabs subjected to inplane and lateral loads, in which the geometry of the slabs, their material properties, boundary conditions, the type and the sequence of loading are varied.

1.5 Thesis outline

In addition to this chapter, there are seven more chapters to form this thesis.

Chapter 2 is a literature review of the recent research work relevant to the topic.

Chapter 3 contains the experimental investigation of tension behaviour of high-strength concrete. All three types of tension tests were employed in study.

Chapter 4 recommends an analytical expression by which measurements from direct uniaxial tension tests are characterized into a realistic tension softening model.

Chapter 5 presents the recommended analytical models of post-cracking behaviour of reinforced high-strength concrete. The realistic stress-strain characteristics of high-strength concrete and reinforcing bars obtained in the laboratory are incorporated into

a proposed plasticity-based material model, which employs smeared crack concept.

Chapter 6 dealts with verification of the formulated finite element model.

Chapter 7 presents a tension stiffening model, which is approximately formulated, based on the fracture energy concept and comparison of finite element predictions to experimental results of reinforced high-strength concrete slabs.

In Chapter 8, the main conclusions drawn in various parts of the thesis are collated and further supplemented.

Chapter 2

Review of Literature

2.1 Introduction

This chapter summarizes two aspects related to concrete structures, namely: concrete behaviour in ocean environment, and the nonlinear analysis of reinforced concrete structures.

A brief review of structural concrete development is presented, with emphasis placed upon its application in marine and offshore civil engineering. The demand of high-strength concrete for marine offshore structures is rationalized, based on the challenge posed by the cold ocean temperate and harsh environment. The adverse effects of cold ocean water on high-strength concrete mechanical properties is also addressed.

Also this chapter concentrates on a more detailed survey of the relevant literature covering recent work on nonlinear analysis of reinforced concrete structures with focus on the modelling of concrete tension behaviour. The difficulties associated with material modelling and nonlinear analysis with finite element method is also discussed.

2.2 Concrete in marine and offshore engineering

2.2.1 Historical background

The development of concrete as a structural material has been gradual over centuries. Concrete has been widely used in marine civil engineering for harbour works and breakwaters (Gerwick, 1976). Large seagoing reinforced concrete vessels were built in USA during the First World War. Up to date, some of them still remain in use as breakwaters. This accentuates the fact that well built concrete structures are lasting.

The first large scale apllication of concrete to oil industry took place in 1971 with the construction of Ekofisk 1, the first concrete Gravity Based Structure (GBS) installed in the North Sea. It was constructed in 70 m deep water and contained 80000 m^3 of normal strength concrete with a specified 28-day compressive strength of 45 MPa. Thereafter, over twenty other concrete gravity platforms have been constructed in the North Sea, the Baltic Sea and offshore Brazil (Hoff, 1985).

In these apllications, concrete was selected over steel as structural material because of its advantages: durability, great self weight, less prone to progressive damage, and cheaper to maintain when compared with steel structures.

The minimum compressive strength specified by ACI Committee 357 (1985) is 35 MPa for all zones and 42 MPa where severe surface degradation is likely. The modern offshore structures in the North Sea were built with high-strength concrete with minimum compressive strength of 60 MPa (Haug and Sandvik, 1988).

It has been shown that the offshore concrete platforms have survived the harsh North Sea environment. But, they are now facing the additional challenges posed by the North Atlantic and Arctic Offshore frontiers. Consequently, high-strength structural concrete is being required to provide a concrete with improved resistance

to chemical attack, better abrasion resistance, improved freeze-thaw durability, reduced permeability, increased modulus of elasticity and decreased creep and shrinkage. Thus, high-strength structural concrete offers an excellent solution to problems associated with severe adverse sea environment.

2.2.2 Durability

It was found that concrete durability was largely dependent on its permeability, as stated by Marzouk and Hussein (1990), Mehta (1980) and Mather (1980), and Gjorv (1971), based on their extensive studies on the case histories of deteriorated portland cement concretes exposed to sea water, in both mild and cold climates, for different exposure ages up to 67 years. The individual process of deterioration tends to limit itself to different parts of a structure depending on the tidal lines.

Based on this observation, Mehta (1980) divided a marine structure into three zones. The upper most part of the structure above the high-tide line is defined as the atmospheric zone, which is not directly exposed to sea water. Instead, it is exposed to atmospheric air, winds carrying salts and frost action. Consequently, cracking due to corrosion of reinforcement and/or freezing and thawing of concrete becomes a predominant factor causing deterioration in this zone. The concrete in the splash zone between the high and low-tide marks is, not only vulnerable to cracking and spalling of concrete due to wetting and drying, frost action and reinforcement corrosion, but also to loss of material due to chemical decomposition of the hydration products of cement and the impact of waves containing ice, sand, and gravel. The lower part of the structure (submerged zone), which is always submerged in sea water, is vulnerable to strength retrogression and loss of material as a result of the chemical

reaction between sea water and hydration products of cement. Consequently, the permeability of concrete is the most important property in all the three zones, which influences all physical and chemical phenomena causing concrete deterioration.

In spite of the physical and chemical effects of cold ocean water on high-strength concrete, there is very limited effort directed towards the study of the adverse effects of ocean environment on the behaviour of high-strength concrete.

2.3 Concrete tensile strength as a design criterion

Failure of reinforced concrete structures is usually initiated by cracking of plain concrete. The cracking process starts at a low tensile stress level associated with a very early load stage. Cracking and post-cracking behaviour of concrete, which is governed by its tensile properties, is a very important feature of concrete and has a significant effect on the behaviour of the concrete structural member. The experimental evidence (William 1986, Clark and Speirs 1978) has shown that the average strains in the steel in a real situation are much lower than would be expected when ignoring the tensile contribution from concrete, even at strains much above the cracking strain. Although the concrete tensile stress tends to zero at the cracks, the concrete in between two adjacent cracks is still capable of sustaining appreciable tensile stress induced due to the inherent bond effect and aggregate friction interlock. The concrete contribution in tension towards the overall stiffness of a member is known as tension stiffening and the effect can be very significant in the postcracking range under service loads. As the load level increases, tension stiffening gradually deteriorates due to progressive bond breakdown.

However, it has long been a common practice in the conventional designs to neglect the tensile strength of concrete since it is relatively weak in tension. Thus, the predicted deflections and crack widths could be well overestimated in excess of those observed in tests and in practice by ignoring the concrete tension stiffening effect in the serviceability range. Therefore, most modern design codes have a provision to allow for tension stiffening, using either the average steel strain (e.g. British design code (BSI BS8110, 1985) and the European CEB recommendations (CEB, 1986)) or the effective moment of inertia of a member (e.g. American ACI code (ACI318-83, 1983)) to enable a gradual transition from an uncracked elastic state to a fully cracked state.

In these modern design codes, requirements for both ultimate and serviceability limit states are specified, based on the probability principles. The former concerns safety and the provision of adequate strength against structural collapse. The latter deals with the performance of the structure under working loads, with particular reference to the control of deflections and crack widths. Because of the increases in permissible steel stress over the past few decades, steel strains in modern structures are generally high and the serviceability requirements have now often become the critical factors in design.

2.4 Finite element analysis of reinforced concrete structures

2.4.1 Introduction

Nonlinear analysis using finite element method is particularly attractive for design calculations at the serviceability limit state with tension stiffening, in that changes

in material stiffness due to concrete cracking, concrete crushing, steel yielding, etc. can be conveniently and properly modelled, provided an accurate description of the material constitutive relations is available. Therefore, the application of nonlinear finite element analysis of reinforced concrete structures has been increasing.

The early work of the application of finite element methods in the analysis of reinforced concrete is illustrated in Fig. 2.1 (Ngo and Scordelis, 1967).

There are three fundamental requirements for any structural analysis method: the force equilibrium, the displacement compatibility, and the laws of material behaviour. In the finite element method, the force-displacement relations for each element are usually formulated by using the virtual work principle or the principle of minimum potential energy. The displacement variables within each element are usually represented by polynomial expressions. The compatibility conditions are satisfied exactly, because continuous displacement fields are used; the equilibrium conditions are satisfied in an overall sense using imagined forces at the nodes, rather than having every infinitesimal element in equilibrium. The force-displacement relations for each element involve integrals over the element volume. These integrals are evaluated approximately using values at integration points or Gauss points and weighting functions. In a sense, the material laws are satisfied only at the Gauss points, which represents adjacent volumes of material.

The iterative solution techniques are usually employed when finite element analysis is applied to a material such as concrete that exhibites nonlinear behaviour due to concrete cracking and other material nonlinearities. Three common iterative solution techniques (Scordelis, 1978) are illustrated in Fig. 2.2. With either of these techniques, the system of internal forces are sought in approximate equilibrium with

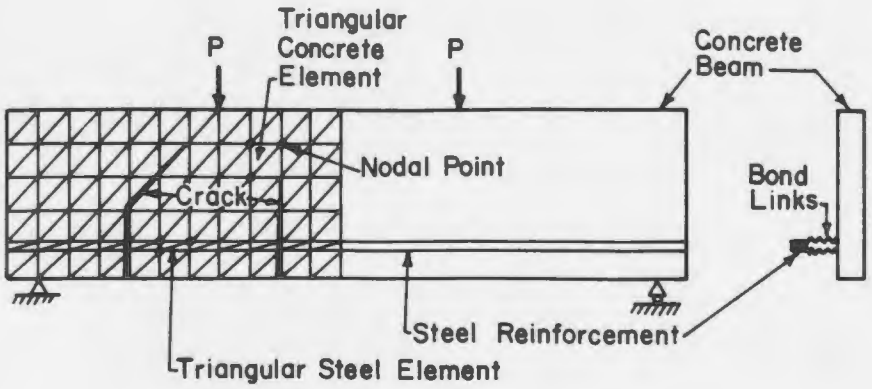

Figure 2.1: Finite element modelling by the discrete crack approach (Ngo and Scordelis, 1967)

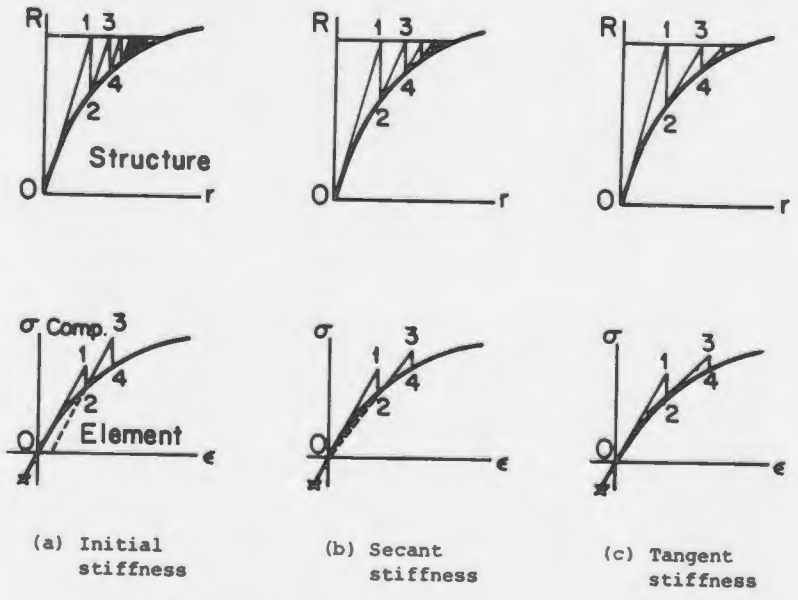

Figure 2.2: Iterative solution techniques for nonlinear analysis (Scordelis, 1978)

the applied external loads, within certain specified tolerance. A successful analysis requires proper satisfaction of material property laws as well as an accurate definition of these laws.

There is a large amount of literature on the use of the finite element method in the analysis of reinforced concrete structures. Comprehensive surveys can be found in ASCE (1982), Chen (1982), Scordelis (1978), and Cope (1984 and 1986). In this chapter, literature review only focuses on concrete nonlinear responses, especially cracking, and their modelling. The concrete cracking and post-cracking behaviour is first reviewed, followed by associated modelling techniques including constitutive relations for concrete tension stiffening and the representation of reinforcement. The computational difficulties resulting from the use of tension stiffening models are also presented.

2.4.2 Concrete cracking

The tensile weakness of concrete and ensuing cracking that results therefrom, is a major factor contributing to the nonlinear behaviour of reinforced concrete elements. The tensile stress fields applied to concrete induce cracking that has a significant influence on the basic behaviour of the member through the entire load range up to structural failure. As a result, the cracking and post-cracking behaviour has been a major concern for decades.

2.4.2.1 Tension softening of plain concrete

It is experimentally observed that after concrete cracks have developed, the concrete between two adjacent cracks is still capable of sustaining appreciable tensile forces

induced due to the inherent bond effect and aggregate friction interlock. This phenomenon is referred to as concrete tension softening in literature. Many researchers have reported the observations of concrete softening behaviour from plain concrete tension tests performed by controlling the specimen deformation. Evans and Marathe (1968) first illustrated this behaviour on specimens loaded in direct tension in a testing machine modified to control deformation. The recorded tensile stress-strain curves are presented in Fig. 2.3 that including unloading beyond the maximum tensile stress. The descending branch was determined primary by localized deformation across individual cracks, as stated by Petersson (1981), hereby indicating that there are large differences between the average strain and local cracking strains. Some test results from Petersson (1981) are shown in Fig. 2.4.

In recent years, testing techniques have been improved by the use of electrohydraulically controlled testing machines. The deformation of the specimens can be well controlled through such testing machines so that the sudden brittle failure of concrete specimens in direct tension can be avoided. Consequently, more experimental evidence from concrete tests under direct tension has been obtained that confirmed concrete tension softening and its localized nature. Different tension specimens employed in different research programmes are illustrated in Fig. 2.5.

However, there is no standard test method for testing concrete in direct tension, because of the difficulties associated with applying a pure tensile force to a plain concrete specimen. This is the main reason that the limited information on direct tension behaviour of concrete is often conflicting. The test results were considerably different with various testing methods employed. This was demonstrated in the measurements of the tensile strains at maximum tensile stress. The recorded strain corresponding

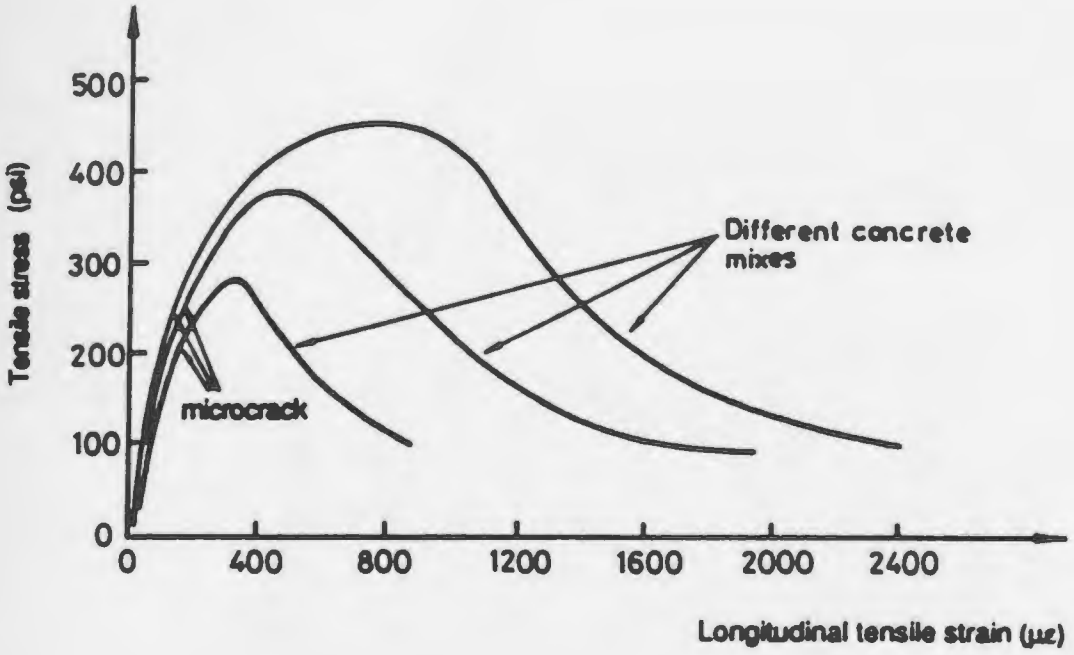

Figure 2.3: Typical experimental stress-strain diagrams for plain concrete in direct tension (Evans and Marathe, 1968)

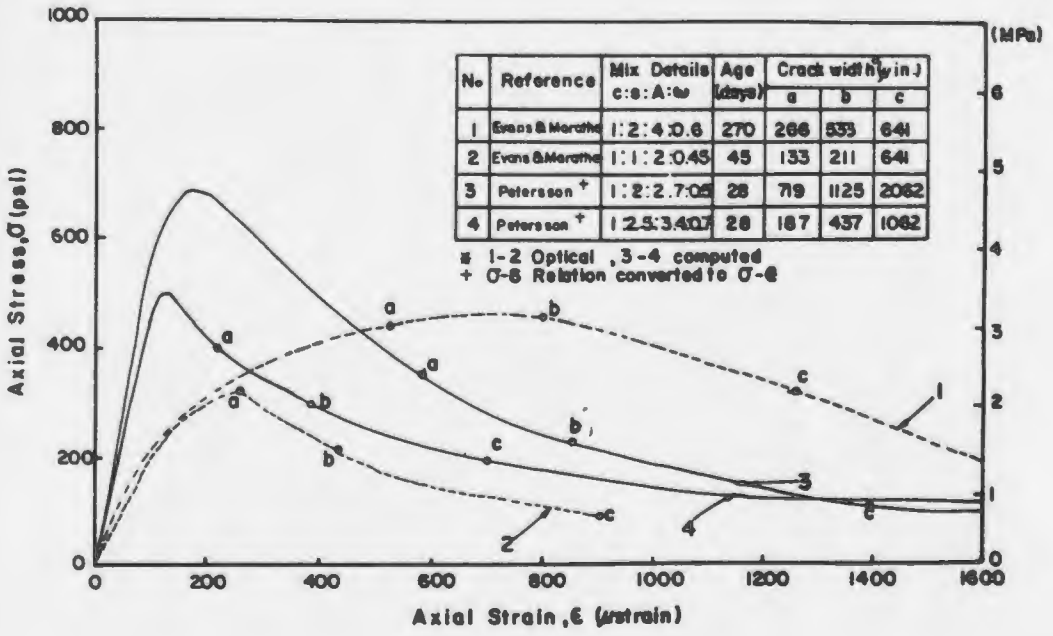

Figure 2.4: Comparison of the test results from plain concrete under direct tension (Evans and Marathe 1968, and Petersson 1981)

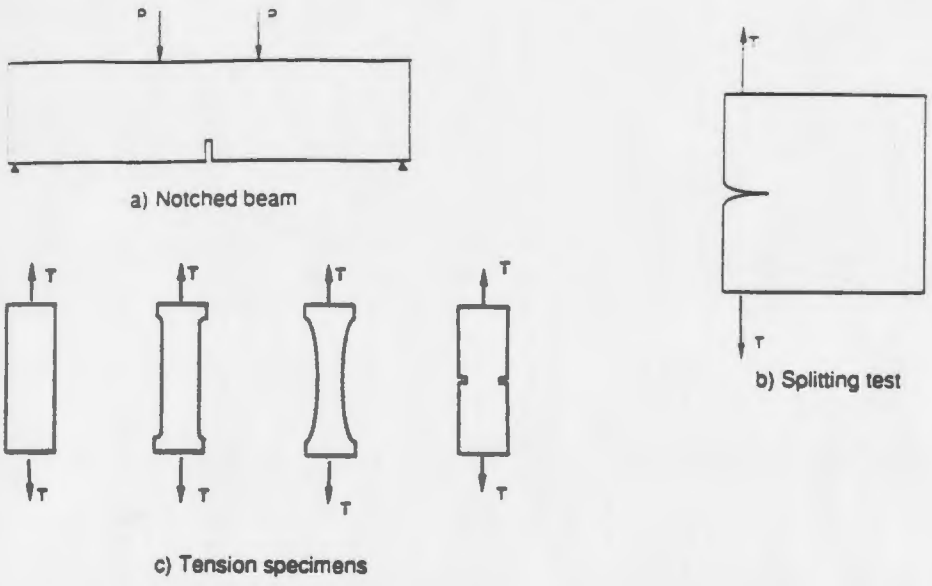

Figure 2.5: Different tension specimens employed in research

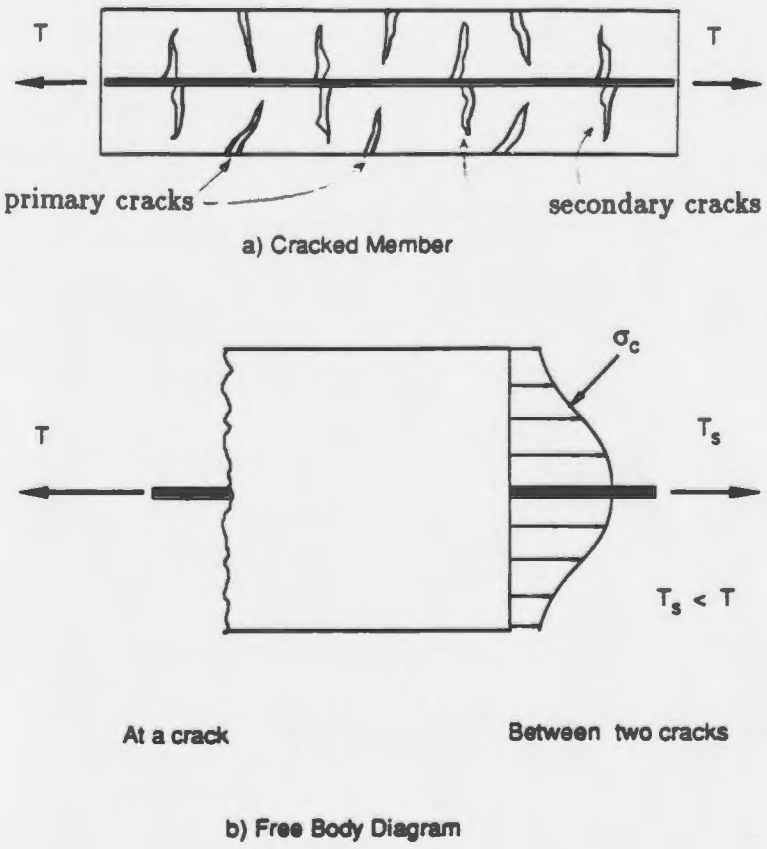

Figure 2.6: Reinforced concrete member in tension

to maximum tensile stress were 200-800$\mu\varepsilon$, 60-90$\mu\varepsilon$, 97-132$\mu\varepsilon$ and 70-136$\mu\varepsilon$, reported respectively by Gopalaratnam and Shah (1985), Evans and Marathe (1968), Hughes and Chapman (1966), and Guo and Zhang (1987). Epoxy glue was used by Guo and Zhang (1987) to connect the steel loading plates to both ends of specimens in a stiff frame consisting of two beams and four bars placed in parallel with the specimen. Instead, special grips were used to connect the specimen with the testing frame (Gopalaratnam and Shah 1985, and Naaman and Homrich 1989).

The effect of different testing methods is also illustrated in Fig. 2.4, where data from two sources are compared (Evans and Marathe 1968, and Petersson 1981). Curves 1 and 2, shown as dotted lines, were obtained by testing concrete specimens in parallel with a steel tension frame (Evans and Marathe, 1968). This technique was developed to avoid unstable failure at the peak load resulting from the sudden release of stored elastic energy in the testing system. Curves 3 and 4, shown as solid lines, were obtained by testing concrete specimens in parallel with stiff aluminum columns (Petersson, 1981) The load was indirectly applied to the concrete specimens by heating the aluminum columns. A large discrepancy in values of the modulus of elasticity, peak strain and crack widths are observed between two sets of curves.

Furthermore, all available information were from the tests of normal strength concrete and fibre concrete in direct uniaxial tension. There is no documented information for high-strength concrete in direct tension.

2.4.2.2 Tension stiffening of reinforced concrete

a) Development of tension cracks

Broms (1965) identified two types of tension cracks in the reinforced concrete member after its tensile capacity is reached. The first type is called primary or external crack, such visible crack exists at the concrete surface. The second type, named secondary or internal crack, does not progress to the concrete surface. Each of these two types of cracks has a different geometry, as illustrated in Fig. 2.6. More recently, the formation and development of tension cracks were also studied in detail by Goto and Otsuka (1979).

b) Stress distribution after cracking

As a result of the formation of cracks in a tension member, a new stress pattern develops between the cracks. The stress distribution in a cracked reinforced concrete member, reported by Lin and Scordelis (1975), is illustrated in Fig. 2.7, indicating concrete retaining substantial tensile capacity after cracking.

c) Tension stiffening

The concrete contribution to the overall stiffness of a reinforced member is known as tension stiffening. This phenomenon has often been observed in experiments. Because of the variability in tensile strength along the length of a concrete member, cracks do not all form at the same stress level. Clark and Spiers (1978) estimated that the first major crack forms at about 90 percent of the average concrete tensile strength and the last major crack at about 110 percent of the average concrete tensile strength. The tension stiffening effect from typical tests on reinforced concrete beams and slabs, as

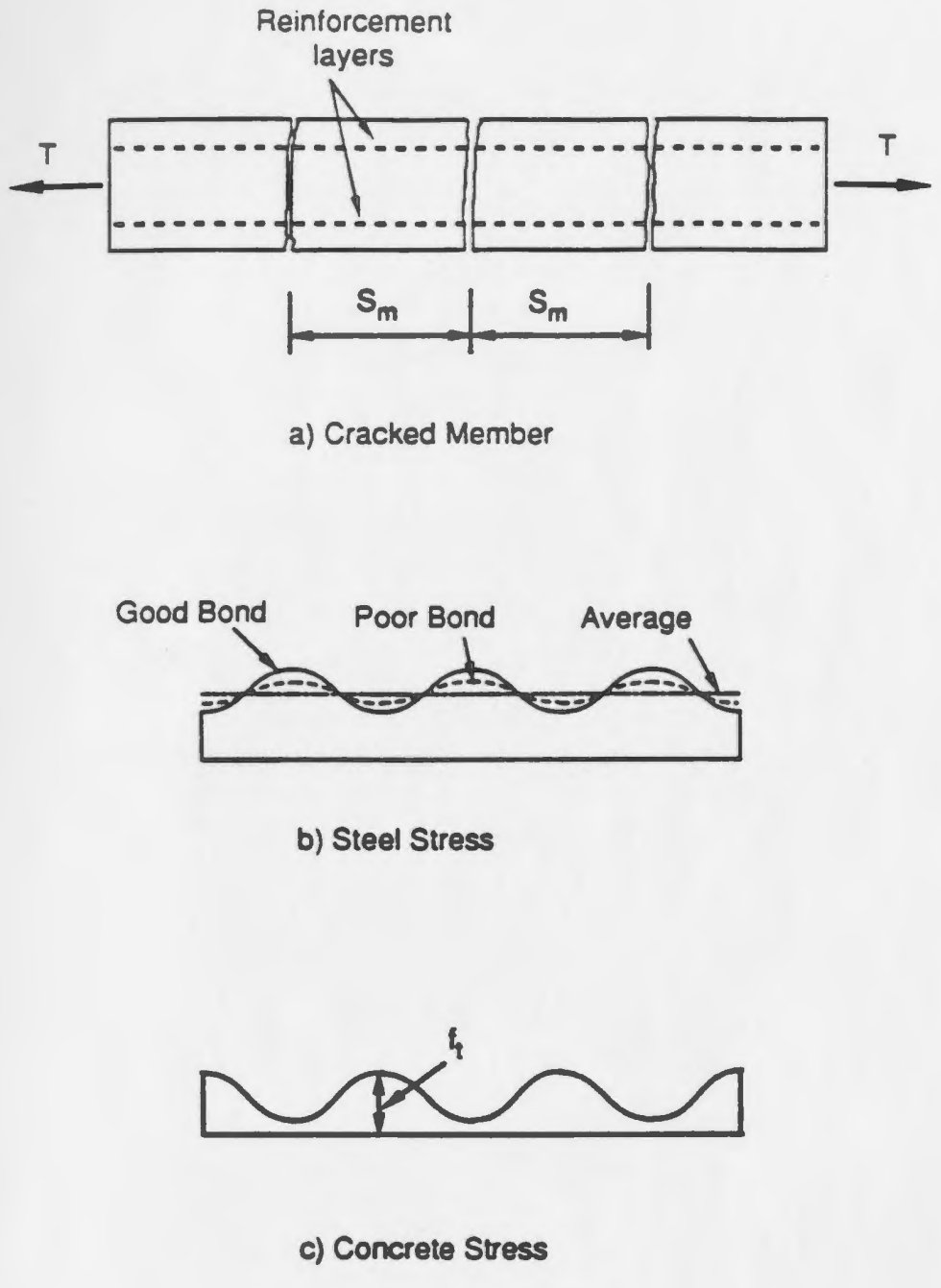

Figure 2.7: Stress distribution in a cracked reinforced concrete element (Lin and Scordelis, 1975)

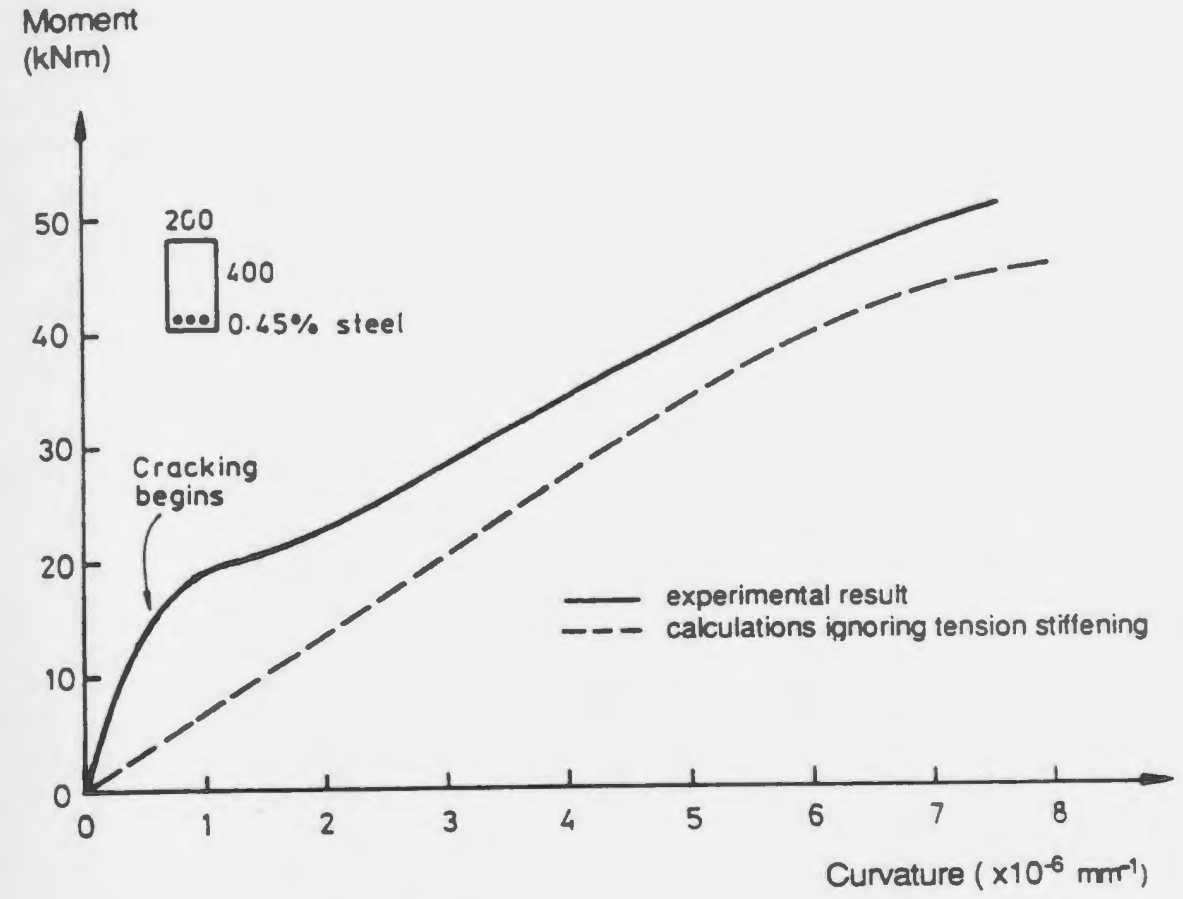

Figure 2.8: Tension stiffening effect from typical tests on reinforced concrete beams and slabs (Clark and Spiers, 1978)

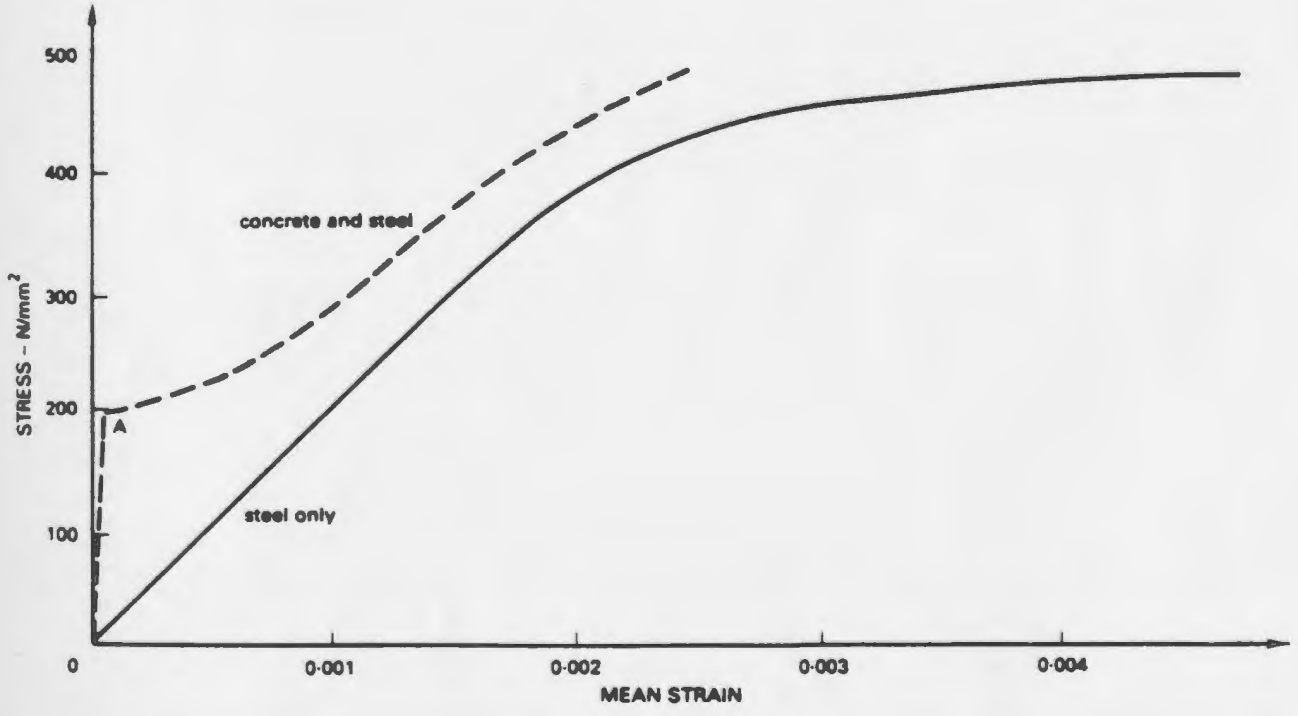

Figure 2.9: Tension stiffening effect from typical tests on large reinforced concrete elements under direct tension (William, 1986)

experimentally observed by Clark and Spiers (1978), is presented in Fig. 2.8. More recently, William (1986) performed tests on the large reinforced elements subjected to direct tension and also found a pronounced tension stiffening effect (Fig. 2.9).

2.4.3 Modelling of concrete post-cracking behaviour

The strain softening branch measured on plain concrete in direct tension descends gradually as cracks open and stress decreases, as described in detail in the proceeding section. This phenomenon could be attributed to the coarse aggregate interlock at narrow widths, energy absorbed in crack surfaces, etc. Therefore, the concrete tensile stress will not actually be zero just after cracking, but will rapidly tend to zero.

The post-cracking stress-carrying capacity of concrete is more pronounced in the reinforced concrete due to additional strength enhancement as a result of interactions between reinforcement and concrete. Recently, it has become increasingly evident that it is necessary to simulate the local energy release properly as the crack propagates in order to achieve accurate predictions of the responses of concrete structures, such as load-deflection characteristics, crack width, bond transfer and shear transfer phenomenon, and tension-stiffening of concrete between cracks.

Consequently, the falling branch of complete stress-strain diagrams of concrete in tension is commonly used in the finite element analysis of reinforced concrete to represent the concrete tension stiffening.

The research on post-cracking behaviour of reinforced concrete has been carried out for the last two decades. A number of constitutive descriptions of concrete post-cracking behaviour has been proposed by various previous researchers, which are reviewed in the rest of this section.

2.4.3.1 Simplified concrete tension models (stepped, bilinear, exponential, etc.)

Due to the lack of experimental data associated with the difficulties posed in concrete tests under direct tension, few accurate models are available to describe the softening response of concrete in uniaxial tension. The concept of average strain over a relatively long gage length was first considered by Scanlon (1972). An approximate formulation was used to incorporate gradual loss of stress-carrying capacity of plain concrete in tension in the numerical schemes that accounted for the tension stiffening effects observed in reinforced concrete. Concrete was assumed to be linear up to the tensile strength, followed by a series of discrete steps, each with decreasing modulus of elasticity, as shown in Fig. 2.10a.

The proposal of Scanlon (1972) has been modified and adopted by many other analysts. Lin an Scordelis (1975) considered experimental stress-strain data and fitted for the falling branch a polynomial expression

$$f_t = a_0 + a_1\epsilon_{to} + a_2\epsilon_{to}^2 + a_3\epsilon_{to}^3 \tag{2.1}$$

where a_0, a_1, a_2, and a_3, are constants (Fig. 2.10b). The limiting strain ϵ_{max} at zero stress was assumed to be five times the tensile strain ϵ_{to} at the tensile strength f_t'. And, Maeda et al. (1976) preferred hyperbolic unloading defined by

$$f_t = \frac{f_t'\epsilon_{to}}{\epsilon_t} \tag{2.2}$$

based on results from beam tests. A similar model was formulated with a continuous damage concept by Mazars (1981) to represent post-peak stress-strain curves of concrete (Fig. 2.10c).

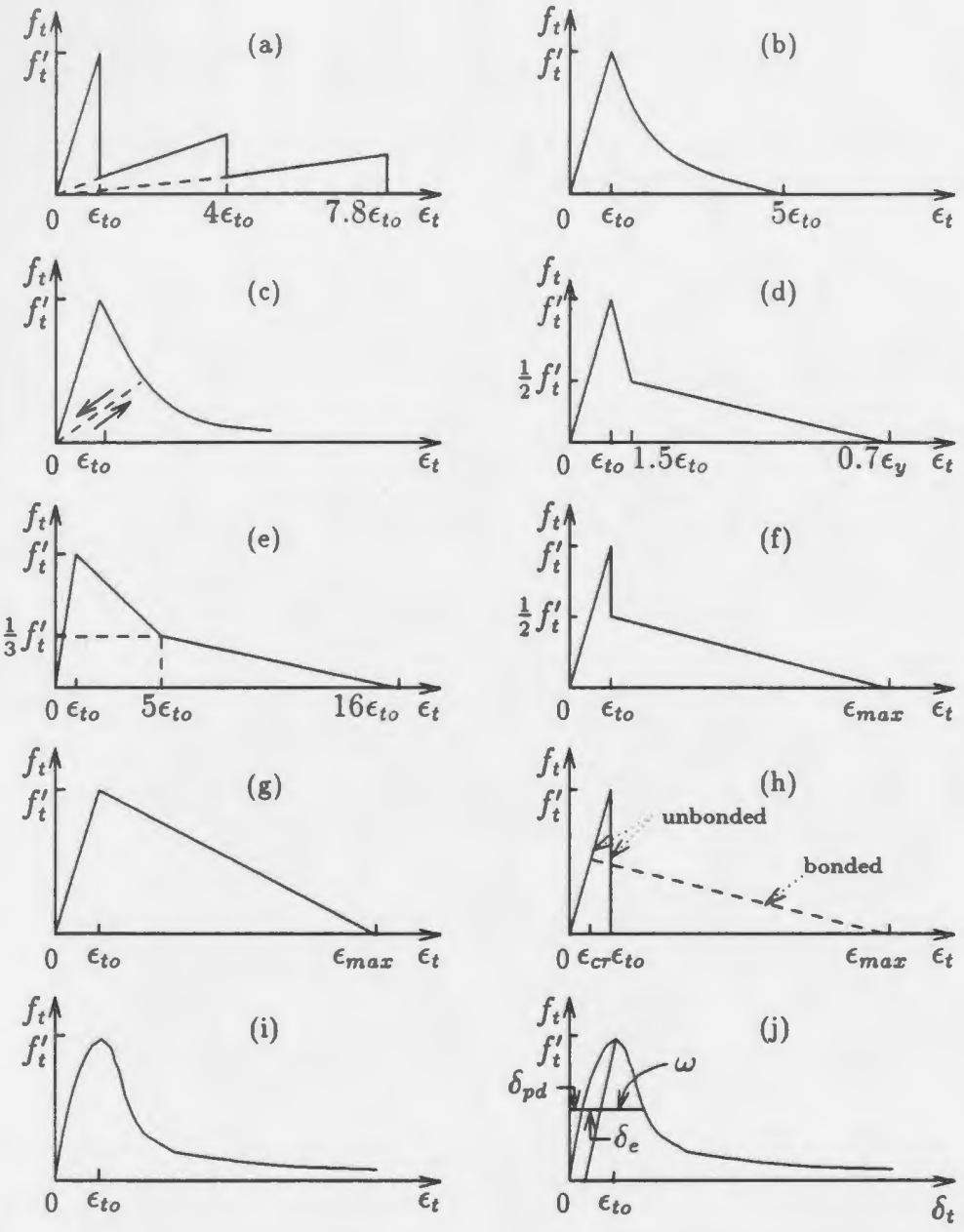

Figure 2.10: Modelling of concrete tension stiffening
(a) stepped unloading response (Scanlon, 1972); (b) smooth unloading model (Lin and Scordelis, 1975); (c) modified smooth unloading model (Mazars, 1981); (d) bilinear unloading model (Cope et al., 1979); (e) modified bilinear unloading model (Massicotte et al., (1990); (f) discontinuous unloading model (Damjanic and Owen, 1984); (g) simple linear unloading model (Bazant and Oh, 1984); (h) modified linear unloading model (Bergan and Holand, 1979); (i) continuous stress-deformation model (Guo and Zhang, 1987); (j) continuous stress-crack width model (Gopalaratnam and Shah, 1985)

Cope et al. (1979) fitted a bilinear relationship for the falling branch (Fig. 2.10d). A similar relationship, but with different parameters, was also proposed by Massicotte et al. (1990). A detailed analysis was performed on 52 test results, reported independently by Gopalaratnam and Shah (1985), Guo and Zhang (1987), Yankelevskey and Reinhardt (1987), Bazant and Oh (1983), and Hillerborg (1985). Based on this analysis, Massicotte et al. proposed a trilinear stress-strain curve (Fig. 2.10e) with a reasonable compromise between accuracy and simplicity, with a linear ascending branch and a bilinear tension softening branch for concrete after cracking. The change of slope in the descending branch occurs at one-third of f'_t and five times peak strain ϵ_{to}, similar to that suggested by Hillerborg (1985). The ultimate tensile effective strain was specified as sixteen times ϵ_{to}.

In addition, Damjanic and Owen (1984) even chose a discontinuous linear pattern to represent the softening branch of stress-strain curve for plain concrete (Fig. 2.10f).

2.4.3.2 Simple linear tension models of concrete

For simplicity, many other researchers like Bergan and Holand (1979) and Bazant and Oh (1984) simply specified a single linear falling branch after the concrete tensile strength is reached (Fig. 2.10g).

In many cases the extent of softening, defined by the parameter α, where

$$\epsilon_{max} = \alpha \epsilon_{to} \tag{2.3}$$

has been specified differently by various analysts. Damjanic (1983) related the value of α to the nature of the problem being analysed; valued of 5 to 10 were proposed for shear type cracking and 20 to 25 for flexural type cracking. Kulicki and Kostem

(1972) argued that microcracking in concrete occurs at a tensile strain ϵ_{cr} lower than ϵ_{to} (Fig. 2.10h): values of $\epsilon_{cr} = 0.55\epsilon_{to}$, $\epsilon_{to} = 0.0001$ and $\epsilon_{max} = 0.0007$ were further recommended by Bergan and Holand (1979).

In an approach based on fracture mechanics theories and on the blunt crack band model, Bazant and Oh (1983) related the area W_f under the concrete tensile stress-strain curve to the fracture energy G_f, so that

$$G_f = \omega_c W_f \tag{2.4}$$

where G_f is the energy absorbed to create a unit area of crack surface, and ω_c is the effective width of the fracture process zone (or crack band) over which microcracking is distributed. The value of ω_c is dependent on the element size, element type, and the nature of the problem.

2.4.3.3 Continuous tension models of concrete

In contrast, some other researchers proposed a continuous tension model, similar to one for concrete in compression. The concrete tensile stress was expressed in terms of the crack width, tensile strain and deformation, as proposed by Gopalaratnam and Shah (1985), Carreira and Chu (1986) and Guo and Zhang (1987), respectively. The stress-displacement relationship was continuous prior to and beyond the peak stress (Figs. 10i and 10j). Any abrupt changes in the stiffness, which are characteristic of discontinuious tension models between ascending and descending branches, are likely to pose instabilities in certain numerical schemes. Hence, it appears that the continuous tension models are more suitable with finite element method. These types of continuous models are further discussed in detail in chapter 4.

2.4.3.4 Layered tension models of concrete

The post-cracking response of concrete differs considerably through the thickness of a flexural reinforced concrete member such as beam and slab, depending on the relative distance away from the reinforcement. In order to represent this phenomenon, two additional concrete stress-strain relations were specified by Gilbert and Warner (1978) to describe the behaviour of the concrete layers once and twice removed from the tension steel. The solution is somewhat dependent on the thickness of the concrete layers, or the number of layers used to represent a member section.

2.4.3.5 Different alternatives for modelling concrete tension stiffening

There are some other methods to represent concrete tension stiffening, reported in the literature. Among these, Bazant and Oh (1983) used a fictitious additional steel area or an equivalent tensile area of concrete at the level of the tension steel to account for tension stiffening. Alternatively, Floegl and Mang (1981 and 1982) indirectly included concrete tension stiffening in the finite element analysis by the use of bond stress-slip relations. An effective moment of inertia of a member section was also used to model tension stiffening in research (Branson, 1977).

It can be seen that various types of tension models have been proposed, to account for the concrete post-cracking behaviour: linear, bilinear, exponential, rational, etc. Usually, the models are only the appropriate representations of experimental behaviour of concrete in tension conducted individually. This reflects that there is no common understanding in this area. More efforts, especially more experimental data, are needed.

Comparative studies by Damjanic and Owen (1984) and Hinton et al. (1981) have

shown that finite element solutions are significantly affected by the shape and extent of the falling branch.

2.4.4 Finite element modelling of reinforced concrete structures

Extensive research has been done in the last two decades on the application of finite elements to modelling the behaviour of reinforced concrete. Consequently, several techniques were developed with finite element method to reflect the changes in material behaviour induced due to cracking and other nonlinear effects (ASCE, 1982). The modelling techniques can be classified into two categories: the discrete crack approach and the smeared crack approach.

In general, both of these two approaches are based on replacing the composite continuum by an assembly of finite elements representing the concrete and reinforcement. Cracking is treated as discrete individual cracks between concrete elements in the first approach, and as distributed cracks within the elements in the second.

Furthermore, three crack concepts were gradually evolving with the the smeared crack approach: the fixed crack, rotating crack, and multi-dimensional cracks. With the fixed crack concept, the orientation of the crack is fixed during the entire computational process, whereas a rotating crack concept allows orientation of the crack to co-rotate with the axes of either principle stress or strain. The multi-dimensional smeared crack concept falls in between the fixed and rotating smeared crack concepts, which allows occurrence of more than one crack at the same sampling point (Yuzugullu and Schnobrich 1973, Darwin and Pecknold 1976, and Massicotte et al. 1990).

2.4.4.1 Discrete crack approach

The discrete crack approach was first introduced in the early days of the application of finite element method in reinforced concrete structures. Ngo and Scordelis (1967) analysed reinforced concrete beams assuming linear elastic material behaviour, using either constant strain quadrilateral or triangle elements to represent both concrete and main longitudinal reinforcement (Fig. 2.1). The vertical shear stirrups were simulated by using one-dimensional bar elements. The individual cracks were modeled by means of separations at common nodes between finite elements, as depicted in detail in Fig. 2.11. A linkage element (Fig. 2.11b), having two degrees of freedom h and v, is to simulate bond stress-slip (Fig. 2.11a), aggregate interlock and opening or closing of the crack (Fig. 2.11d), by assuming appropriate values of the spring stiffness k_h and k_v. In transferring the dowel shear at a crack (Fig. 2.11e), the main longitudinal reinforcement is disconnected from concrete over an effective dowel length, which represents the distance over which bond is assumed to be destroyed.

With this approach, the displacements at the cracks can be calculated, hence allowing assessments to be made of the shear stresses due to aggregate interlock and dowel action, and of the steel stresses at the cracks. However, the solution is mesh dependent since cracks can only form along element boundaries. Thus geometrical restrictions on the calculated crack pattern seem inevitable because of the unknown nature of crack locations and directions while generating the finite element mesh. The redefinition of element topology at a crack is computational inefficient and complicated. Moreover, concepts of fracture mechanics to predict the stress concentrations and extensions at the crack tip were ignored in this early work.

Because of the complications involved in using discrete crack modelling, most

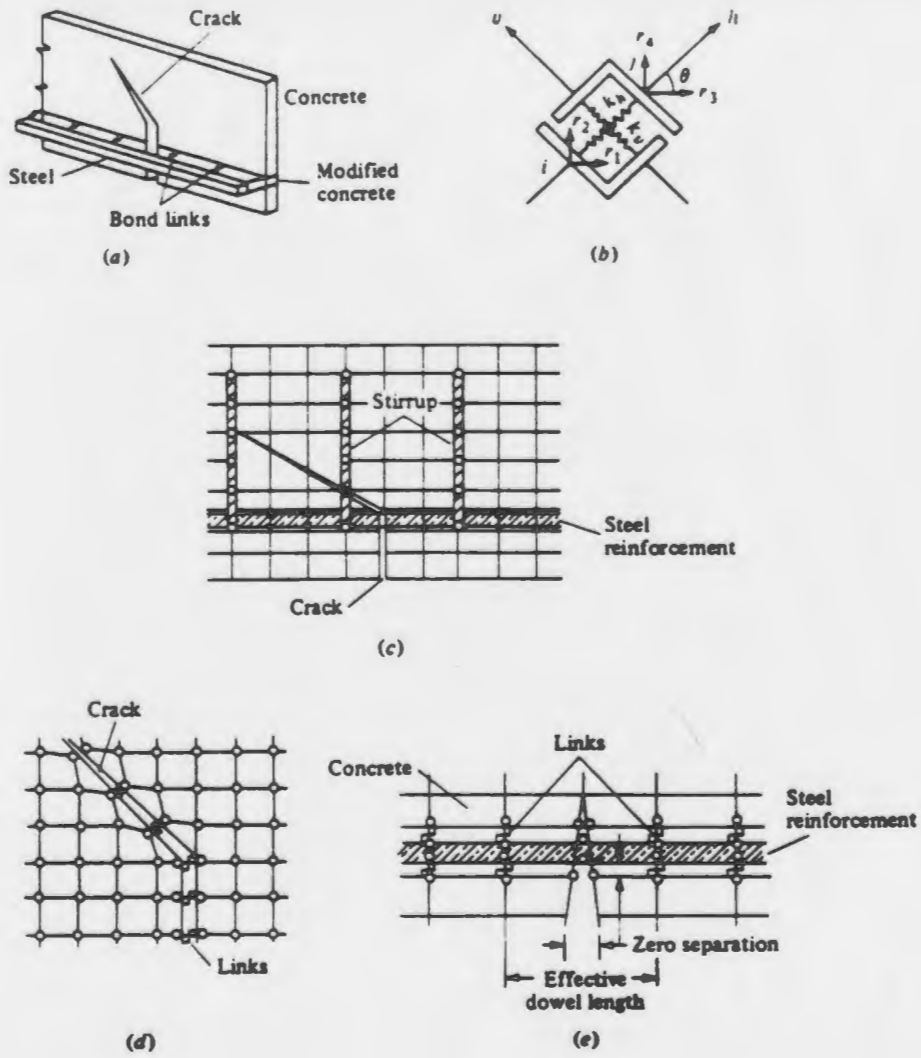

Figure 2.11: Analytical models and linkage elements used in the discrete crack approach (Scordelis, 1972) (a) analytical model (b) linkage element (c) reinforcement representation (d) crack and aggregate interlock (e) effective dowel length

present analyses use the concept in which progressive cracking is assumed to be distributed over an entire element or at integration points within the element, resulting in a smeared crack approach.

2.4.4.2 Smeared crack approach

The smeared crack approach, originally introduced by Rashid (1968), starts from the notion of stress and strain and permits a description of a cracked solid in terms of stress-strain relations. It is sufficient to switch the initial isotropic stress-strain law to an orthotropic law upon crack formation, with axes of orthotropy being determined according to the condition of crack initiation. This approach is attractive not only because it preserves the topology of the original finite element mesh, but also because it does not impose restrictions with respect to the locations and directions of cracks, in other words, the axes of orthotropy. For these reasons the smeared crack approach quickly replaced the early discrete crack approach and came into widespread use during the 1970's. Variations of this approach have been developed by a number of researchers (ASCE, 1982).

a) Multi-layering technique

The layering technique was first applied to model nonlinear behaviour of concrete by Franklin (1970) in the analysis of plane frames, and was later widely adopted for beams, slabs, plates and shells by many others such as Scanlon (1972), Bergan and Holand (1979), Lin and Scordelis (1975), Cope et al. (1980), and Gilbert and Warner (1978). The plane section, assumed to remain plane after deformation, is divided into a number of layers across the depth, with smeared properties in each layer. The steel

reinforment is likewise represented by a smeared steel layer. Each layer is assume to be under a state of plane stress with perfect bond between layers. The effect of cracking is simply averaged over the layer within the region represented by the cracked integration point. The material-property laws for the cracked concrete in terms of average stresses and strains are then followed and are individually defined for each layer across the section thickness. Thus, the summation of material properties across a section can be conveniently carried out in the calculation of internal forces and moments.

Despite its simplicity, the layering approach allows for coupling between membrane and flexural effects with no extra effort. Therefore, it is commonly adopted in solving slab problems with rigid boundaries.

b) Fracture mechanics approach

Kaplan (1961) first analysed the cracked concrete with fracture mechanics approach where a critical stress intensity factor K_{IC} was used to be a measure of the fracture toughness of the concrete as a criterion to govern the material failure. Since then, intensive research has been carried out in this area.

More recent work (Bazant et al., 1979) has shown that the energy consumed in fracture of concrete must be correctly modeled in order to obtain objective finite element results in general cases. Hillerborg et al. (1985 and 1976) further assumed that microcracking existed in the intact concrete and concentrated in a narrow region (the fracture zone) in front of the crack tip. Upon the formation of fracture zone, the stress decreases, the deformation in the fracture zone increases but the deformation in the parts away from this region decreases as unloading occurs. In order to define a

stress-deformation relation independent of the length over which the deformation is measured, two curves were proposed: a stress-strain curve up to the tensile strength, and a falling stress-crack width curve to describe the additional deformation in the fracture zone after the tensile strength is reached (Fig. 2.12). In terms of the energy, the area under the stress-strain curve represents the energy per unit volume absorbed in the intact zones, while the area under the descending stress-crack width curve represents the energy G_f absorbed per unit area of the cracked surface within the fracture zone.

With this assumption, a fictitious crack model (Fig. 2.13) was proposed by Hillerborg (1985). In this model, a crack capable of transferring stresses is used to model the fracture zone. The stresses across the fictitious crack are represented by nodal forces, which follows the stress-crack width relation for the fracture zone. A relatively coarse mesh could be used, because of the absence of stress singularity, so that the absorbed energy is not very sensitive to the mesh size.

The fictitious crack model was widely accepted by several researchers (ASCE, 1982). Modifications were made so that many other phenomena of concrete can be accounted for in this model, such as history-dependence and thermal effects (Rots et al., 1985). Many other methods based on fracture mechanics theories were also developed (e.g. Bazant et al. 1983, and Gerstle et al. 1982).

2.4.5 Representation of reinforcement

There are at least three alternative representations of reinforcement that are commonly used in the finite element analysis of a reinforced concrete member: distributed, embeded, and discrete. These three alternatives are illustrated in Fig. 2.14.

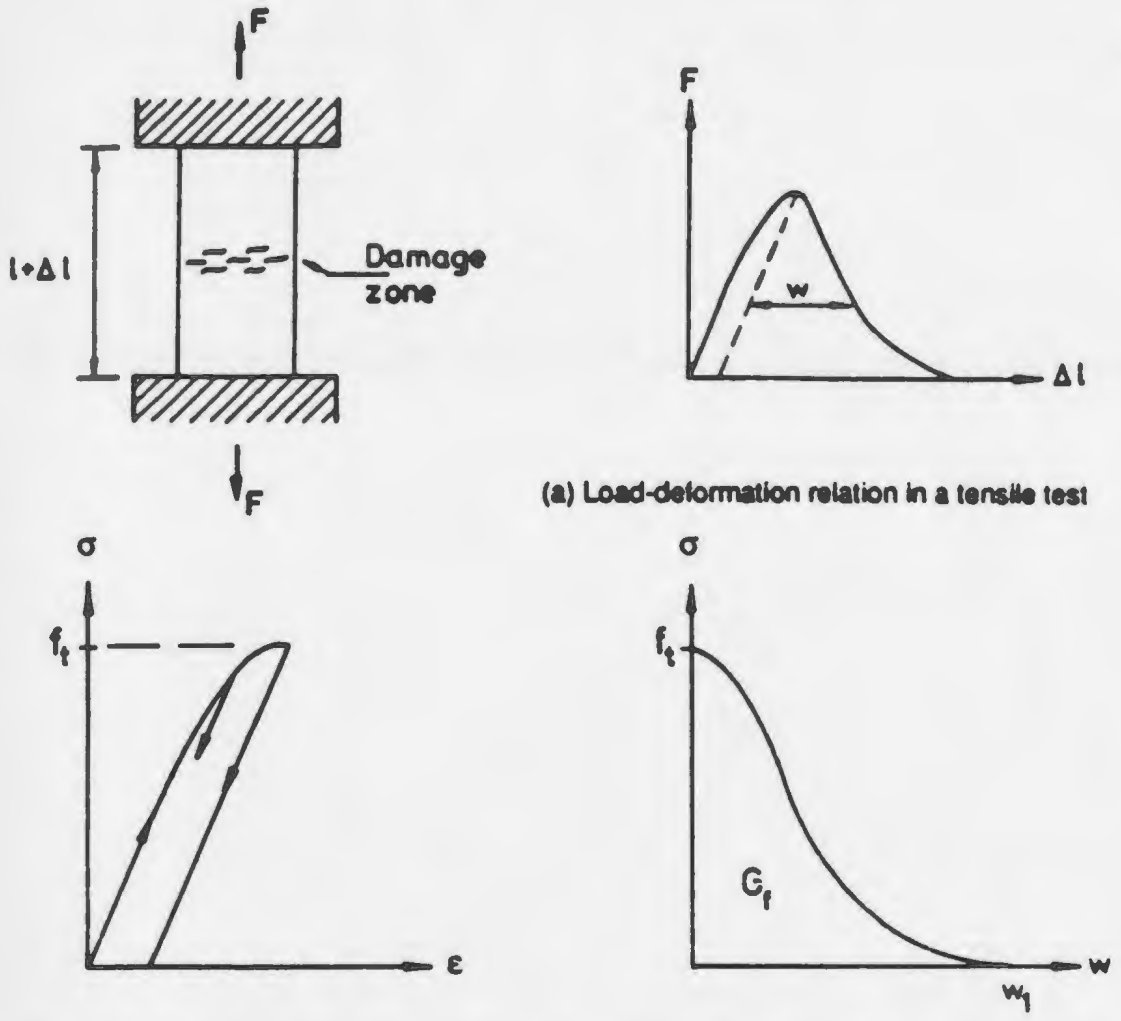

Figure 2.12: Complete load-deformation relation of concrete in tension (Hillerborg, 1985)

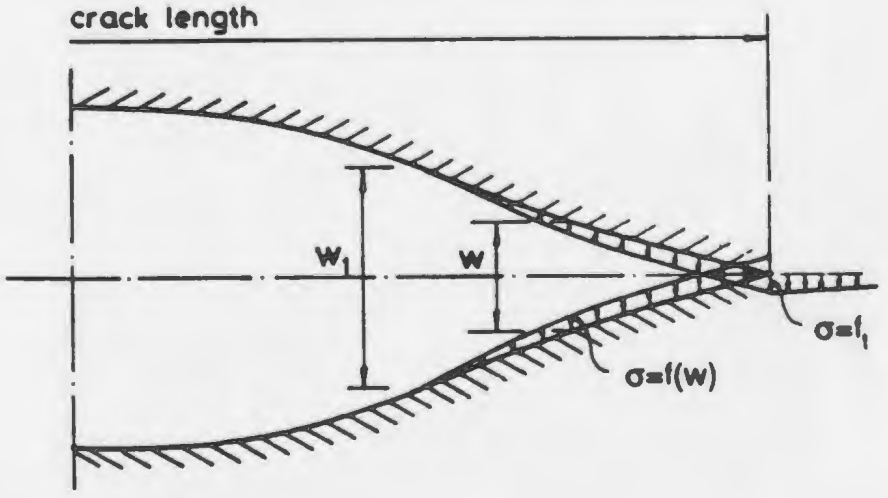

Figure 2.13: Fictitious crack model used in the fracture mechanics approach (Hillerborg, 1976)

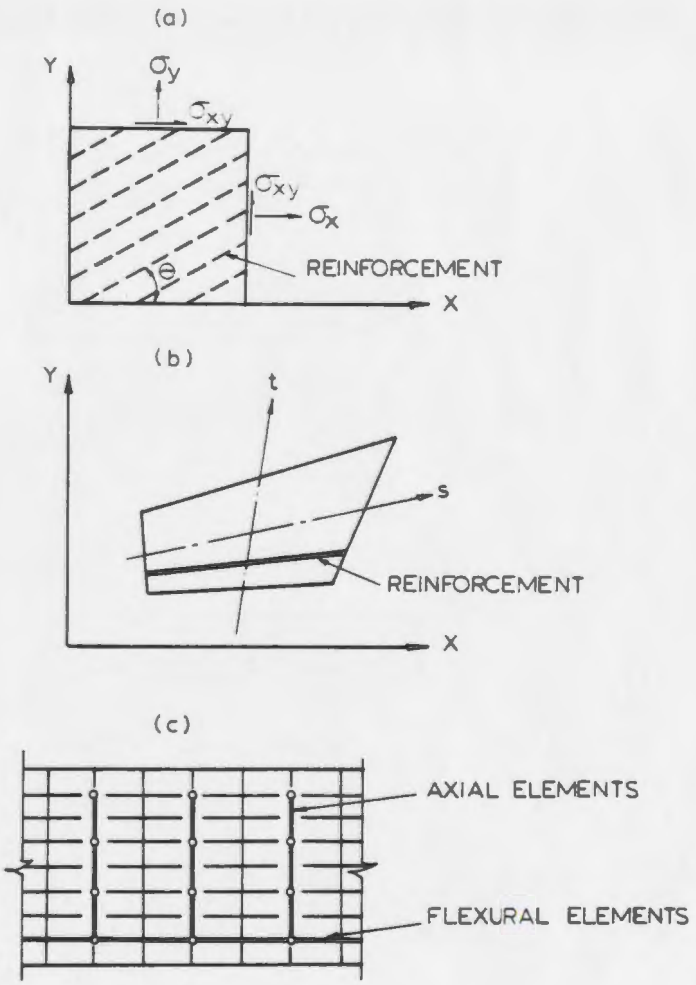

Figure 2.14: Alternative representations of reinforcement (ASCE, 1982) (a) distributed reinforcement (b) embedded reinforcement (c) discrete reinforcement

2.4.5.1 Distributed representation

In this approach, the steel is assumed to be distributed over the concrete element, with a particular orientation angle θ. A composite concrete-reinforcement constitutive relation is usually used. In order to derive such a relation, perfect bond must be assumed between the concrete and steel (e.g. Lin and Scordelis 1975, and Schnobrich 1977).

2.4.5.2 Embedded representation

In the case where higher order isoparametric elements are used, an embedded representation can also be used (e.g. Phillips and Zienkiewicz, 1976). The reinforcing bar is considered to be an axial member built into isoparametric element such that its displacements are consistent with those of the element. Again perfect bond must be assumed.

2.4.5.3 Discrete representation

A one-dimensional steel element is used in this approach (e.g. Nilson, 1968). Axial force members or bar links may be used and assumed to be pin connected with two degrees of freedom at the nodal points. Alternatively, beam elements may be used, assumed to be capable of resisting axial force, shear, and bending; in this case, three degrees of freedom are assigned at each end. In either case, the one-dimensional reinforcement elements are easily superimposed on a two-dimensional finite element mesh such as might be used to represent the concrete. A significant advantage of the discrete representation, in addition to its simplicity, is that it can account for possible displacement of the reinforcement with respect to the surrounding concrete.

The selection of these approaches is dependent on the nature of the problem to be analysed. For particular types of problems, a combination of these three representation may also be used (ASCE, 1982).

2.4.6 Computational difficulties and solution strategies

The accuracy and efficiency of finite element analysis of reinforced concrete structures is largely dependent on the proper description of material behaviour. Computational problems of alternative equilibrium states, perhaps due to non-uniqueness of the equilibrium path, and occurrence of local limit points in a load-deflection analysis have been reported by Crisfield (1982a). These often cause numerical difficulties in solution convergence during nonlinear iterations. The difficulties were found to be related to the softening branch of the concrete complete stress-strain relation in tension.

In order to overcome these unique problems in the finite element analysis of reinforced concrete structures, various solution strategies have been developed. A detailed survey of different methods is presented by Crisfield (1982b). The solution strategies can usually be classified into two categories: the solution technique and iteration technique. The first approach determines the type of approach used to bring an analysis to a converged and adequate solution. Various approaches have been employed in research, namely, load control method, the constant arc-length method, the Quasi-Newton method, etc. The iteration techniques are limited to the standard and modified Newton Raphson methods and both are widely used in any of the solution techniques mentioned before. The stiffness matrix is updated at every iteration with the standard Newton Raphson technique whereas, the stiffness matrix at the

beginning of each load increment is used throughout the iteration process with the modified Newton Raphson method. The second approach is usually more economical in terms of computing time, but requires more iterations to obtain the convergence. Three commonly used iteration techniques are illustrated in Fig. 2.2.

Chapter 3

Experimental Investigation of the Tensile Behaviour of High-Strength Concrete

3.1 Introduction

3.1.1 General

Failure of reinforced concrete structures is usually initiated by cracking of plain concrete. The cracking process starts at a low tensile stress level associated with a very early load stage , and has a significant effect on the behaviour of the concrete structural member. After concrete cracks are developed, the concrete between two adjacent cracks is still capable of resisting tensile forces induced due to the inherent bond effect and aggregate friction interlock. This phenomenon has long been ignored in the common design practice. Recently, it has become increasingly evident that it is necessary to properly simulate the local energy release as cracks propagate in order to achieve accurate predictions of the responses of concrete structures, such as load-deflection characteristics, crack width, bond transfer and shear transfer phenomenon, and tension-softening of concrete between cracks.

Therefore, cracking has become a very important feature of concrete behavior. However, available information in the literature on the tensile properties of high-strength concrete is very scarce. To the best of the author's knowledge, there is no documented information on the softening response and complete load-deformation behaviour of high-strength concrete subjected to the uniaxial tension. Furthermore, any information that could be obtained was from tests of normal strength concrete under direct uniaxial tension. Considering the ever increasing application of high-strength concrete in heavy duty constructions and offshore application, there is a great need for information in this area which has prompted the present research.

3.1.2 Test methods

The terms tensile strength and stress-strain relationship in tension have no absolute meanings, but must be expressed in terms of the specific test procedure used. There are three test methods to determine the tensile strength of plain concrete. They can be classified into two categories: the direct tension test and the indirect tension tests that include the beam flexure test and splitting cylinder test.

Following the ASTM C292 and C78 the modulus of the rupture, a measure of tensile strength, can be obtained by testing a plain concrete prism in flexure. Another indirect measure of tensile strength can be obtained from splitting cylinder test by following ASTM C496 provision. The indirect tensile strengths, as calculated from the measurements of the indirect tension tests , are based on the elastic theory. Therefore, only the the direct tension test can provide the complete stress-strain diagram in tension beyond the elastic behaviour. However, there is no standard test procedure for direct tension tests, because of the difficulties associated with applying

a pure tensile force to a plain concrete specimen.

3.1.3 Experimental program

In this experimental investigation, all three test methods were used to study the tensile behaviour of plain high-strength concrete. At the outset, the experiments of plain high-strength concrete under direct uniaxial tension were conducted, in order to reveal its unique tensile behaviour including the post-cracking response. The corresponding indirect tension tests and compression tests of the identical material were followed. Then, the tensile behaviour of high-strength concrete in the cold ocean water environment were examined in terms of low temperature effect and exposure duration. The performance of the empirical expressions for indirect tensile strengths adopted by ACI Committee 363 (1992) were also evaluated against the test results. Finally, the recorded results from three different test procedures for concrete in tension are compared.

3.2 Direct uniaxial tension tests

This section presents the experimental investigation on the behaviour of plain high-strength concrete subjected to direct uniaxial tension. The special testing method is described in detail, which was developed in order to obtain reliable load-deformation behaviour of plain high-strength concrete in direct uniaxial tension, including post-cracking softening response. The strains in crack process zone and elongation for various gage lengths were measured during the tests, in order to characterize the tensile softening response.

The experimental investigation reported here was carried out with two main ob-

jectives: (1) to understand the nature of the softening response of plain high-strength concrete under direct uniaxial tension; and (2) to characterize the observed response analytically in order to reflect the tension softening behaviour in the nonlinear analysis of high-strength concrete structures (details in chapter 4).

3.2.1 Mix design

The production of quality high-strength concrete that will meet the requirement for workability and strength development demands more stringent requirements on material selection than for lower-strength concrete. In this study, local materials were utilized, based on the recommendations of earlier researchers and test results obtained at the concrete laboratory of Memorial University (Marzouk and Hussein, 1990).

The local coarse aggregate employed consisted mostly of crushed quartzite sandstone with a minor fraction of siltstone and shale, and with a maximum nominal size of 10 *mm*. Local fine aggregates that had an identical composition to the coarse aggregates were utilized in the mix. The fine aggregates consisted mainly of quartzite sandstone with a fineness modulus of 3.1. The selection of these specific aggregates was based on the observations by Blick (1973). In the mix, the ordinary portland cement (Type 10) CSA3-A55 with modified C3A content of about 6% as produced in Newfoundland, was used. A 12% replacement of cement by Type F fly ash and 8% replacement by silica fume were used on the basis of weight. A neutralized vinsol resin air-entraining agent, a nonchloride water-reducing agent of polyhydroxy carboxylic base was added. The superplasticizer of sulfonated naphthalene formaldehyde base was also included in the mix, in order to yield the desirable concrete workability, due to the smaller size of coarse aggregates used. Mix proportions for one cubic metre

of high-strength concrete are given in Table 3.1 along with the properties of fresh concrete obtained from the tests.

The sieve analysis of aggregates was conducted according to ASTM C 135. Tests for determination of specific gravity and absorption percentage were also carried out conforming to the ASTM C 127 and ASTM C 128, respectively. The grading and the physical properties of both fine and coarse aggregates are given in Tables 3.2 and 3.3 respectively.

3.2.2 Test specimens

A total of 22 specimens with dimensions of 20 x 75 x 300 *mm* were cast in special plexiglass molds fabricated for specimens. The fresh concrete was placed into the molds in three layers in order to yield specimens as compact as possible. Then, the molds were transferred onto a vibrating table and subjected to light vibration to facilitate the casting. The moulded specimens were covered with water saturated burlap and left in the casting room at 20 °C for 24 hours before being immersed in water and left to cure for another 27 days. The direct tension tests were carried out at the concrete age of about 28 days.

The direct tension specimens were notched on both edges. The notches were cut by a circular diamond concrete saw with notch dimensions of 11 *mm* deep and 3 *mm* wide respectively. The selection of notch dimensions was based on the fracture energy concept as explained later. The width of the fracture process zone (ω_c) is assumed to remain constant before and after cracking. In addition, the value of ω_c before cracking can be assumed to be equal to 2 times notch depth plus notch width, that is $\omega_c = 25$ *mm*. This is based on the assumption that the stress trajectories in cracking process

Table 3.1: Mix proportions for 1 m^3 of high-strength concrete and properties of fresh concrete

Cementing material kg		Aggregate & water kg		Chemical admixture ml		Fresh concrete property	
Cement	440	Fine	660	Air entraining agent	360	Slump	9.4 mm
Fly ash	66	Coarse	1100	Retarder	17600	Air content	4.2 %
Silica Fume	44	Water	165	Superplasticizer	13200	Density	2390 kg/m^3

Table 3.2: Grading of aggregates

Coarse aggregate		Fine aggregate	
Sieve size	Cumulative percentage passing	Sieve size	Cumulative percentage passing
11.1 mm	95.00	4.75 mm (No. 4)	99.94
9.50 mm	77.90	2.36 mm (No. 8)	81.00
6.40 mm	35.30	1.18 mm (No.16)	48.00
4.75 mm	19.40	600 μm (No. 30)	30.08
		300 μm (No. 50)	15.05
		150 μm (No.100)	5.50
		Pan	1.50

Table 3.3: Physical properties of aggregates

Physical properties	Coarse aggregate	Fine aggregate
Bulk specific gravity, SSD	2.615	2.684
Apparent specific gravity	2.640	2.804
Absorption, Percentage	0.568	0.532

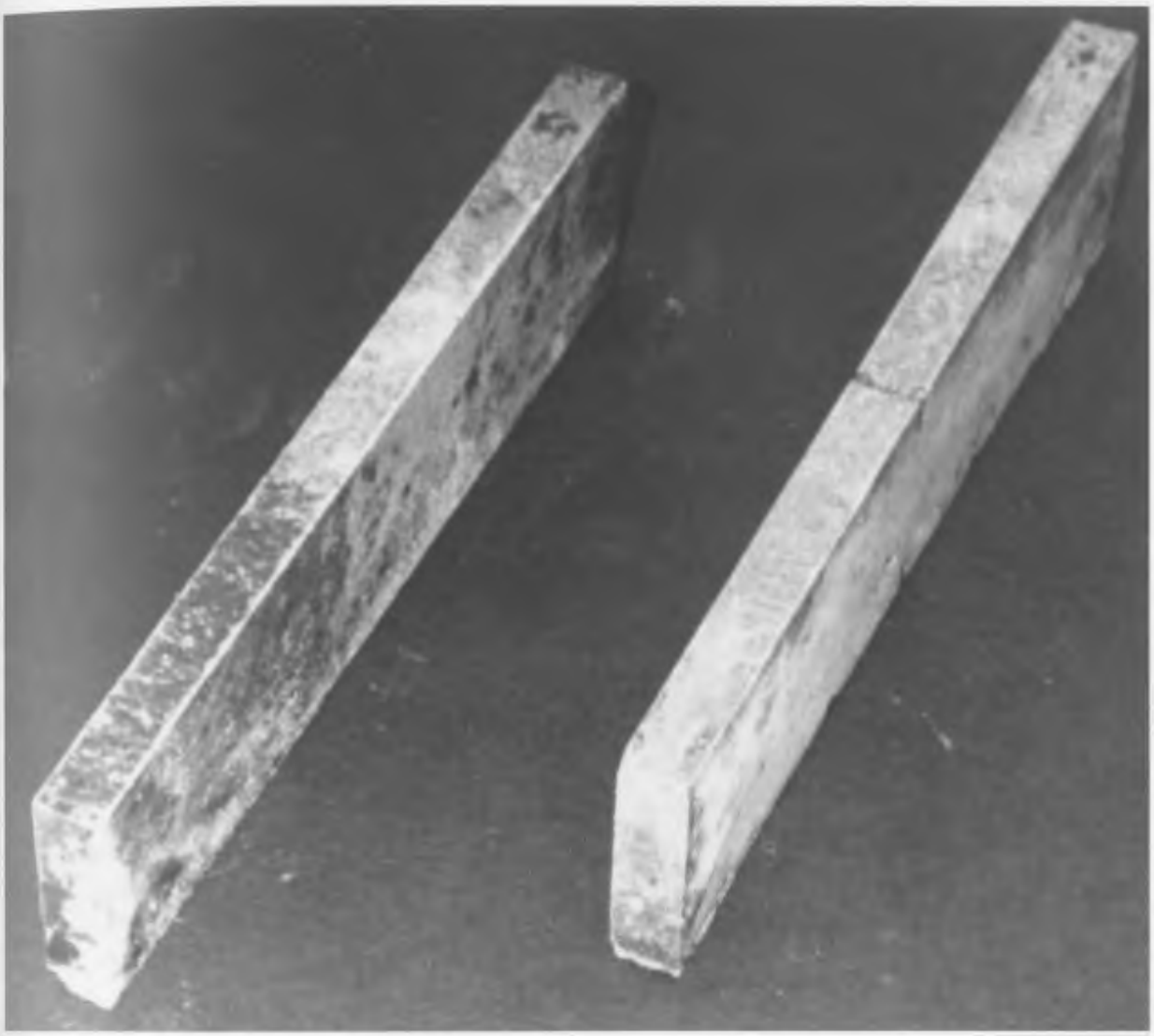

Figure 3.1: Tension specimens with double notches

zone expand at a 45 degree angle into other regions away from it on either side. This also prompts that an extensometer of 25 mm gage length be used across each notch in order to measure the cracking deformation in the fracture process zone. Hence, ω_c was 2.5 times d_{max}, the maximum nominal aggregate size (10 mm). The ratio of ω_c to d_{max} fell into the normal range of 1.5 to 4.0 for various types of concrete as stated by Bazant and Oh (1983), based on their extensive analysis of several test results obtained from various researchers and performed on different types of test set-up.

It was observed that there was no microcracking introduced due to the cutting process. The finished direct tension specimens before testing are shown in Fig. 3.1. The notched specimens were selected based on the observations that the average responses of the notched and unnotched specimens were identical, and both notched and unnotched specimens failed at a single critical section (one major crack), as reported by Gopalaratnam and Shah (1985).

3.2.3 Test set-up

Two main problems are usually encountered in testing of brittle, tension-weak materials in direct tension: the inability to eliminate total failure of the specimen at or near the grips where uniaxial stress conditions do not exist, and the inability to obtain stable post-peak response. In this study, a special test setup was fabricated in order to overcome these two problems. The test set-up is similar to that developed by Gopalaratnam and Shah (1985).

Inevitably some modification and refinement to the experimental arrangements and test procedure were made in response to the difficulties encountered and experience gained. Only the final experimental setup is described here but other salient

points are also highlighted.

The testing system consisted of a closed-loop servohydraulic universal testing machine, a pair of special wedge-type frictional grips, and a high-speed data acquisition system. The frictional grips and fixture attachment to the specimen are shown in Fig. 3.2. The special wedge-type friction grips were designed to assure that the fracture could occur away from the grips. The grips consisted of self-clamping steel and aluminum wedges and a universal joint connection to the loading machine. This allowed freedom of rotation along coordinate axes and eliminated the possibility of inducing end moments in the specimens. The wedge action was provided by sliding soft aluminum wedges over angled steel wedges. A 5 mm thick layer of gasket rubber with double surfaces serrated was introduced between the specimen and vertical face of aluminum wedges in order to enhance the friction interaction between wedges and specimen. This also allowed a uniform transfer of shear stresses from the grips to the concrete specimens. The steel wedges on each vertical face were held together by four ties which applied a moderate amount of pressure on the specimen surface prior to the application of the test load. It was shown that the self-clamping force of grips was sufficient enough to hold a specimen until it broke into two pieces.

3.2.4 Instrumentation

A servohydraulic universal testing machine was employed with a rigid loading frame throughout the tests in this study. The loading system consisted of a hydraulic actuator and load cell with maximum capacity of 100 kN and 91 kN respectively. The actuator had a piston area of 48.9 cm^2 with a dynamic and static stroke capacity of 152 mm and 168 mm respectively. Both tension and compression can be monitored

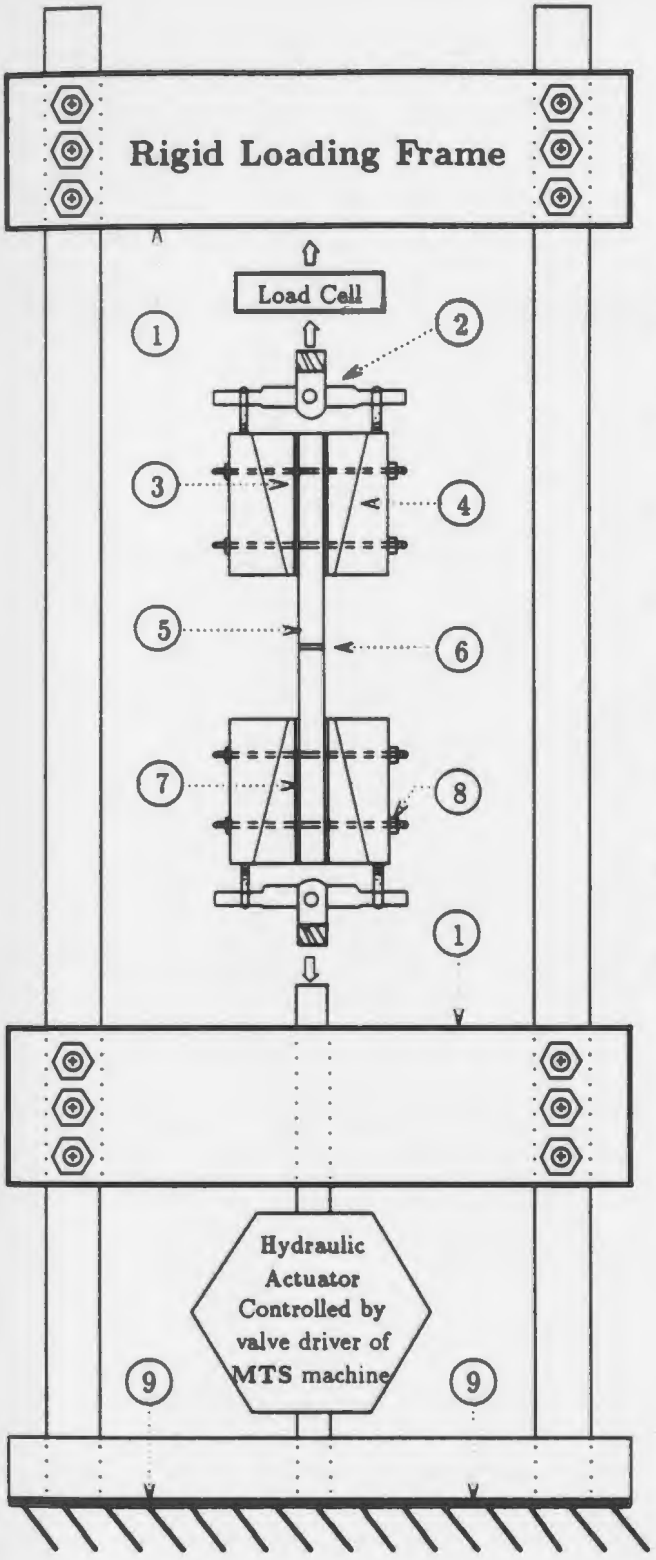

Legend:

1. Ajustable cross beam
2. Universal joint
3. Aluminium wedge
   (100 x 75 x 10-30 mm)
4. Frictional steel loading wedge
   (100 x 115 x 20-40 mm)
5. High-strength concrete specimen
   (300 x 75 x 20 mm)
6. Saw-cut notch on both sides of specimen
   (3 x 11 x 20 mm)
7. Double faces serrated rubber padding
   (100 x 75 x 5 mm)
8. Threaded tie rods and nuts
   (ϕ=10 mm)
9. Loading frame connected to ground

Figure 3.2: Loading frame and wedge-type frictional grips used for direct tension test

through the load cell employed.

The test controlling system, MTS 850 structure test system, consisted of an MTS 410 Digital Function Generator, MTS 413 Master Control Panel, MTS 417 Counter Panel and MTS 430 Digital Indicator. Tests can be performed with three modes, namely, load control, stroke control and strain control. The strain control testing technique was utilized throughout the tests.

The specimen was placed in parallel to the two columns of the rigid loading frame and loaded to maintain a constant rate of specimen deformation. It was observed that a specimen could fail in an unstable manner when a feedback signal to the servocontroller was used to control the rate of loading through an MTS built-in linear variable differential transducer (LVDT) with a gage length of 200 mm. This was due to the partial unloading of some parts of the specimen away from the crack after cracking was initiated in the specimen. As a result, even though the total elongation increased at the controlled rate, local deformations immediately across the crack increased drastically, sometimes resulting in a premature and unstable failure. Failure was less likely to occur if a smaller gage length was used for the feedback signal. However, with a smaller gage length, the possibility of cracking outside the gage length increased. If a crack formed outside the gage length unstable failure could occur. This dichotomy was avoided in the present investigation by providing a notch at the center of the specimen on both its sides and using the deformation across the notch through a electromechanical extensometer (gage length of 25 mm) to control the loading (Fig. 3.3). This arrangement insured a stable post-peak response. The test set-up is shown in Fig. 3.4.

In order to obtain the strain distribution in the crack process zone, six electrical

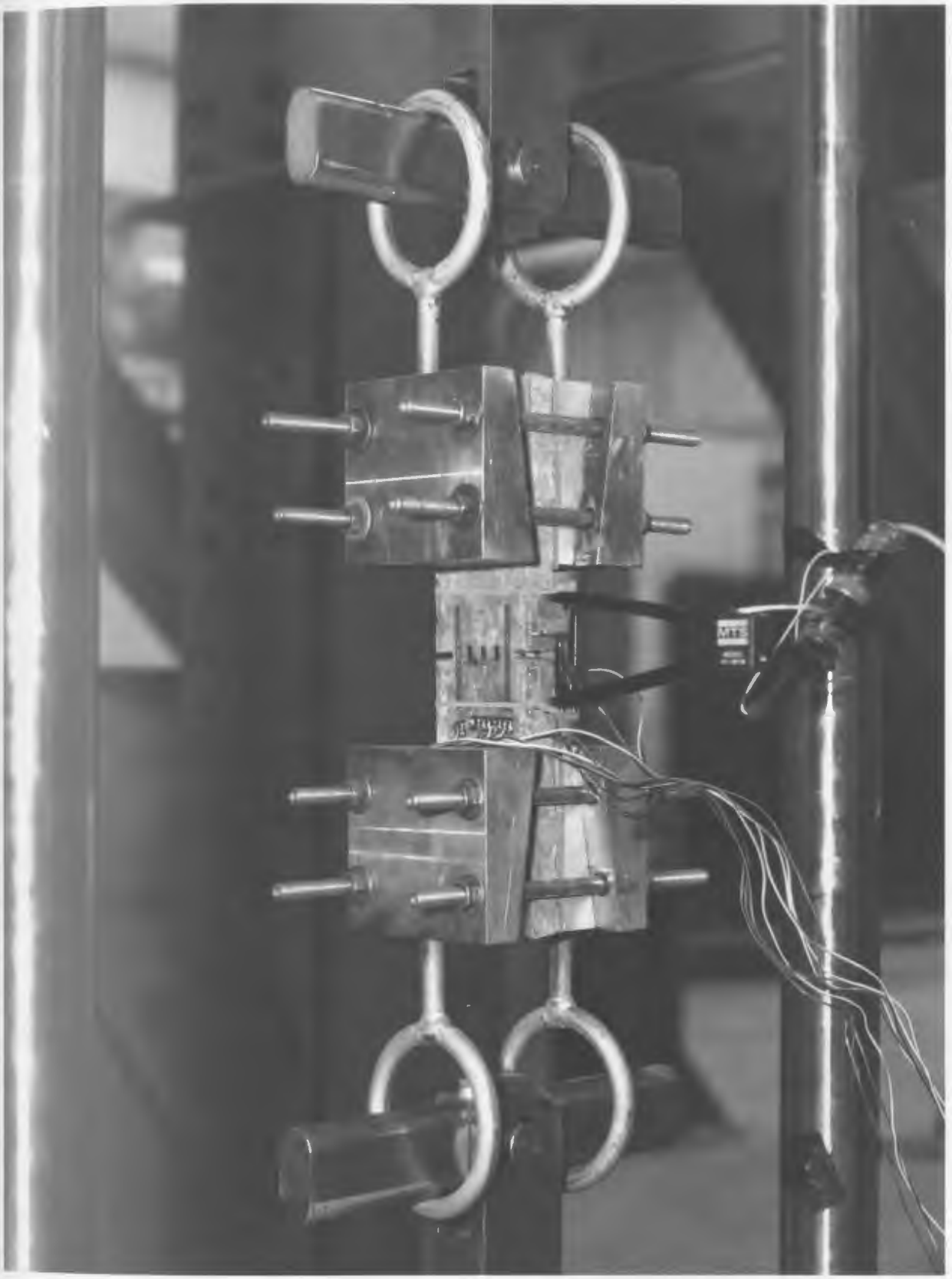

Figure 3.3: Close-up of a mounted tension specimen

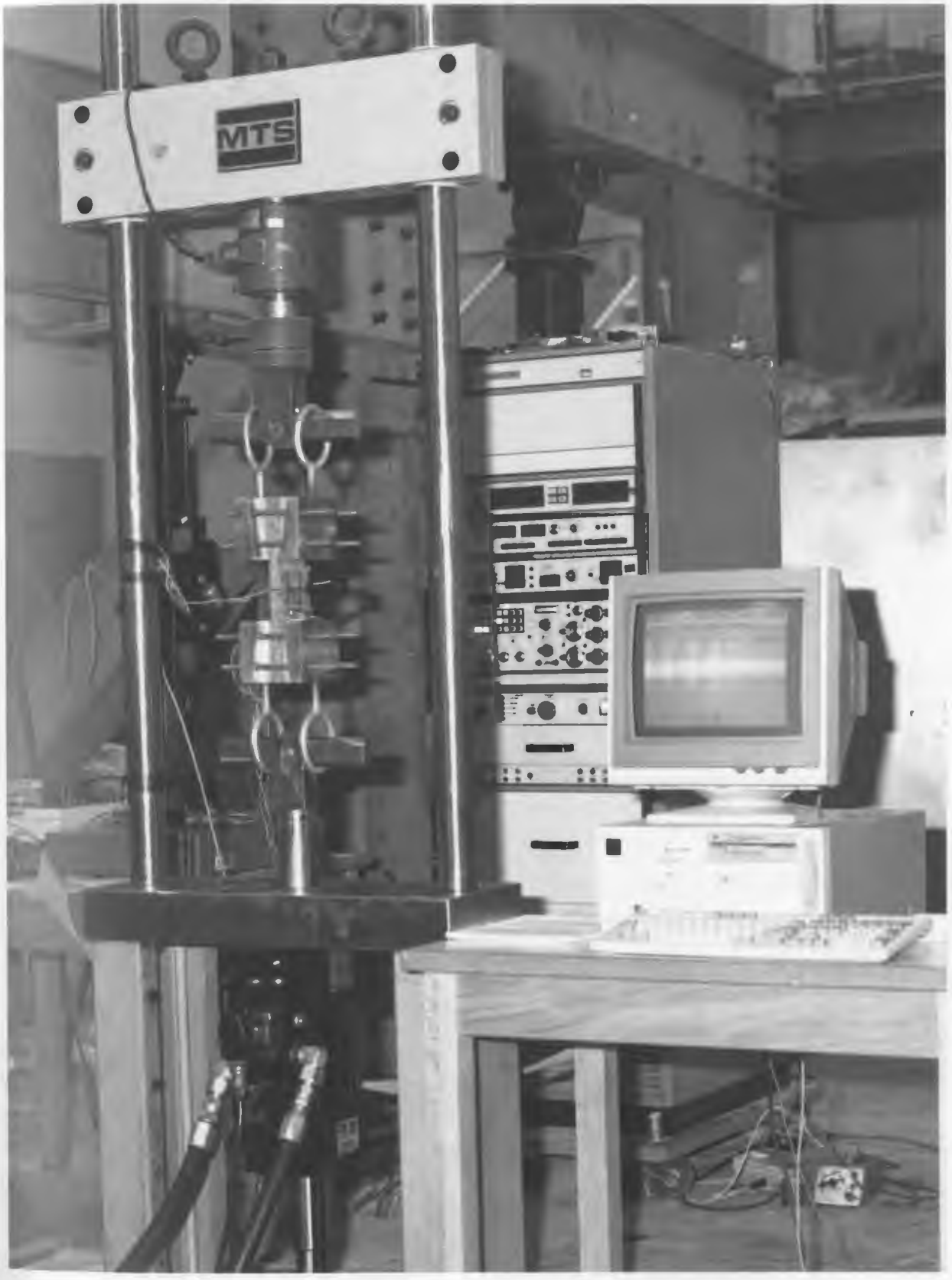

Figure 3.4: Test set-up and instrumentation for f'_t

resistance strain gages and four special concrete strain gages with gage length of 6 mm and 50 mm, respectively, were attached to both faces of some specimens (Fig. 3.5). The output of the strain gages along with the load and deformation data was automatically logged into the data aquisition system (System 200, from Sciemetric Instruments INC) and later processed for analysis. The output of the electromechanical extensometer and the load data were simultaneously logged into the X-Y Recorder (Hewlett Packard, Model 7046A) during the test. The general arrangement of the closed-loop test scheme and associated instrumentation is highlighted in the block diagram (Fig. 3.6).

3.2.5 Test procedure

The strain-controlled tests of plain high-strength concrete in direct uniaxial tension were performed as described previously. The load was applied with a hydraulic actuator controlled through a closed-loop universal testing machine in strain operating mode. Total testing time for each specimen was about 4 hours with an approximate strain rate of $0.02\mu\varepsilon$ per second. The slow strain rate was employed in an attempt to record a significant part of the descending branch of the complete stress-strain curve and to minimize the effect of the machine energy release. It was observed that higher strain rate usually resulted in a premature and unstable failure. This could be attributed to the more brittle nature of high-strength concrete as compared to lower strength concrete.

Readings from load cell and electromechanical extensometer were constantly displayed and monitored through the HP X-Y Recorder. The output of strain gages together with load and deformation data were continuously scanned and recorded

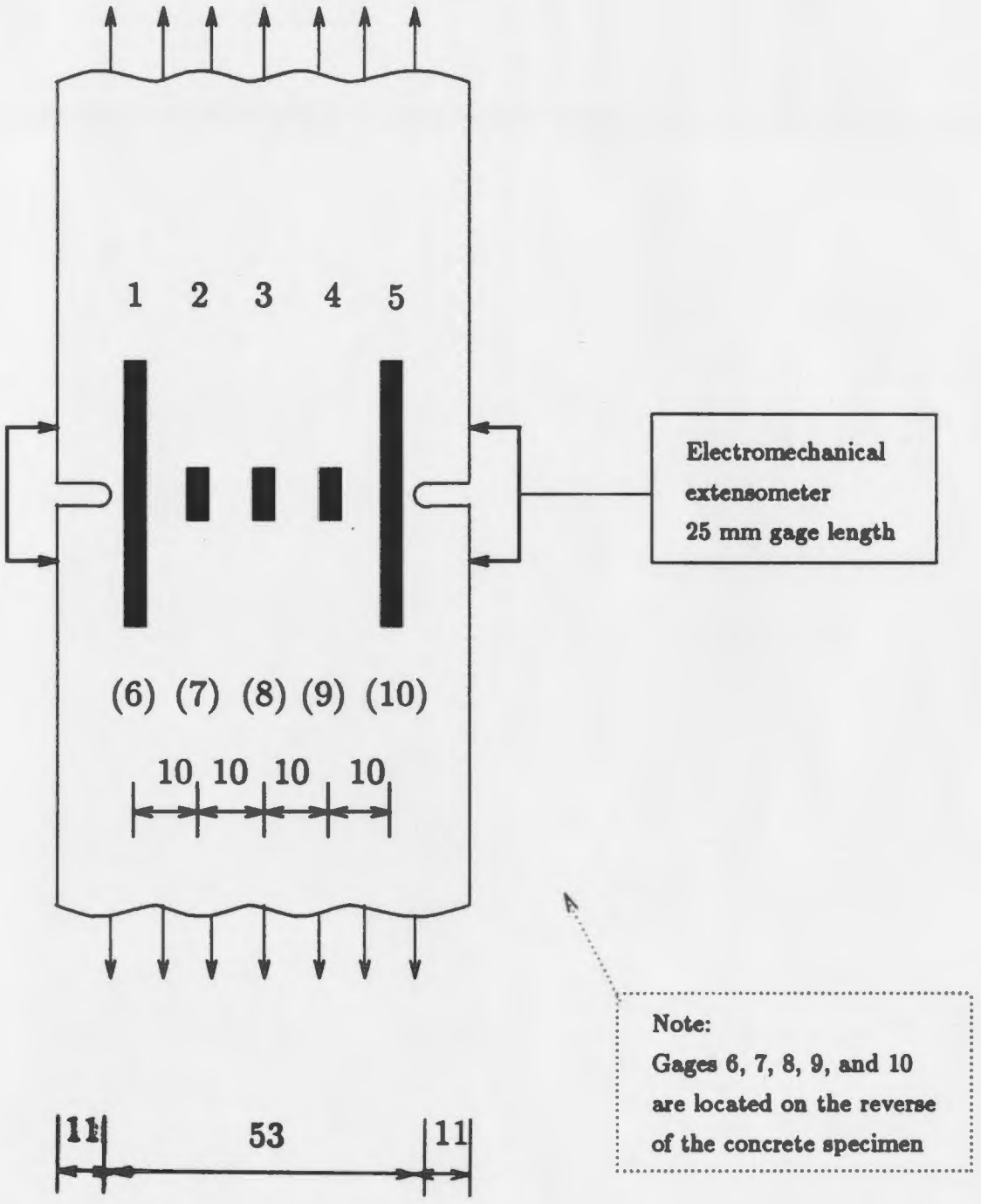

Figure 3.5: Strain gage arrangements

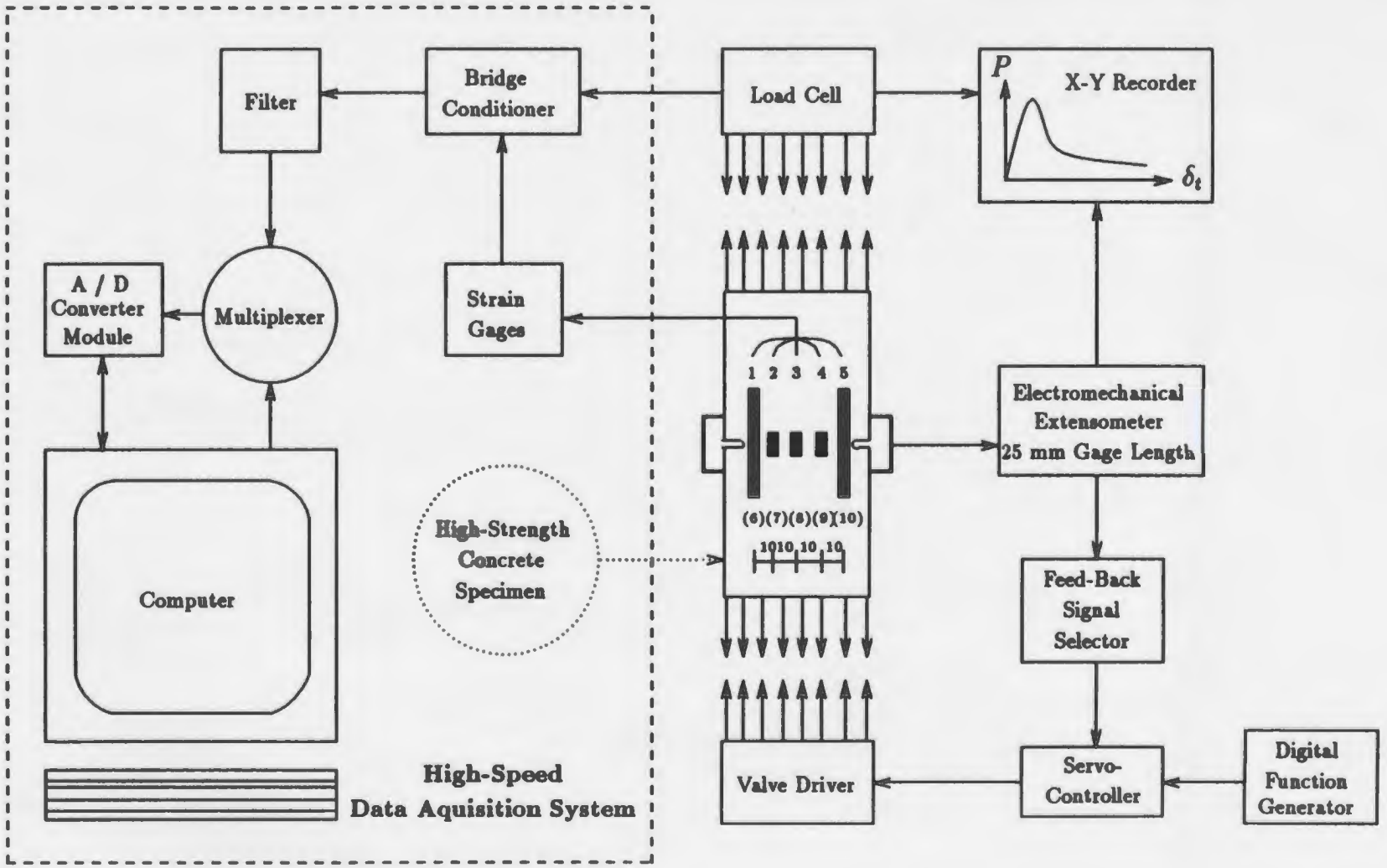

Figure 3.6: Test instrumentation and block diagram of the closed-loop test

into a data aquisition system and constantly displayed through the use of a computer.

3.2.6 Experimental observation and discussion

3.2.6.1 Stress-deformation curves

Test results of some specimens reflected a stable failure and a complete load-deformation curve as shown in Figs. 3.7, 3.8 and 3.9. The deformation of these specimens was perfectly under control. Stress and strain increased proportionally up to an elastic limit of about 50% of the maximum stress. Thereafter, the strain increased more quickly and the stress-strain curve began to respond nonlinearly. The maximum tensile stress was reached when the corresponding strain was measured between 100.5 and 136.9 $\mu\epsilon$; the curve then descended sharply. It was observed that the cracking was initiated at one side of the specimen soon after peak load, at the point where the electromechanical extensometer was mounted. A single crack propagated towards the other end of the specimen. No cracks were observed prior to the peak load, although other investigators have reported microcracks prior to the peak load (Terrien 1982 and Hillerborg 1985).

As the crack developed, the load decreased and cracking deformation increased slowly. A crack developed gradually across the width of the section when the total cracking deformation was about 3.5-4.5 times the deformation at peak stress. The corresponding residual load was about 20 to 30 percent of the maximum load due to a small residual tensile area and aggregate interaction of the cracking section. It can be seen that the specimens exhibited a substantial post-cracking tensile resistance. The cracked surfaces appeared to be connected and/or bridged by aggregates or crystals

and the observed cracking deformation was only a measure of the average separation of these surfaces. The ten strain gage measurements indicated that after cracking the cracking strains increased sharply, while the strains on the other parts away from the cracking zone decreased as load decreased.

Finally, the single crack through the section widened so much that the specimens were broken into two pieces. Most parts of the broken section passed through the aggregates; a minor percentage passed through the cementing materials. A close-up photo of a specimen after cracking is presented in Fig. 3.10.

3.2.6.2 Mechanical properties

Some of the average material properties obtained from the tests which yielded a complete load-deformation (p-δ) curve are summarized in Table 3.4. Values reported herein include the peak stress and corresponding strain (f'_t,ϵ_{to}); initial modulus of elasticity E_0 and secant modulus of elasticity at peak stress E_p; and the corresponding ratios of the initial modulus to the secant modulus at peak E_0/E_p. The initial modulus of elasticity E_0, is defined as the secant modulus at the stress of $\frac{1}{2}f'_t$. The statistical analysis of the corresponding test results was also completed in this study.

It can be obtained from the statistical analysis that the test results are quite consistent and reliable. In comparison, results of the strain at peak ϵ_{to} and initial modulus E_0 were more scattered with a coefficient of variation of 12.7% and 12.5% respectively. The coefficient of variation for peak stress f'_t and corresponding secant modulus were 7.7% and 7.6% respectively. The mean peak stress was 3.29 MPa, ranging from 3.07 to 3.62 MPa with a standard deviation of 0.26 MPa. The strain varied between 100.5-136.9 $\mu\epsilon$ with a mean value of 119.6 $\mu\epsilon$ and a standard deviation

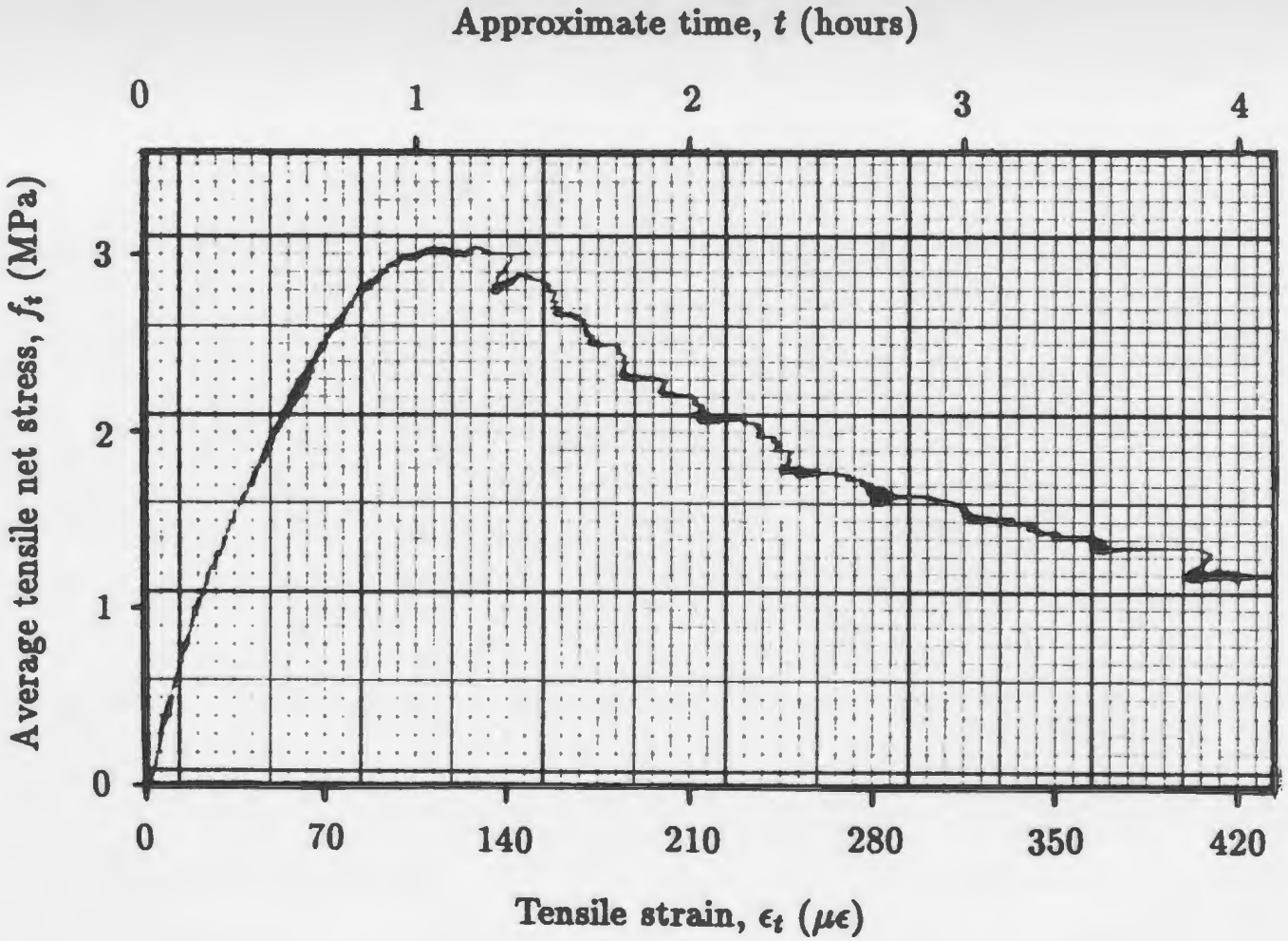

Figure 3.7: Typical stress-strain curve for a high-strength concrete specimen under direct tension (strain measurements across the notch through a 25 *mm* gage length extensometer)

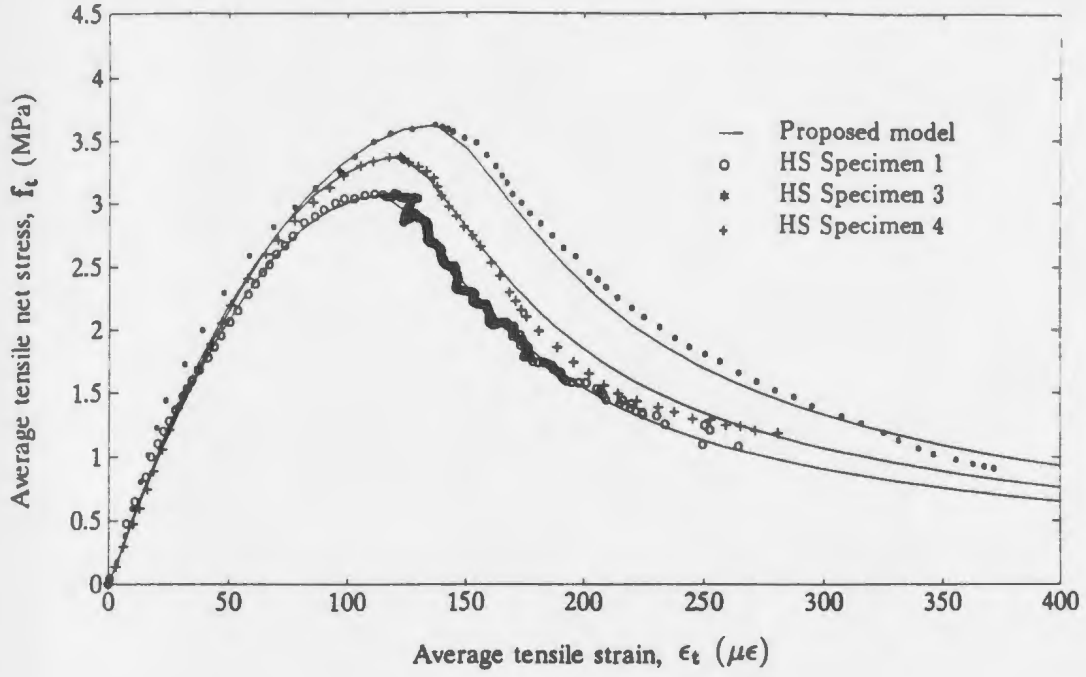

Figure 3.8: Tensile stress-strain measurement (specimens HS1, HS3, and HS4)

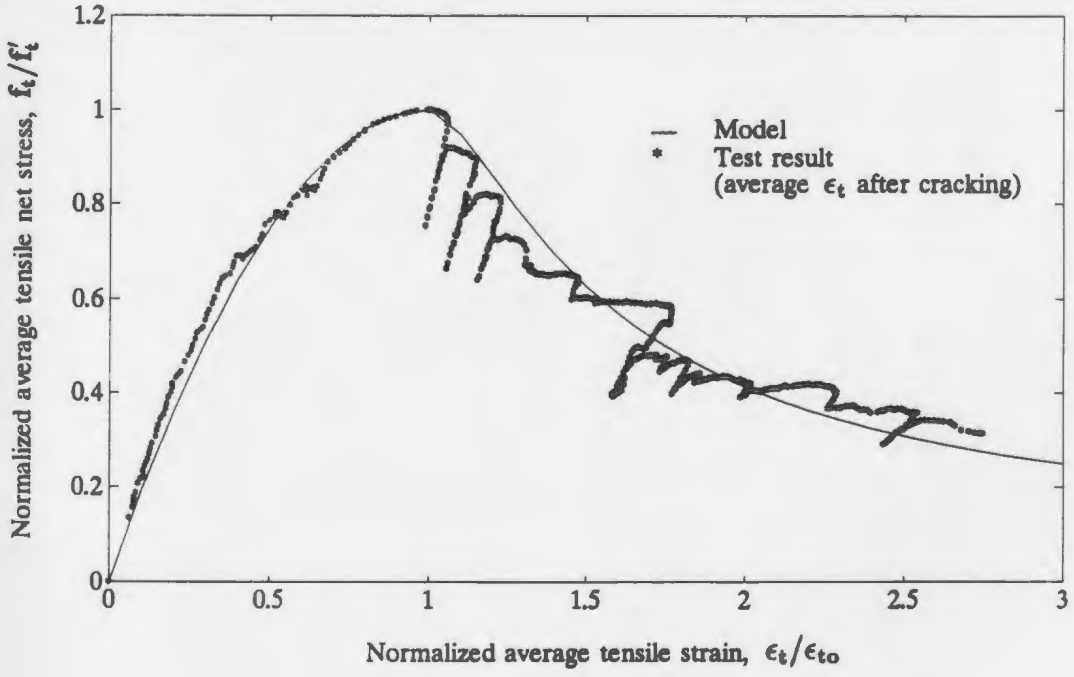

Figure 3.9: Normalized tensile stress-strain measurement (specimen HS2)

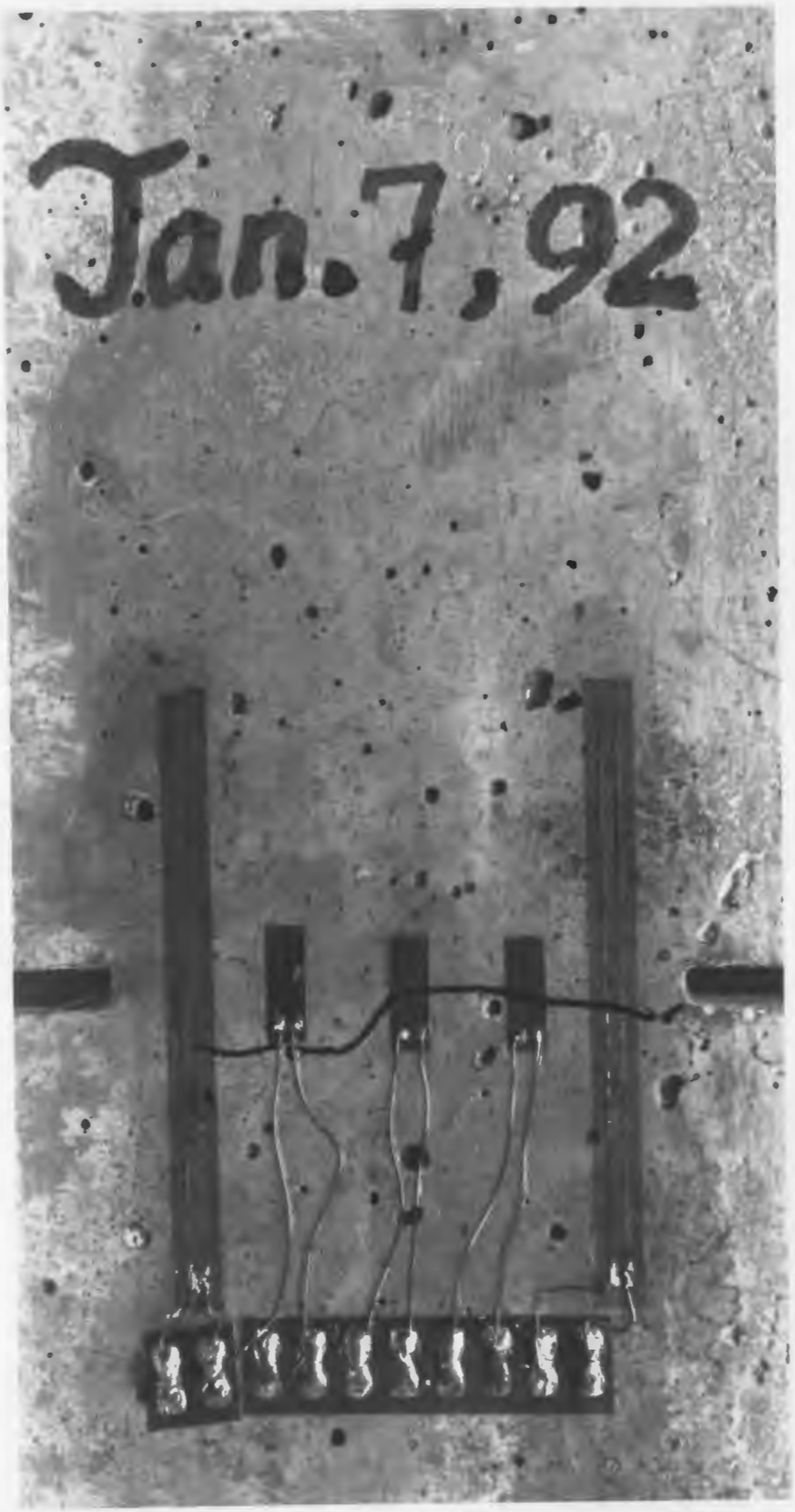

Figure 3.10: A close-up of a specimen after cracking

Table 3.4: Typical results of high-strength concrete specimens under direct tension (stable p-δ curve)

Specimen dimension mm	f'_c MPa	Experimental measurement	Direct tension test specimen designation			
			HS 1	HS 2	HS 3	HS 4
20 x 75 x 300	74.154*	f'_t, MPa	3.067	3.118	3.620	3.369
		ϵ_{to}, $\mu\epsilon$	114.9	100.5	136.9	122.0
		E_0, kN/mm^2	47.01	59.81	52.97	45.82
		E_p, kN/mm^2	26.69	31.03	26.44	27.62
		E_0/E_p	1.761	1.928	2.003	1.659

*Determined from compression tests of corresponding standard concrete cylinders (152.5 x 305mm)

of 15.1 $\mu\epsilon$. The large mean ratio (E_0/E_p=1.84) of initial modulus to secant modulus at peak may indicate the severe material nonlinearity of high-strength concrete in the ascending branch of stress-strain curve.

3.2.7 Summary

High-strength concrete exhibits a appreciable post-cracking resistance under direct tension as shown in Figs. 3.7, 3.8 and 3.9. The descending branch of the complete stress-cracking strain curve in direct tension is due to the reduction of the effective tensile area. The observed post-cracking resistance of high-strength in direct tension can be explained due to the residual effective tensile area and bridging of cracked surfaces through the interaction of aggregates and fibrous crystals. The concrete post-peak softening response is related to widening of a single crack developed across the section. Generally, the crack occurs at the weakest part of the critical section and spreads gradually across the critical notched section. After cracking, the cracking strains increase sharply, while the strains on the other parts away from the cracking zone decrease as load decreases.

The initial modulus of elasticity of high-strength concrete in tension is high, with a mean value of 51.40×10^3 kN/mm^2, due to the brittle nature of high-strength concrete. The relatively severe nonlinearity of the ascending branch of the average stress-strain curve of high-strength concrete in tension beyond the elastic limit was observed, as indicated by the ratio of the initial modulus to the secant modulus at peak stress.

In general, the strain at peak stress (ϵ_{to}) increased proportional to the tensile strength. The measured values are between 100.5-136.9 $\mu\epsilon$. The recorded tensile

strains were more scattered than the measured tensile strengths. The tensile strength of high-strength concrete in direct tension was measured to be approximately equal to $4.8\%f'_c$.

The testing scheme developed in this study for high-strength concrete in direct tension is capable of performing the required tests and yielding a complete stress-cracking deformation relation.

3.3 Indirect tension tests

3.3.1 Experimental observations

Tests on the modulus of rupture and splitting tensile strength of high-strength concrete were performed, in order to evaluate the empirical expressions adopted by ACI Committee 363 (1992). The indirect tensile strengths were obtained from the two different sets of specimens. The first set tests, used to obtain the modulus of rupture, were conducted on 75 x 75 x 300 *mm* prisms loaded at midpoint on a 300 *mm* span with a closed-loop MTS testing machine. The tests were conforming to the procedure of ASTM C78 (Fig. 3.11). The second set tests, used to obtain the splitting tensile strength, were conducted on 152 x 305 *mm* standard concrete cylinders loaded through a 2670 kN (600 Kips) Soiltest compression testing machine according to ASTM C496 procedure (Fig. 3.12).

The corresponding compression tests of the identical concrete at the age of about 28 days were also conducted at the room temperature in order to determine the compressive strength. The test results are given in Tables 3.5 and 3.6.

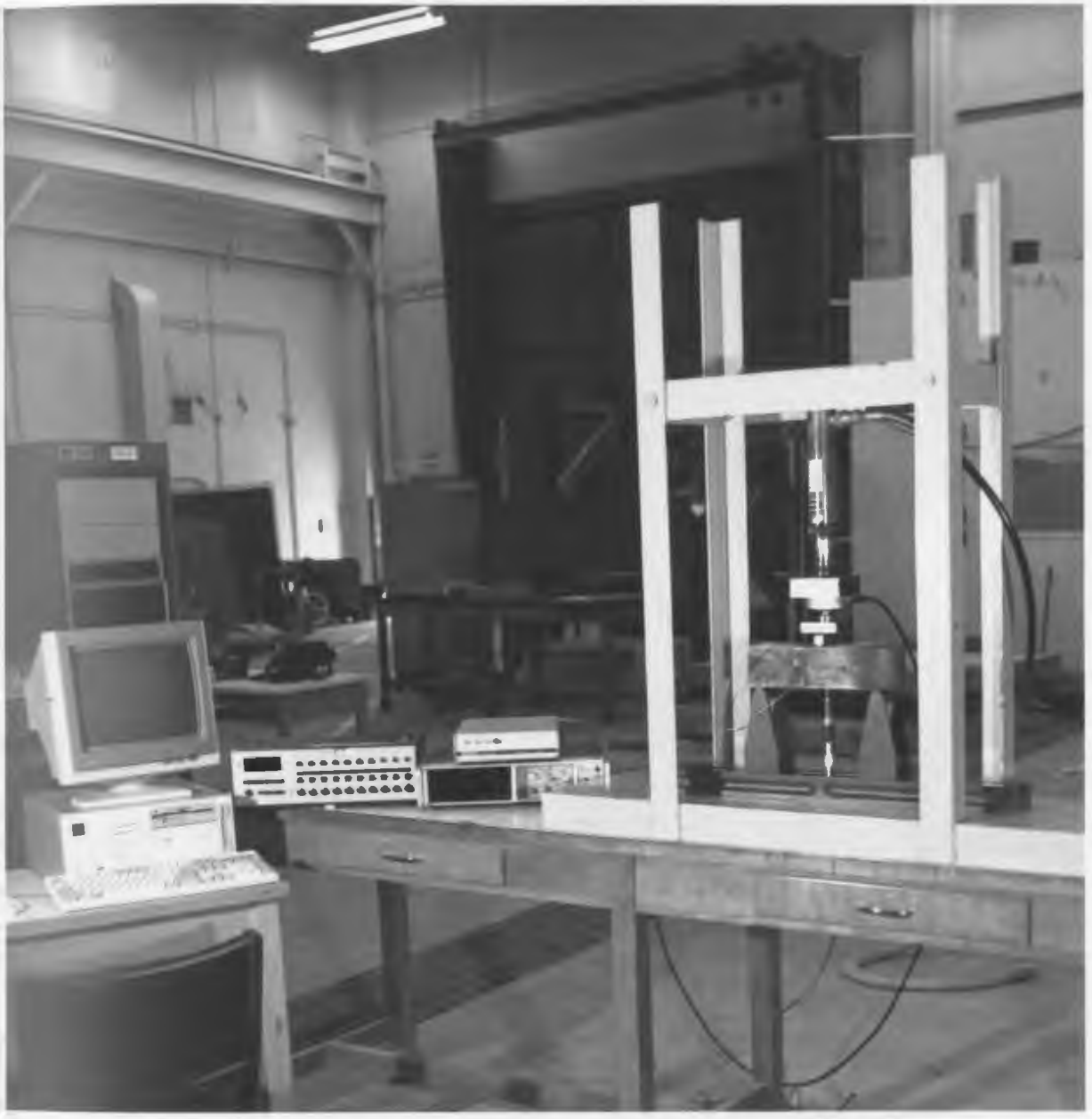

Figure 3.11: Test set-up and instrumentation for f'_r

Figure 3.12: Test set-up and instrumentation for f'_{ct}

Table 3.5: Comparison of ACI Expression to test results (f'_{ct}, Eq. 3.1)

f'_c (MPa)	Age (Days)	ACI f'_{ct} (MPa)	Test f'_{ct} (MPa)	ACI Test
69.1	28	4.86	4.95	0.98
68.8	28	4.86	5.12	0.95

Table 3.6: Comparison of ACI Expression to test results (f'_r, Eq. 3.2)

f'_c (MPa)	Age (Days)	ACI f'_r (MPa)	Test f'_r (MPa)	ACI Test
69.1	28	7.73	7.16	1.08
68.8	28	7.73	6.44	1.20

3.3.2 Evaluation of the ACI empirical expressions

Based on the values reported by various investigators, the ACI Committee 363 (ACI, 1992) recommended the following equations for the predictions of the indirect tensile strengths, as measured by the splitting tensile strength and modulus of rupture from the corresponding compressive strength:

$$f'_{ct} = 0.59\sqrt{f'_c} \ \ MPa \tag{3.1}$$

$$f'_r = 0.94\sqrt{f'_c} \ \ MPa \tag{3.2}$$

where,

f'_{ct} = Splitting tensile strength

f'_r = Modulus of rupture

f'_c = Concrete compressive strength

The predictions of Eqs. 3.1 and 3.2 are compared to the experimentally determined values at the room temperature. The comparisons are made with respect to a very common concrete test age of 28 days and are presented in Tables 3.5 and 3.6. It is found that the empirical expressions adopted by ACI Committee 363 (1992) provided fairy good estimates of splitting tensile strength and modulus of rupture.

3.4 Relation of tensile and compressive strengths

In order to illustrate the relationship of the compressive and tensile strengths of high-strength concrete, the compression tests and three types of tension tests were conducted on the same material. More experimental results of direct tensile strength

were obtained that are given in Table 3.7. The corresponding experimentally determined values of compressive strength and modulus of rupture are listed in Tables 3.8 and 3.9 respectively.

The values of modulus of rupture were determined under midpoint loading. The related prism-shaped specimens were additionally cast for this comparison study, using the same mix proportion as for the specimens in direct tension, splitting and compression tests. The results are presented in Table 3.10.

3.4.1 Variability of tensile and compressive strengths

The test measurement are summarized in Table 3.11 together with the results of related statistical analysis. It can be seen that the results of compressive strength were very consistent with a variation coefficient of only 4.8%. The most scattered results were associated with the direct tensile strength that had a variation coefficient of 13.1%. This could be attributed to the nature of concrete, where coarse aggregate articles are distributed randomly and aggregate-mortar bond strength differs from the tensile strength of mortar itself (detailed in section 3.2.6). Therefore, concrete responded more unfavourably in tension than in compression.

3.4.2 Relation of tensile and compressive strengths

It was observed that the direct tensile strength was only recorded as 4.8% f'_c, where f'_c was the measured compressive strength of the identical material. The splitting tensile strength was about 7.2% f'_c, whereas the modulus of rupture was about 9.4% f'_c (Table 3.12).

It was found that the modulus of rupture values (f'_r) were about 30 percent higher than tensile strength measured from the splitting test. The measured splitting tensile

Table 3.7: Direct tensile strength of high-strength concrete (f'_t, MPa)

Tension specimen dimensions (mm)	Mean* compressive strength f'_c (MPa)	Recorded direct tensile strength f'_t (MPa)					Statistical analysis		
							Mean strength (MPa)	Standard deviation (MPa)	Coefficient of variation
20 x 75 x 300	74.154	3.067	3.118	3.620	3.369	3.369	3.526	0.461	13.1%
		3.519	2.846	3.118	3.570	4.224			
		4.022	4.123	4.073	3.771	3.469			
		3.369	3.318	2.715	4.626	3.419			
		3.483	3.519	-	-	-			

*Determined from compression tests of corresponding standard concrete cylinders (152.5 × 305mm)

Table 3.8: Compressive strength of high-strength concrete (f'_c, MPa)

Standard cylinder dimensions (mm)	Compressive strength f'_c (MPa)					Statistical analysis		
	No. 1	No. 2	No. 3	No. 4	No. 5	Mean strength (MPa)	Standard deviation (MPa)	Coefficient of variation
152.5 x 305	70.250	77.080	70.740	74.640	78.060	74.154	3.569	4.8%

Table 3.9: Splitting tensile strength of high-strength concrete (f'_{ct}, MPa)

Splitting cylinder dimensions (mm)	Mean* compressive strength f'_c (MPa)	Splitting tensile strength f'_{ct} (MPa)			Statistical analysis		
		No. 1	No. 2	No. 3	Mean strength (MPa)	Standard deviation (MPa)	Coefficient of variation
152.5 x 305	69.133	4.750	5.220	4.890	4.953	0.241	4.9%

*Determined from compression tests of corresponding standard concrete cylinders with dimensions of 152.5 × 305mm

Table 3.10: Modulus of rupture of high-strength concrete (f'_r, MPa)

Flexural prism dimensions (mm)	Mean* compressive strength f'_c (MPa)	Modulus of rupture f'_r (MPa)				Statistical analysis		
		No. 1 & 2	No. 3 & 4	No. 5 & 6	No. 7 & 8	Mean strength (MPa)	Standard deviation (MPa)	Coefficient of variation
76 x 76 x 305	68.8	7.196	6.930	6.663	6.575	6.441	0.572	8.9%
		6.663	5.775	5.508	6.219			

*Determined from compression tests of corresponding standard concrete cylinders (152.5mm x 305mm)

Table 3.11: Variability of tensile and compressive strengths of high-strength concrete

Type of test	Mean strength MPa	Standard deviation MPa	Coefficient of variation
Direct tension test, f'_t	3.526	0.461	13.1%
Splitting tension test†, f'_{ct}	4.953	0.241	4.9 %
Modulus of rupture*, f'_r	6.441	0.572	8.9 %
Compression test, f'_c	74.154	3.569	4.8 %

†The corresponding compressive mean strength was 69.1 MPa
*The corresponding compressive mean strength was 68.8 MPa

Table 3.12: Relation of compressive and tensile strengths of high-strength concrete

f'_c MPa	$\frac{f'_t}{f'_c}$	$\frac{f'_{ct}}{f'_c}$	$\frac{f'_r}{f'_c}$	$\frac{f'_{ct}}{f'_t}$	$\frac{f'_r}{f'_t}$	$\frac{f'_r}{f'_{ct}}$
69.133	-	0.072	-			
74.154	0.048	-	-	1.500*	1.958*	1.306*
68.800	-	-	0.094			

*Normalized values were used in calculation

strength was about 50 percent higher than the direct tensile strength. In addition, the measured modulus of rupture was almost 200 percent of direct tensile strength.

3.4.3 Summary

Various types of tension tests have been used for plain high-strength concrete testing: the direct tension test, the modulus of rupture test, and the splitting test. The results from three kinds of tests were considerably different (Table 3.11). The measured modulus of rupture and splitting tensile strength were about 100 percent and 50 percent higher than the measured direct tensile strength. As experimentally observed, only the direct tension test could provide the complete stress-deformation diagram in tension beyond the elastic behaviour. All the specimens in both modulus of rupture and splitting tests resulted in a sudden failure.

High-strength concrete is relatively weaker in tension compared to normal strength concrete, when compared to the corresponding compressive strength. The measured direct tensile strength was as low as 4.8 percent of the corresponding compressive strength measured. The splitting tensile strength was measured as 7.2 percent of compressive strength, whereas it could be as high as 10 percent for lower strength concrete (Dewar, 1964). This indicated that the tensile strength of high-strength concrete did not increase at the same rate as the compressive strength increased.

3.5 Effect of low ocean water temperature

3.5.1 Experimental details

For the sake of simplicity, only the indirect tensile strengths were examined with respect to the low ocean water temperature, in order to illustrate its effect on the

tensile behaviour of high-strength concrete. A total of over 40 concrete cylinders and 80 concrete prisms was tested for determining the modulus of rupture and splitting tensile strength respectively. The mix proportions were the same as those used for direct tension specimens (section 3.2). The moulded specimens were covered with water saturated burlap and left in the casing room at 20 °C for 24 hours. They were then demoulded and transferred to the water tanks until required for testing.

The five water tanks were filled with ocean water with different temperatures of 20 °C, 10 °C, 0 °C, -5 °C and -10 °C respectively. At each temperature, two specimens were tested after being exposed to cold ocean water for 1, 7, 14 and 28 days.

The indirect tensile strengths were obtained from the two different sets of specimens. The first set tests, used to obtain the modulus of rupture, were conducted on 75 x 75 x 300 *mm* prisms loaded at midpoint on a 300 *mm* span with a close-loop MTS testing machine. The tests were conforming to the procedure of ASTM C78 (Fig. 3.11). The second set tests, used to obtain the splitting tensile strength, were conducted on 75 x 150 *mm* cylinders loaded through a 2670 kN (600 Kips) Soiltest compression testing machine according to ASTM C496 procedure (Fig. 3.12). The relatively small size specimens were employed, due to the size limitation of the water tanks.

3.5.2 Experimental observations and discussions

The experimentally measured values of splitting tensile strength and modulus of rupture are given in Tables 3.13 and 3.14.

As can be seen from Tables 3.13 and 3.14, strengths increased in general with exposure time at various temperatures. The strength gain with concrete age at the

temperature of 20 °C is presented in Table 3.15. The ratios of strengths at 7 days to 28 days were 0.72 and 0.78 for splitting tensile strength and modulus of rupture respectively. These values are higher than those of normal strength concrete that were reported as 0.7-0.75 (Parrot, 1969).

As temperature decreased, the strength gain with exposure time tends to be less. At temperature of 20 °C, the ratios of strength gain at 28 days to 1 day were 89% and 82% for splitting tensile strength and modulus of rupture respectively, while the strength gain ratios for the same period at the lowest test temperature of -10 °C were only 36% and 52%. The recorded testing data are graphically presented in Figs. 3.13 through 3.16 for splitting tensile strength and modulus of rupture respectively.

As revealed by recorded test results presented in Fig. 3.13 through Fig. 3.16, the low temperature and sulfate associated with cold ocean water had severely adverse effect on the indirect tensile strengths of high-strength concrete. This is due to the effect of cold ocean water on the cement hydration of high-strength concrete made with silica fume and fly ash.

The hydration of ordinary portland cement concrete at normal temperature consists mainly of calcium silicate hydrate, hydrates of calcium aluminates and calcium aluminate ferrites, and calcium hydroxides. Also, the hydrated products contain some quantities of unhydrated cement and water in both evaporable and nonevaporable forms. Furthermore, the calcium hydroxide (hydrated lime), which is the by-product of the hydration process, reacts at room temperature with the silica fume and fly ash to form tobermorite gel that has a very strong and stable cementing quality.

As the temperature decreased in the tests, the hydration process was slowed down. Hence, the rate of evolution of calcium hydroxide decreased. Therefore, the recorded

test results showed that the rate of strength gain tended to be less as temperature decreased.

The ocean water has a rich sulfate content. Normally, sulfate reacts with calcium hydroxide and calcium silicate hydrate to form gypsum and calcium sulfoalluminate. These newly formed compounds are much weaker and have greater volume that leads to the expansion and deterioration of concrete. Since the hydration process almost ceased at temperature of -10 °C, the calcium hydroxide was free to react with the sulfate. This reaction caused the lower rate of maturity and deterioration of concrete at lower temperatures. While at normal temperature, the pozzolanic reaction consumed free calcium hydroxide and rendered the aluminate-bearing phase inactive. Therefore, the sulfate attack had no evident effect on the strengths at room temperature of 20 °C.

Table 3.13: Effect of cold ocean water on the splitting tensile strength

Exposure time (Days)		1	7	14	28
f'_c (MPa)	Temperature (°C)	f'_{ct} (MPa)			
67.7	20	3.05	4.15	5.43	5.76
	10	2.93	4.09	4.63	4.83
	0	2.80	4.02	4.57	4.63
	-5	2.68	3.90	4.02	4.24
	-10	2.56	3.41	3.66	3.46

Table 3.14: Effect of cold ocean water on the modulus of rupture

Exposure time (Days)		1	7	14	28
f'_c (MPa)	Temperature (°C)	f'_r (MPa)			
67.7	20	3.82	5.42	5.55	6.93
	10	3.82	4.98	5.86	6.62
	0	3.38	4.62	5.24	5.91
	-5	3.64	4.39	4.69	5.86
	-10	3.55	4.22	4.18	5.42

Table 3.15: Strength gain with concrete age
(specimens at 20 °C)

MPa	Concrete age		Ratio of strength at 7 days to 28 days
	7 Days	28 days	
f'_{ct}	4.15	5.76	0.72
f'_r	5.42	6.93	0.78

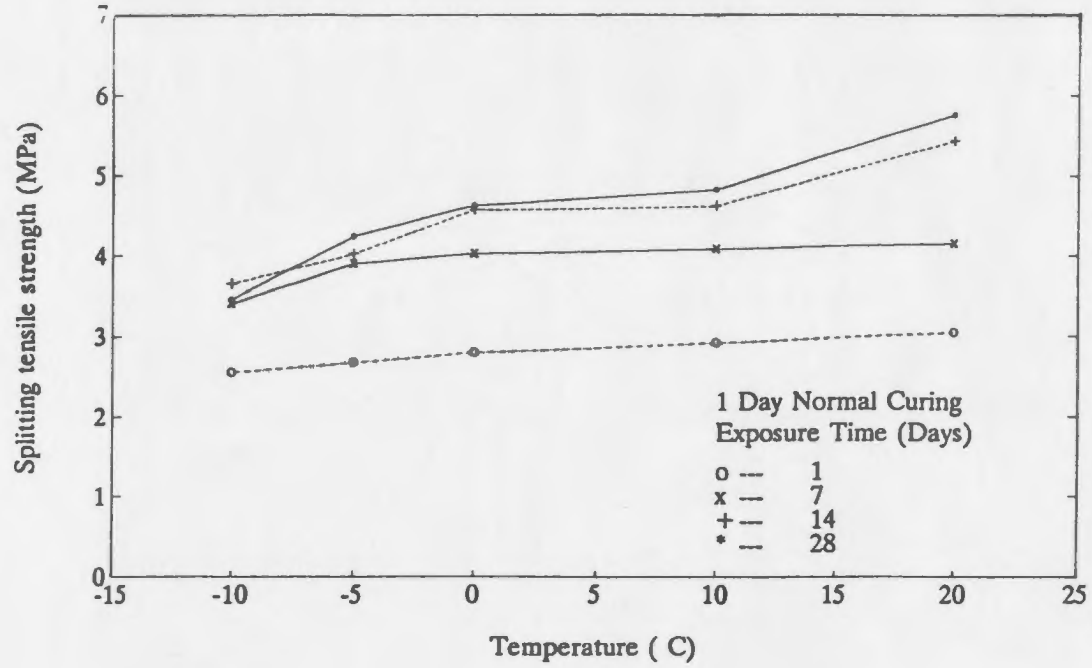

Figure 3.13: Effect of low temperature on f'_{ct}

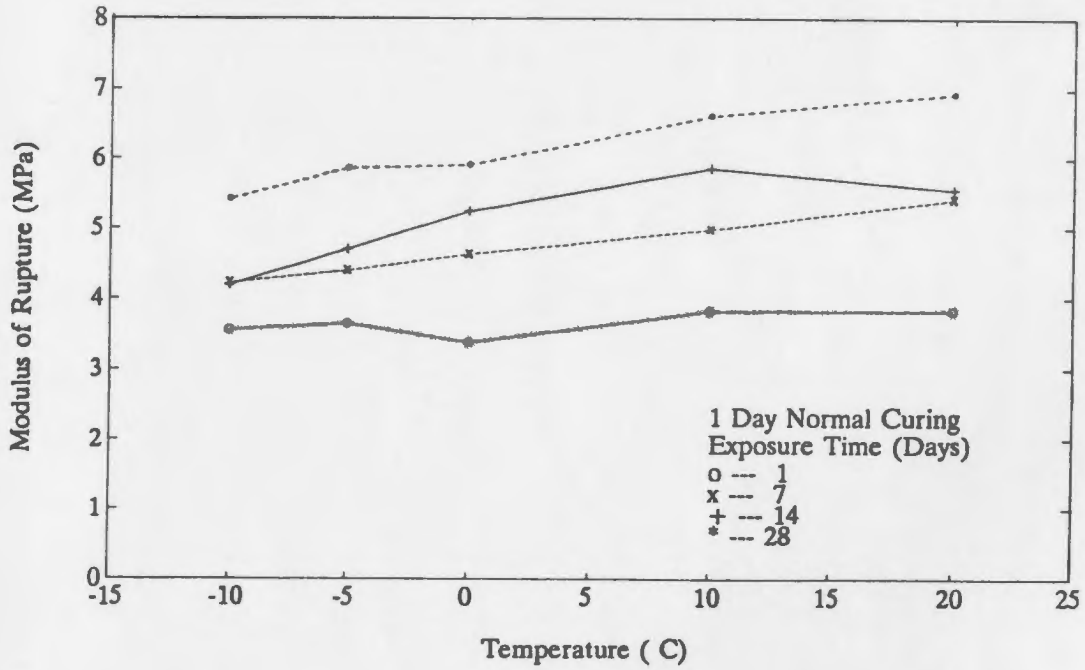

Figure 3.14: Effect of low temperature on f'_r

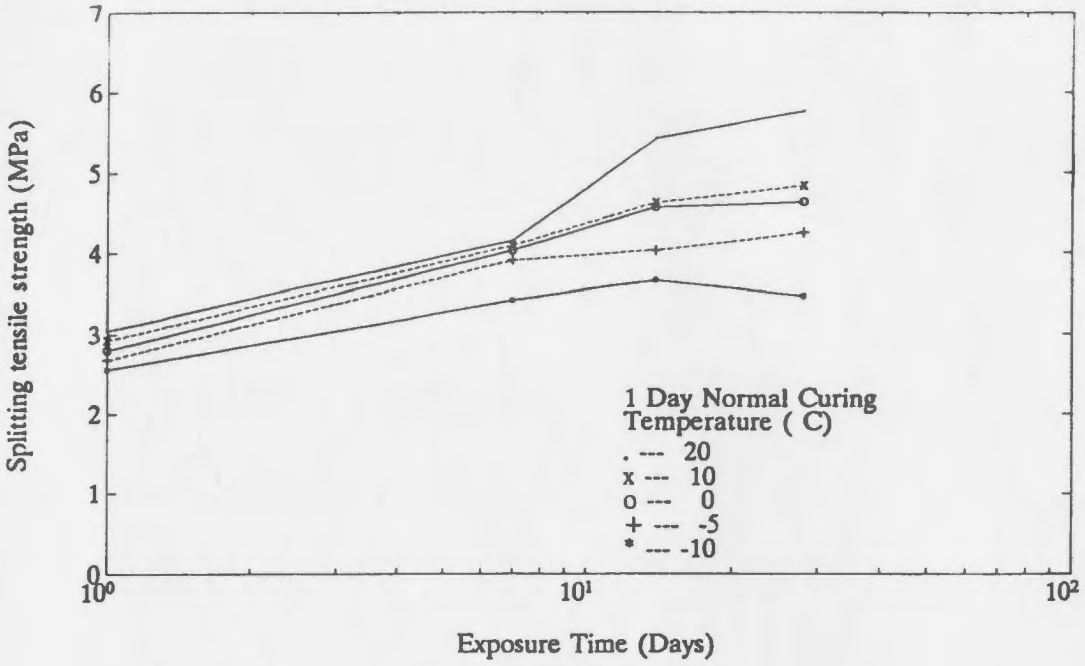

Figure 3.15: Effect of exposure time on f'_{ct}

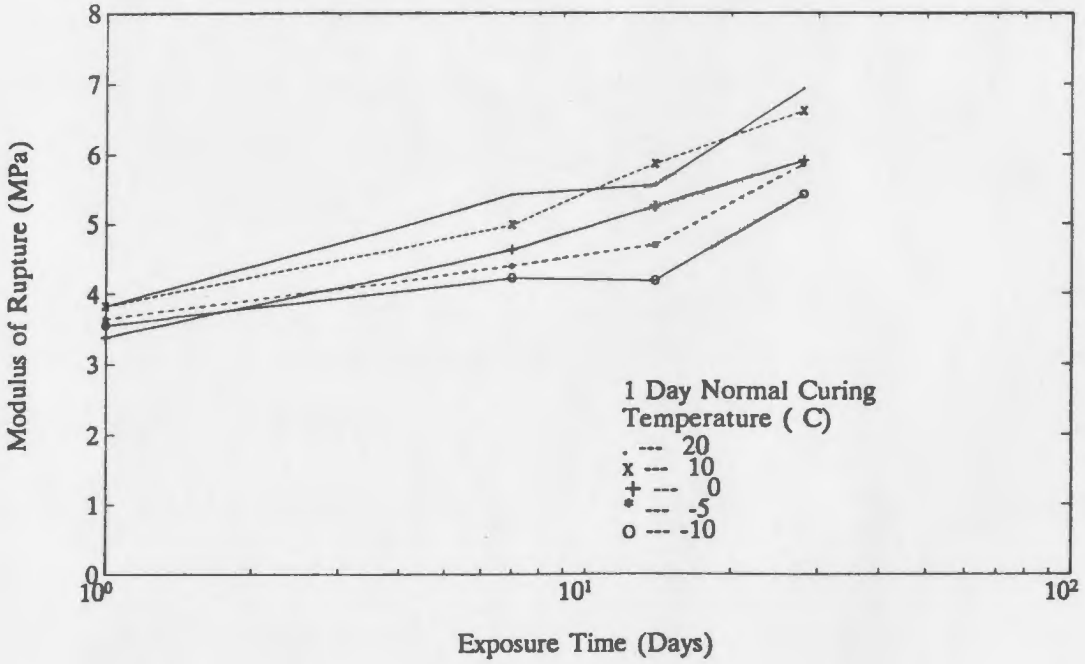

Figure 3.16: Effect of exposure time on f'_r

Chapter 4

Constitutive Relationship of High-Strength Concrete in Uniaxial Tension

4.1 Introduction

This chapter presents a recommended analytical expression by which measurements from high-strength concrete specimens tested under the direct uniaxial tension are characterized into a realistic tension softening model. The tension softening model is significant for any accurate nonlinear analysis of high-strength concrete structural members, since the cracking and post-cracking behaviour is a very important feature of high-strength concrete.

At the outset, the typical continuous tension softening models available for normal strength concrete are described. The performance of the existing models are evaluated against the test results of high-strength concrete. A realistic tension softening model for high-strength concrete is then developed, based on the experimental measurements obtained in this study. The understanding of tension softening nature of high-strength concrete is enhanced by comparison to that of lower-strength concrete in terms of

fracture energy, mechanical properties and entire load-deformation response.

4.2 Development of tension softening model for high-strength concrete

Various types of tension softening models have been proposed for plain concrete in uniaxial tension: linear, bilinear, exponential, rational, etc., as detailed in chapter 2. Usually, the existing models are only the appropriate representations of experimental behaviour of normal strength concrete specimens conducted individually. There is no common understanding in this area. Moreover, there is no documented data on the tension softening behaviour of high-strength concrete in uniaxial tension.

In an attempt to establish a tension softening model for high-strength concrete investigated in this study, three typical continuous tension softening models for normal strength concrete reported by Carreira and Chu (1986), Guo and Zhang (1987), and Gopalaratnam and Shah (1985) respectively were evaluated against experimental measurements obtained in this investigation. All three models selected have one important feature that they are continuous in stress-displacement relationships prior to and beyond the peak stress. Abrupt discontinuities in the stiffness are characteristic of linear approximations of the softening behavior and are likely to pose instabilities in certain numerical schemes. Therefore, the linear softening model should be avoided for the generality of application.

4.2.1 Typical continuous tension softening models for normal strength concrete

Carreira and Chu (1986) recommended a single serpentine curve to represent the average stress-strain response of concrete in tension that was exactly the same form

as suggested for concrete in compression, but with a different value of parameter β:

$$\frac{f_t}{f_t'} = \frac{\beta(\epsilon_t/\epsilon_{to})}{\beta - 1 + (\epsilon_t/\epsilon_{to})^{\beta}} \tag{4.1}$$

where,

f_t = the tensile stress corresponding to tensile strain ϵ_t

f_t' = direct tensile strength

ϵ_{to} = the tensile strain at peak stress f_t'

β = a parameter that depends on the shape of the stress-strain diagram

The average stress-strain relationship given in Eq. 4.1 represents the overall or resultant behaviour in tension and can be used for both plain concrete and reinforced concrete by a suitable choice of parameters β. Therefore, the combined effects of cracking, slippage, and bond along the reinforcement may be included.

In addition, two separate equations continued at peak stress were proposed to describe the complete stress-deformation relationship by Guo and Zhang (1987). A high order polynomial was suggested for the ascending branch to count for the stiff behaviour of concrete prior to cracking. For the descending branch, a rational polynomial was recommended with two adjustable parameters α and β that depend on the shape of the stress-strain diagram. These two equations are given as follows:

$$y = 1.2x - 0.2x^6 \qquad x \leq 1.0 \tag{4.2}$$

$$y = \frac{x}{\alpha(x-1)^{\beta} + x} \qquad x \geq 1.0 \tag{4.3}$$

where,

y = the relative stress f_t/f'_t

x = the relative strain ϵ_t/ϵ_{to}

The parameter β was suggested as 1.7 and α should be determined by the least square method for individual experimental curves of specimens. The complete stress-deformation curve is similar in shape to that recommended by Carreira and Chu (1986).

Furthermore, the concept of the stress-crack width relationship (f_t-ω) of concrete in tension was introduced by Gopalaratnam and Shah (1985) and Petersson (1981), rather than a stress-strain relationship. Gopalaratnam and Shah (1985) recommended two separate equations to describe the ascending and descending branches that were continuous at peak stress. A simple expression was proposed for the uniaxial tensile stress-strain curve up to the peak stress value:

$$f_t = f'_t[1 - (1 - \frac{\epsilon_t}{\epsilon_{to}})^A] \tag{4.4}$$

where,

A = $E_t\epsilon_{to}/f'_t$

E_t = initial tangential modulus of concrete

f_t, f'_t, ϵ_t, and ϵ_{to} are same as those previous defined

The value of A is always greater than one for any material exhibiting pre-peak nonlinearity. As a result, the slope of stress-strain curve is always zero at the peak. For the descending part, the unique relationship between stress-crack width was suggested as:

$$f_t = f'_t(e^{-k\omega^\lambda}) \tag{4.5}$$

where,

ω = the crack width

k, λ = the constants

For the sake of continuity at the peak, the constant λ was assumed as 1.01. For this value of λ, a value of k = 1.544 x 10^{-3} was recommended (when ω was expressed in microinches), based on the best fit to the experimentally determined values of f_t-ω diagram. In order to obtain displacement for any gage length or finite element mesh size, the strains in the ascending portions are simply multiplied by the gage length. In the descending portion, the total displacement is given by

$$\begin{aligned} \delta &= \delta_e + \delta_{pd} + \omega \\ &= \frac{f_t}{K_t} + (\delta_p - \frac{f_t'}{K_t}) + (-\frac{1}{k} \ln \frac{f_t}{f_t'})^{1/\lambda} \end{aligned} \tag{4.6}$$

where the various terms are defined in Fig. 2.11j. The first two terms are gage length dependent quantities, while the third term is independent of gage length. The gage length dependence, however, vanishes at large displacements. A smooth transition is achieved from the ascending portion, where the stress-strain relationship is unique, to the softening region, where the stress-crack width relationship is unique. This formulation eliminates the need to subscribe to characteristic lengths attributed by some other investigators as a material or a finite element mesh property.

4.2.2 Evaluation of the existing tension softening models

Comparisons of three typical continuous models to test results are presented in Fig. 4.1 through Fig. 4.3, respectively, where the existing models are optimized in the

post-cracking region with the least square method to fit the test data obtained in this study. In Figs. 4.1 and 4.2, the relative average cracking strain is used. The average cracking strain is calculated as the ratio of the measured deformation over the gage length. In Fig. 4.3, the stress is plotted as a function of relative average cracking width. The average cracking width is denoted as ω. The parameter of ω_t used in the Fig. 4.3 is equal to $(\omega+\delta_p)$, where δ_p is the concrete tensile deformation at the peak load. Actual crack width of a specimen should be the difference between the reading of the deformation transducer and the deformation of uncracked concrete. Since the latter is negligible, measured deformation is considered as the average crack width of concrete.

It should be noted that the relative or normalized deformation is used in the comparisons, in order to eliminate any possible effects of gage length, loading speed, etc. Therefore, the proposed model will have a broader application.

It has been found that among the three selected models, Guo and Zhang (1987) expression (Eq. 4.3) appears to be the best in describing the post-peak response of high-strength concrete, after optimization of the model in the post-peak region with respect to the test data of high-strength concrete.

4.2.3 Recommended tension softening model for high-strength concrete

Based on the test evidence obtained in this experimental investigation (refer to chapter 3), an analytical model is recommended for plain high-strength concrete in the uniaxial tension. This model assumes a realistic stress-deformation relationship . It is similar to the expression proposed Guo and Zhang (1987) for normal strength concrete in the post-peak region. The parameters α and β are determined from results

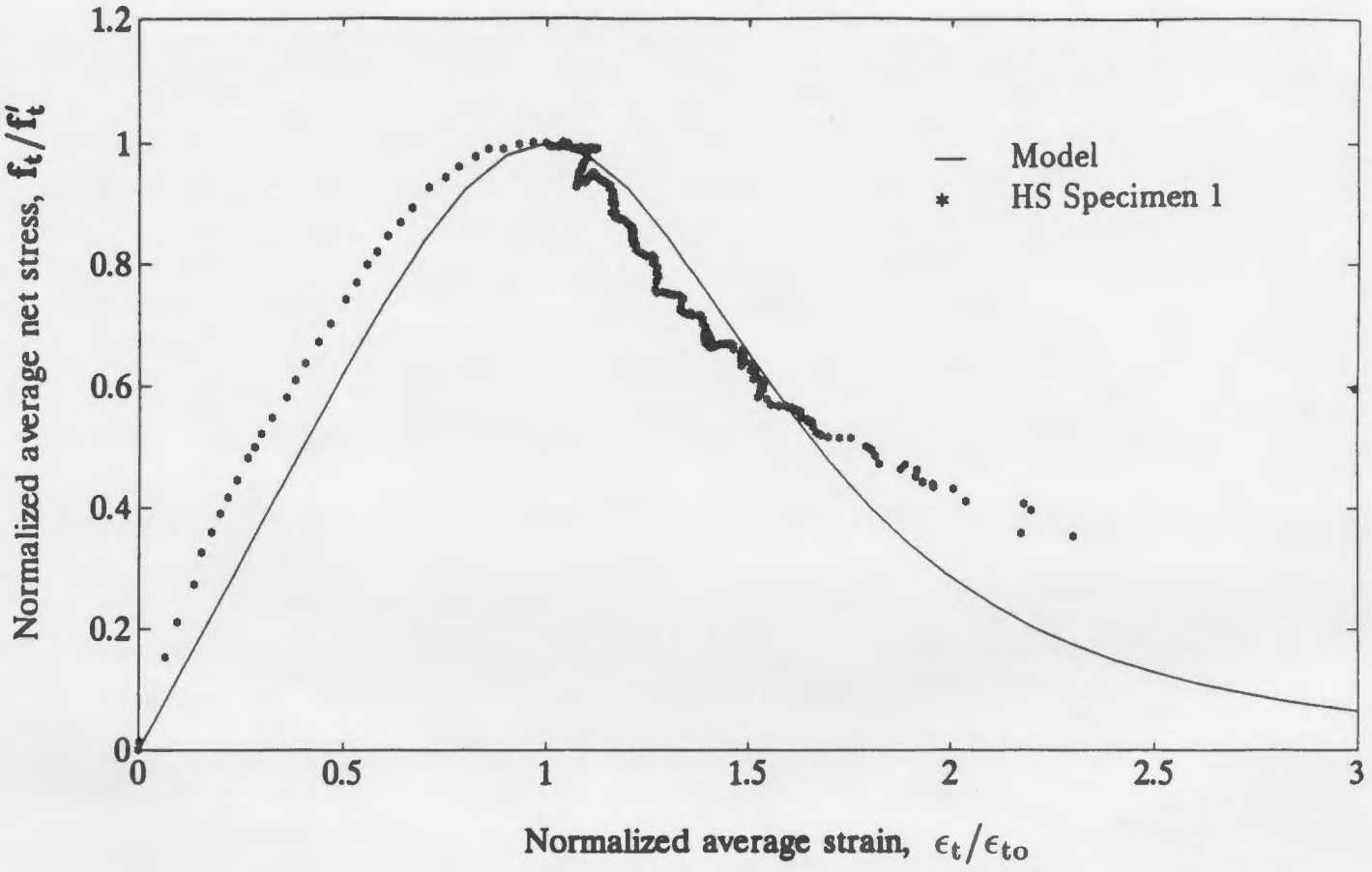

Figure 4.1: Comparison of Carreira and Chu (1986) tension softening model to test measurement obtained for high-strength concrete

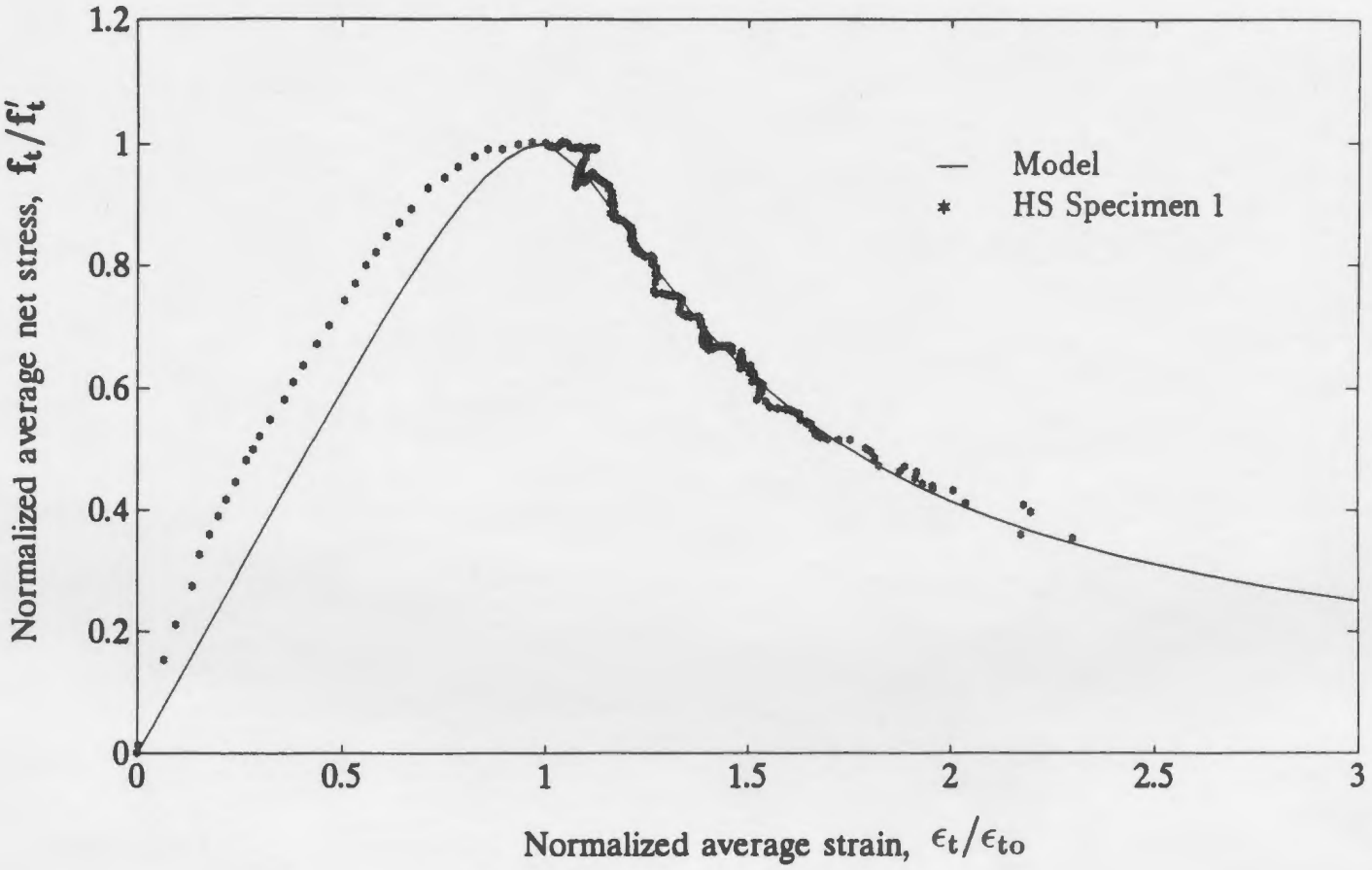

Figure 4.2: Comparison of Guo and Zhang (1987) tension softening model to test measurement obtained for high-strength concrete

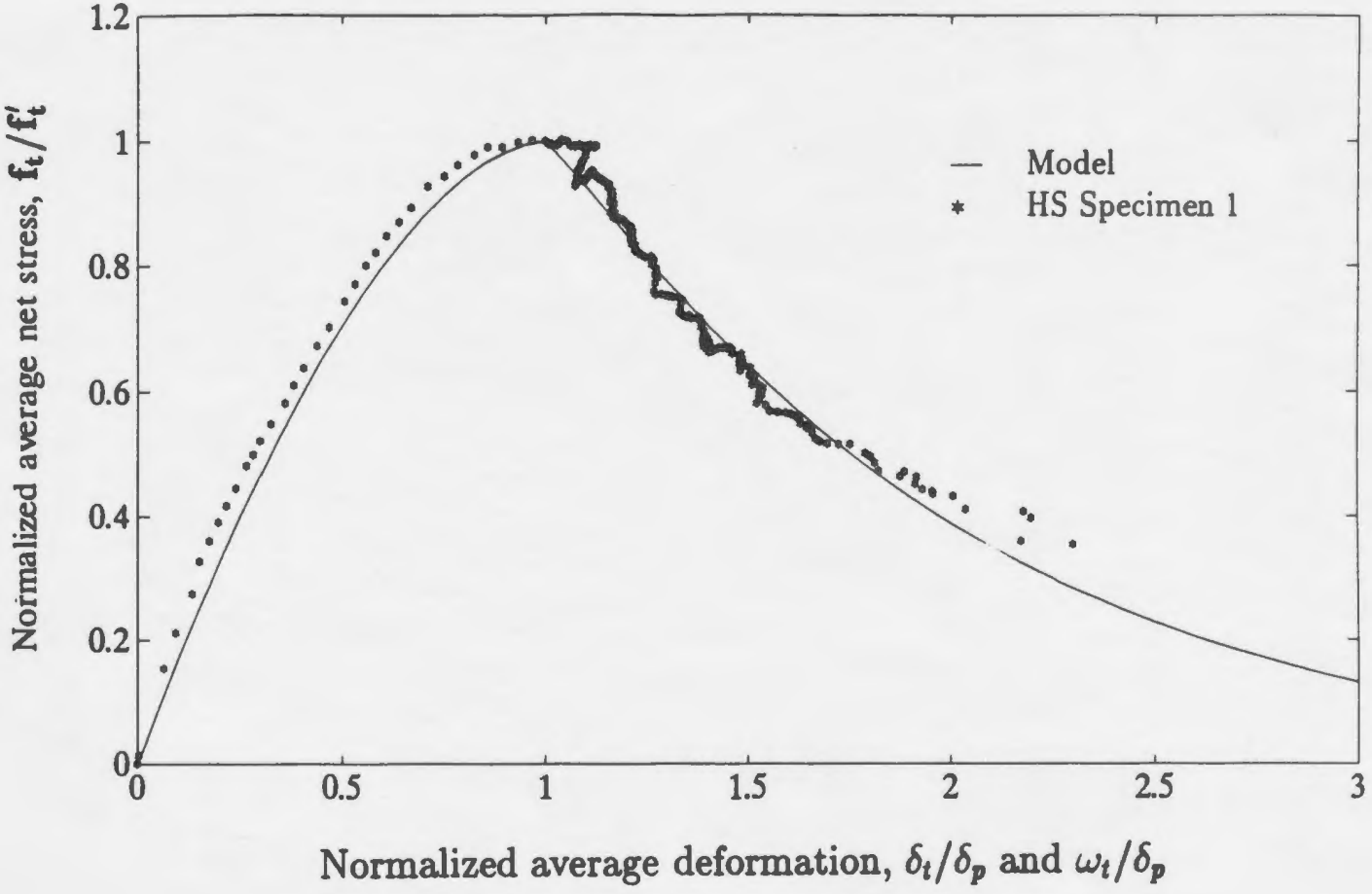

Figure 4.3: Comparison of Gopalaratnam and Shah (1985) tension softening model to test measurement obtained for high-strength concrete

of the plain high-strength concrete specimens tested in uniaxial tension as 1.3863 and 1.6655, respectively, by a nonlinear optimization method. The small value of parameter α indicates the brittle nature of high-strength concrete that rapidly loses its stress-carrying capacity after the peak-stress in tension.

For the ascending portion of the softening model, a simple parabolic expression is proposed for the uniaxial stress-deformation curve up to the peak stress value, based on a regression analysis of the equation to the test data obtained.

Thus, the constitutive relationship of plain high-strength concrete in uniaxial tension can be expressed in two equations as follows:

$$y = 2x - x^2 \qquad x \leq 1.0 \tag{4.7}$$

$$y = \frac{x}{2.8400(x-1)^{1.6655} + x} \qquad x \geq 1.0 \tag{4.8}$$

where,

y = the relative stress f_t/f'_t

x = the relative strain ϵ_t/ϵ_{to}

These two equations are continuous at the peak stress in terms of deformation and slope. The latter satisfies all four boundary conditions: at $x = 1$, $y = 1$; at $x = 1$, $dy/dx = 0$; when $x \to \infty$, $y \to 0$; and when $x \to \infty$, $dy/dx \to 0$. Comparison of the recommended tension softening model to typical experimental observations obtained from plain high-strength concrete specimens tested in direct uniaxial tension is graphically presented in Figs. 4.4 and 4.5. It is evident from these figures that the recommended model follows the test measurements satisfactorily.

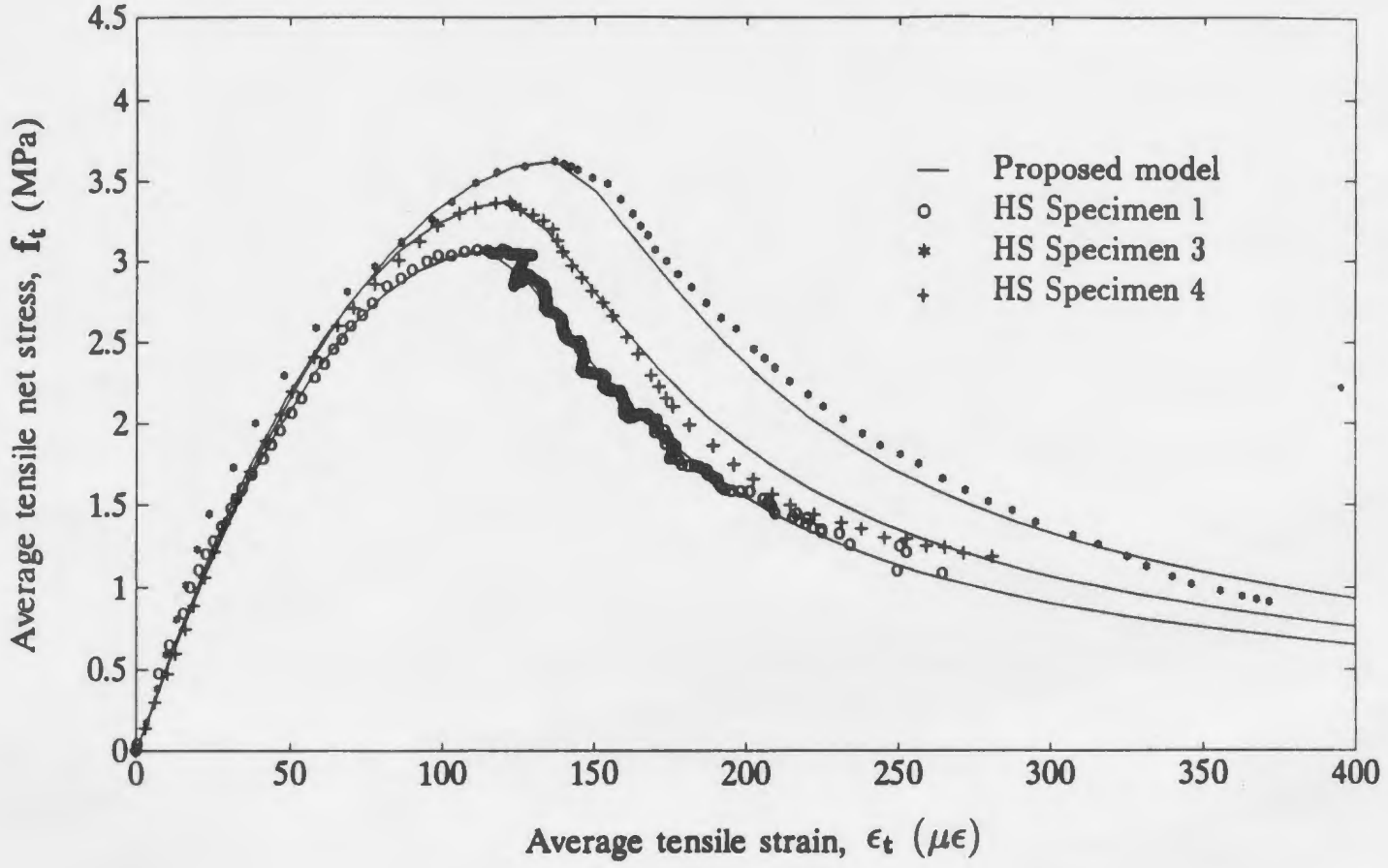

Figure 4.4: Comparison of proposed tension softening model to test measurement obtained for high-strength concrete

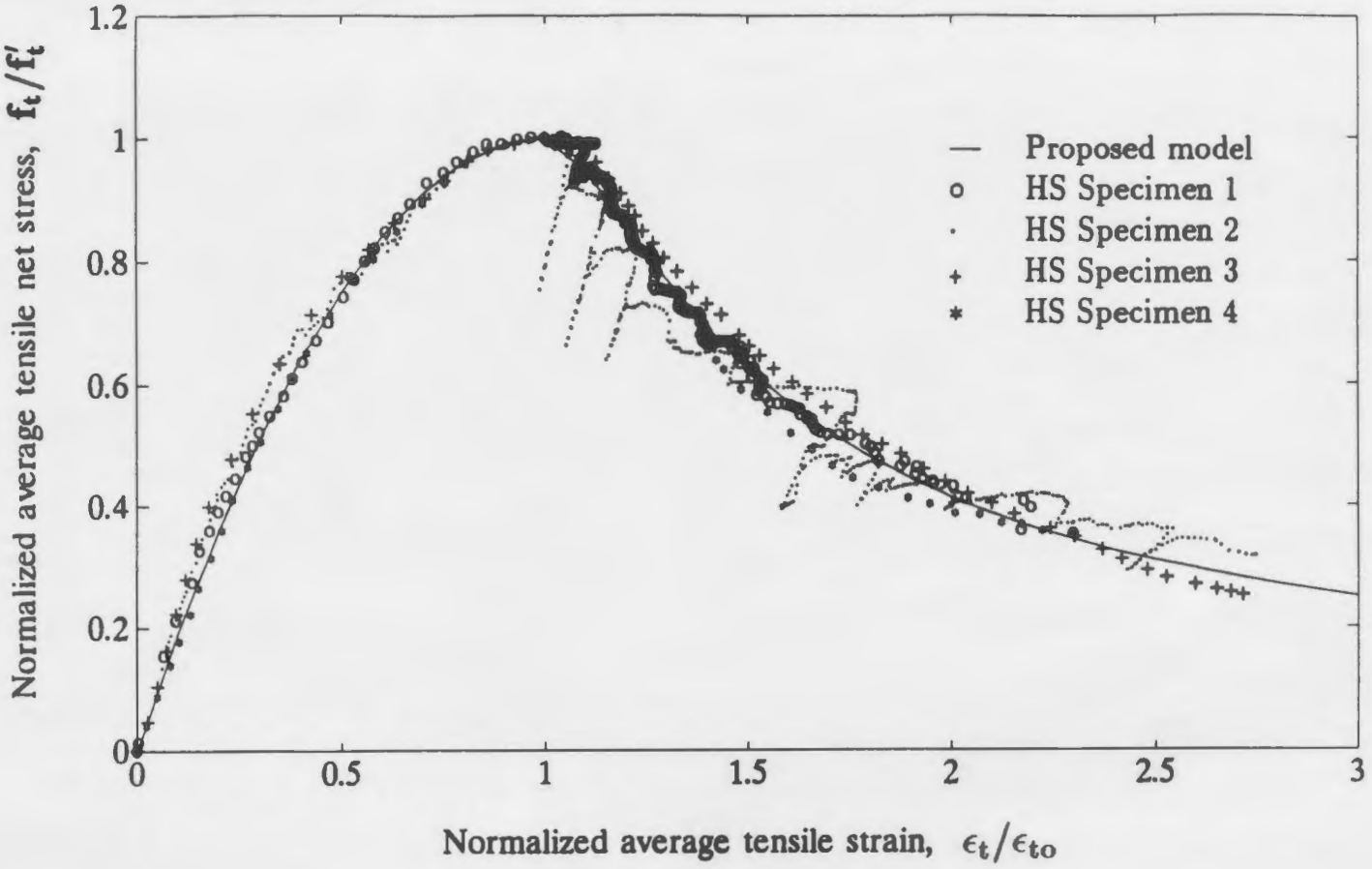

Figure 4.5: Comparison of proposed normalized tension softening model to normalized test measurement obtained for high-strength concrete

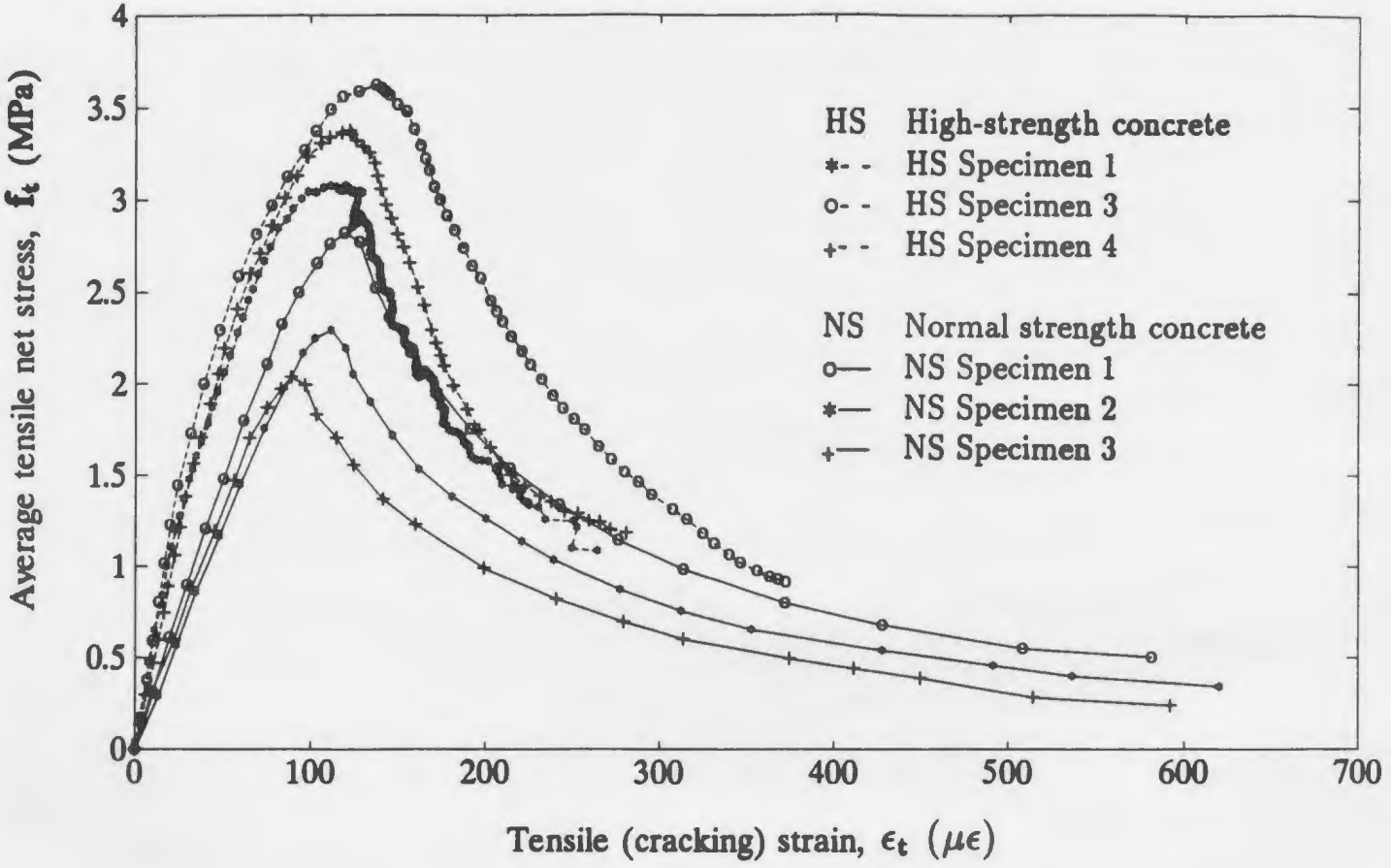

Figure 4.6: Comparison of average net stress-strain measurement of high-strength to normal strength concrete (Guo and Zhang, 1987)

Table 4.1: Comparison of high-strength to normal strength concrete in direct tension

Concrete	f'_c MPa	Direct tension tests: Specimen Dimension mm	Specimen Designation	f'_t MPa	$\epsilon_{to} \times 10^6$ strain	$E_0 \times 10^{-3}$ MPa	f'_t/f'_c
High-strength	74.154*	20 × 75 × 300	HS1	3.067	114.90	47.01	4.1%
			HS3	3.620	136.90	52.97	4.9%
			HS4	3.369	122.00	45.82	4.5%
			Mean value	3.352	124.6	48.6	4.5%
Normal strength	31.410†	100 × 100 × 210 (70 × 70 × 210)	NS1	2.295	111.16	24.10	7.3%
			NS2	2.037	88.93	22.90	6.5%
			NS3	2.819	118.97	30.30	9.0%
			Mean value	2.384	106.35	25.80	7.6%

*From cylinder specimens under compression (152.5 × 305mm)

†From cube specimens under compression (100 × 100 × 100mm), Guo and Zhang (1987)

4.3 Tension softening response of high-strength versus normal strength concrete

This section performs a comparative study on the tension softening response of high-strength and normal strength concrete in an attempt to enhance the understanding of the tension softening nature of high-strength concrete, in which the fracture energy of high-strength concrete is highlighted. Typical test results of high-strength concrete specimens (HS 1, HS 3 and HS 4) obtained in this study are selected as representative results for comparison. The testing of these three specimens resulted in a completely stable failure. For the normal strength concrete, the test results of three specimens reported by Guo and Zhang (1987) are selected in comparison for illustrative purpose.

4.3.1 Stress-deformation curves

The complete stress-deformation curves of high-strength and normal strength concretes in direct tension selected for comparison are presented in Fig. 4.6. The strains, converted from the measured deformation, are equal to the deformation divided by corresponding gage lengths. It can be seen that the high-strength concrete behaved more nonlinearly in the ascending portion of the stress-strain diagram, whereas it descended more sharply after peak stress when compared to normal strength concrete. In addition, the initial axial stiffness of high-strength concrete members appeared higher than that of normal strength concrete. The initial modulus of elasticity is 48.6×10^3 kN/mm^2 for high-strength concrete, almost twice the value of normal strength concrete (Table 4.1), confirming the stiffer and more brittle nature of high-strength concrete.

4.3.2 Tensile strains at the peak stress

It can be seen that the strains at peak stress, ϵ_{to}, increase unanimously as tensile strengths increase (Table 4.1). However, the strains at the peak load for both high-strength and normal strength concrete were relatively close. The relationship between the values of tensile strength and strain at peak developed by Guo and Zhang (1987) is evaluated against test results in this study for high-strength concrete. The regression equation for normal strength concrete overestimates the strain of high-strength concrete at the peak load by 18%.

4.3.3 Tensile strength

It appears that the tensile strength also increases as compressive strength increases. However, the tensile strength increases at a much smaller rate, when it is compared to the increase of the compressive strength. The ratio of the compressive strength between high-strength and normal strength concrete is 2.36, whereas the corresponding ratio for tensile strength is only 1.41. The mean tensile strength is 7.6% of measured compressive strength for normal strength concrete, while the same value decreases to 4.5 % for high-strength concrete, based on the test results of three specimens selected herein for high-strength and normal strength concrete respectively. This indicates that the high-strength concrete is even weaker in tension.

4.3.4 Fracture energy

The post-cracked behaviour was treated with a brittle fracture concept proposed by Hillerborg (1985). The fracture energy required to form an unit area of crack surface, G_f, is assumed to be a material property. This value can be calculated from

integrating the complete tensile stress-crack opening displacement or crack width (ω), as follows:

$$G_f = \int_0^{\omega_o} f_t d\omega \tag{4.9}$$

where the tensile stress f_t is a function of ω and ω_o is the crack width when f_t reaches zero at the end of the concrete tension softening region.

The expression for G_f can be rearranged and expressed as a function of a stress-strain law, more common in the description of engineering materials. Thus, W_f is defined as the fracture energy density (or work per unit of volume) dissipated by cracking, expressed as

$$W_f = \frac{G_f}{w_c} = \int_0^{\epsilon_{max}} f_t \, d\epsilon_t \tag{4.10}$$

where the tensile stress f_t is expressed in terms of tensile strain ϵ_t. ϵ_{max} is the maximum tensile effective (cracking) strain when f_t reaches zero at the end of the tension softening branch. w_c is the width of the fracture process zone. w_c is assumed to remain constant before and after cracking, which is an unknown value at this stage. However, before cracking, the value of w_c can be assumed to be equal to 2 times notch depth plus notch width, that is $w_c = 25\ mm$. This is based on the assumption that the stress trajectories in cracking process zone expand at a 45 degree angle into other regions away from it on either side. This also prompts that an extensometer of 25 mm gage length was used across each notch in order to measure the cracking deformation in the fracture process zone. Hence, w_c was 2.5 times d_{max}, the maximum nominal aggregate size (10 mm). The ratio of w_c to d_{max} fell into the normal range of 1.5 to 4.0 for various types of concrete as stated by Bazant and Oh (1983), based on

their extensive analysis of several test results obtained from various researchers and performed on different types of test set-up.

W_f represents the area under a stress-strain curve of concrete in tension. Hillerborg (1985) pointed out that unlike metallic materials, the energy absorbed by plain concrete members in tension is mainly associated with the descending branch in tension. Concrete damage consists mainly of cracks perpendicular to the principal tensile stress and the tensile stress-displacement curve (f_t-δ_t) is not dependent on stresses in any other directions. Additionally the independence of the tensile stress-displacement curve (f_t-δ_t) with respect to specimen shapes allows one to use G_f for any type of structures.

The maximum tensile effective (cracking) strain (ϵ_{max}) was assumed as 16 times the tensile strain ϵ_{to} at peak stress, since the tensile stress after peak descends sharply and becomes negligible beyond the value of 16 ϵ_{to}, as experimentally observed. Hence, the associated fracture energy density of high-strength concrete, calculated from the above equation (Eq. 4.10), is about 5 times the area under the ascending portion of its complete stress-strain curve. This value is only half of that for normal strength concrete reported by Massicotte et al. (1990), where the maximum tensile effective strain was also assumed as 16 ϵ_{to}. This also indicates that the high-strength concrete is more brittle in tension than normal strength concrete.

4.4 Summary

Several existing prediction equations for modelling the tension softening response of normal strength concrete are evaluated against the test results of high-strength concrete. Based on the test evidence, a constitutive relationship is recommended for

plain high-strength concrete under direct uniaxial tension (Eqs. 4.7 and 4.8).

The unique nature of the tension softening response of high-strength concrete is illustrated in the comparative study performed in this chapter between high-strength and normal strength concrete. The high-strength concrete is more brittle and stiffer, with a larger initial modulus of elasticity, compared to normal strength concrete. After the peak load, the stress-deformation curve of high-strength concrete descends more sharply than that of normal strength concrete. The estimated value of fracture energy density of high-strength concrete is equal to about 5 times the area under the ascending portion of complete stress-strain diagram, while the corresponding value for normal strength concrete increases to 10 times the area under the ascending portion of normal strength concrete stress-strain curve.

In general, the tensile strength, initial modulus of elasticity and the tensile strain at peak stress increase as the compressive strength increases. However, the tensile strength increases at a much smaller rate as the compressive strength increases. Thus, the high-strength concrete is relatively weaker in tension, compared to normal strength concrete. The tensile strength was 7.6% f_c' for normal strength concrete, while this value decreased to 4.5% f_c' for high-strength concrete.

Chapter 5

Finite Element Idealization of Reinforced High-Strength Concrete Slabs

5.1 Introduction

The recommended analytical models of post-cracking behaviour of reinforced high-strength concrete are described. The realistic stress-strain characteristics of high-strength concrete and reinforcing bars obtained in the laboratory are incorporated into a proposed plasticity-based material model, which employs smeared crack concept. The material model allows for a special high-strength concrete strain softening after both cracking and crushing. The finite element model formulated to analyse the structural behaviour of reinforced high-strength concrete slabs is then presented, followed by description of the adopted nonlinear solution techniques, which allows a solution to proceed beyond limit points in a nonlinear analysis.

5.2 Material modelling of concrete

Over the past two decades, several stress-strain relationships have been proposed and used in finite element analysis of reinforced concrete structures. An extensive review of these models was undertaken by the ASCE committee on finite element analysis of reinforced concrete structures (ASCE, 1982). The results from the finite element analysis are largely dependent on these stress-strain relationships, failure criteria used, simulation of steel reinforcement and interaction between the steel and concrete. Proper modelling of cracking and post-cracking behaviour of reinforced concrete, which includes aggregate interlock or shear friction, dowel action and tension stiffening effects, is especially crucial. In order to achieve valid prediction of the response of reinforced concrete structures, all the previously mentioned characteristics of concrete behaviour must be addressed.

The uncertainty present in the behaviour of concrete coupled with the dependence of the results obtained from a nonlinear finite element analysis on several factors that are too complex to be investigated analytically does not justify the use of a highly sophisticated concrete model. However, the concrete model must adequately reproduce the physical characteristics of the concrete response and yield reasonably good results. A good compromise between the acceptable simplicity and accuracy is achieved with plasticity-based models, which can represent inelastic strains in concrete (Suidan and Schnobrich, 1973, Chen and Chen, 1975, Chen and Ting, 1980, etc.). This is a significant improvement over the elasticity-based concrete models (ASCE, 1982).

The experimental results have also confirmed that the nonlinear deformations of concrete are basically inelastic, since upon unloading only a portion of the total strain

can be recovered. Thus, the stress-strain behaviour of concrete materials should be separated into recoverable and irrecoverable components. As a result, the plasticity-based models have been used extensively in recent years to describe the behaviour of concrete (ASCE, 1982).

5.2.1 Plasticity-based concrete model

In this study, the incremental elastic-plastic concrete model implemented in a general purpose finite element analysis code, *ABAQUS*, is adopted. This material model is based on the classical concepts of plasticity theory: a strain rate decomposition into elastic and inelastic strain rates, elasticity, yield, flow, and hardening. This model allows for strain softening after both cracking and crushing. Cracking is assumed to be the most important aspect of the behaviour and representation of cracking and post-cracking behaviour dominates the modelling, as described in the following sections.

5.2.1.1 Concrete in the stress state of dominant compression

When the principal stress components are dominantly compressive, the response of the concrete is modeled by an elastic-plastic theory, using a simple form of yield surface written in terms of the first two stress invariants. Associated flow and isotropic hardening are used, as illustrated in Fig. 5.1. The compression failure surface in plane stress is shown in Fig. 5.2, as originally proposed by Kupfer and Gerstle (1973) based on the experimental evidence of Kupfer et al. (1969).

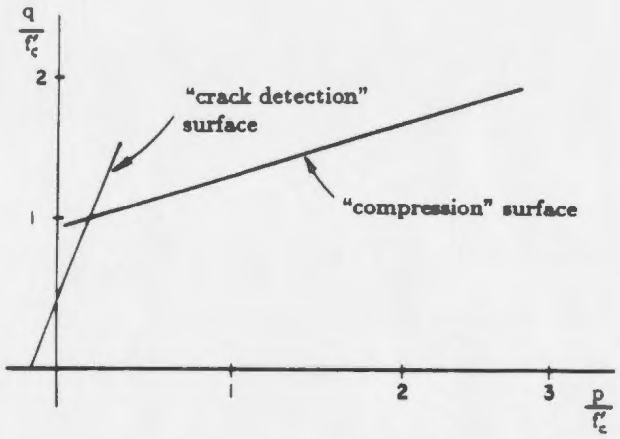

Figure 5.1: Concrete failure surfaces in the $(p - q)$ plane (Hibbitt et al., 1989)

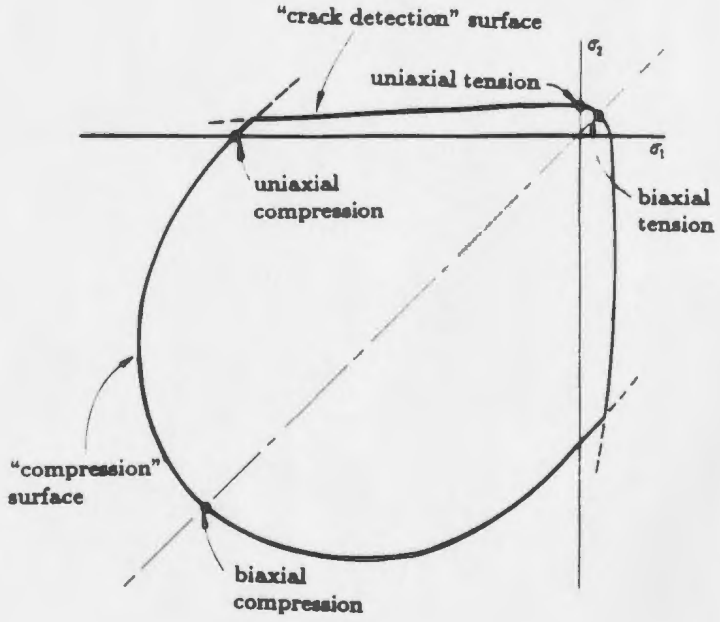

Figure 5.2: Concrete failure surfaces in plane stresses (Kupfer and Gerstle, 1973)

a) Strain rate decomposition

The total strain rate (increment), $d\epsilon$, is assumed to be composed of elastic and plastic components, as follows:

$$d\epsilon = d\epsilon_e + d\epsilon_p \tag{5.1}$$

where $d\epsilon$ is the total strain rate; $d\epsilon_e$ is the elastic strain rate, which includes crack detection strains—this elastic strain will be further decomposed (section 5.2.1.2); $d\epsilon_p$ is the plastic strain rate associated with the compression yield surface.

The elastic part of the strain is assumed to be always small, so that this equation may be integrated as:

$$\epsilon = \epsilon_e + \epsilon_p \tag{5.2}$$

b) Compression yield criterion

The yield criterion for concrete in the dominant compression region is assumed to be dependent on the deviatoric stresses (pure shear stresses) and hydrostatic pressure. The compression yield surface is expressed as:

$$F_c = q - \sqrt{3}a_0 p - \sqrt{3}\tau_c = 0 \tag{5.3}$$

where p is the effective pressure stress (the first invariant of the stress tensor), defined as

$$p = -\frac{1}{3}\mathbf{trace}(\sigma)$$

and q is the Mises equivalent deviatoric stress (the second invariant of the stress tensor):

$$q = \sqrt{\frac{3}{2}\,\mathbf{S} : \mathbf{S}}$$

where $\mathbf{S} = \sigma + p\mathbf{I}$ are the deviatoric stress components; $\mathbf{I}$ is the unity matrix; The constant of a_0 is dependent on the ratio of the ultimate stress reached in biaxial compression to the ultimate stress reached in uniaxial compression; and $\tau_c(\lambda_c)$ is a hardening parameter, which is the size of the yield surface on the q-axis at p=0, so that τ_c is the yield stress in a state of pure shear stress when all other components of the stress tensor σ are zero. The hardening is measured by the value of λ_c, which is defined from the stress-inelastic strain relationship of concrete in uniaxial compression.

This simple yield surface is a straight line in $(p-q)$ space. Thus, only one constant (a_0) is needed to define the shape of the yield surface.

In uniaxial compression, p is equal to $\frac{1}{3}f'_c$ and q is equal to f'_c, where f'_c is the concrete compressive strength. Therefore, on $F_c = 0$ (Eq. 5.3), the τ_c can be expressed as

$$\frac{\tau_c}{f'_c} = (\frac{1}{\sqrt{3}} - \frac{a_0}{3}) \tag{5.4}$$

In biaxial compression, p is equal to $\frac{2}{3}f'_{bc}$ and q is equal to f'_{bc}, where f'_{bc} is the magnitude of the failure principal stress of concrete under equal biaxial stresses.

Therefore, on $F_c = 0$ (Eq. 5.3), the τ_c can be expressed as

$$\frac{\tau_c}{f'_{bc}} = (\frac{1}{\sqrt{3}} - \frac{2a_0}{3}) \tag{5.5}$$

The failure ratio of $r_f = f'_{bc}/f'_c$ can be given as input in the *ABAQUS* (Hibbitt et al., 1989). Typical $r_f \approx 1.16$ was adopted in the analysis. From Eqs. 5.4 and 5.5, a_0 can be calculated as

$$a_0 = \sqrt{3}\frac{1 - r_f}{1 - 2 \cdot r_f} \tag{5.6}$$

c) Hardening rule

The hardening rule defines the motion of the loading surface during plastic deformation. The effective stress τ_c is usually defined as the same function of the stresses that governs yielding (Eq. 5.3). This maps the multiaxial stress state onto equivalent scalar function.

The relation of τ_c to λ_c can be determined from the concrete stress-inelastic strain relationship in uniaxial compression.

As stated earlier, p is equal to $\frac{1}{3}f'_c$ and q is equal to f'_c, in uniaxial compression. During active plastic loading, F_c (Eq. 5.3) is equal to zero. Therefore, τ_c can be obtained as

$$\tau_c = (\frac{1}{\sqrt{3}} - \frac{a_0}{3})f'_c \tag{5.7}$$

d) Flow rule

In plasticity theory a flow rule is defined so that the increments of plastic strain can be evaluated from a given stress state. The present model employs an associated flow rule. This means that the vector of the plastic deformation rate will be assumed to be normal to the adopted yield surface. Thus, the plastic strain rate is defined as

$$d\epsilon_p = \begin{cases} d\lambda_c(1 + c_0(\frac{p}{f_c'})^2)\frac{\partial F_c}{\partial \sigma} & F_c = 0 \text{ and } d\lambda_c > 0 \\ 0 & \text{otherwise} \end{cases} \tag{5.8}$$

Where $d\lambda_c$ is a scalar proportionality factor determining the size of the plastic strain rate; $\frac{\partial F_c}{\partial \sigma}$ is a vector normal to the current loading surface; c_0 is a constant, which is dependent on the other constants in the yield surface and the starin ratio r_ϵ. r_ϵ is defined as the ratio of plastic strain of concrete in a monotonically loaded biaxial compression to that in a monotonically loaded uniaxial compression (Typical value of $r_\epsilon = 1.28$ was used in the analysis). Thus, c_0 can be calculated as follows.

The gradient of the flow potential for the compressive surface is expressed as

$$\frac{\partial F_c}{\partial \sigma} = \frac{\partial q}{\partial \sigma} - \sqrt{3}a_0\frac{\partial p}{\partial \sigma} \tag{5.9}$$

Since

$$\frac{\partial p}{\partial \sigma} = -\frac{1}{3}\mathbf{I}$$

and

$$\frac{\partial q}{\partial \sigma} = \frac{3}{2}\frac{\mathbf{S}}{q}$$

then

$$\frac{\partial F_c}{\partial \sigma} = \frac{3}{2}\frac{\mathbf{S}}{q} + \frac{a_0}{\sqrt{3}}\mathbf{I}$$

In uniaxial compression $p = \frac{1}{3}f'_c$, $q = f'_c$ and $\mathbf{S}_{11} = -\frac{2}{3}f'_c$, so that Eq. 5.8 becomes

$$d\epsilon_p = d\lambda_c(1 + \frac{c_0}{9})(\frac{a_0}{\sqrt{3}} - 1) \tag{5.10}$$

Upon integration, the plastic strain is given by

$$\epsilon_p = \lambda_c(1 + \frac{c_0}{9})(\frac{a_0}{\sqrt{3}} - 1) \tag{5.11}$$

so that λ_c can be evaluated from the plastic strain ϵ_p and the constants a_0 and c_0. Therefore, Eqs. 5.7 and 5.11 define the $\tau_c(\lambda_c)$ relationship from the concrete stress-inelastic strain relationship in uniaxial compression.

In biaxial compression, when both non-zero principal stresses have the magnitude f'_{bc}, $p = \frac{2}{3}f'_{bc} = \frac{2}{3}r_f f'_c$, $q = f'_{bc} = r_f f'_c$, and $\mathbf{S}_{11} = -\frac{1}{3}r_f f'_c$. Therefore, the flow rule becomes

$$d\epsilon_{pb} = d\lambda_c(1 + \frac{4}{9}r_f^2 c_0)(\frac{a_0}{\sqrt{3}} - \frac{1}{2})$$

Where $d\epsilon_{pb}$ is the principal plastic strain rate associated with f'_{bc}. Using the above equation and Eq. 5.10 then defines c_0 from $r_\epsilon = \epsilon_{pb}/\epsilon_p$ and the other constants as

$$c_0 = 9\frac{r_\epsilon(\sqrt{3} - a_0) + (a_0 - \sqrt{3}/2)}{r_\epsilon(\sqrt{3} - a_0) + r_f^2(2\sqrt{3} - 4a_0)} \tag{5.12}$$

The compression surface is illustrated in Figs. 5.1 and 5.2.

5.2.1.2 Concrete in the stress state of dominant tension

Tensile failure in matrix-aggregate composites like concrete involves progressive micro-cracking, tortuous debonding and other process of internal damage. These softening processes eventually coalesce into a geometric discontinuity that separates the material. Such a discontinuity is called a crack.

Cracking dominates the material behaviour when the state of stress is predominantly tensile. The "crack detection" plasticity surface in stress space is used in the concrete model to determine when cracking takes place., and the orientation of the cracking. Damaged elasticity is then employed to describe the post-cracking behaviour of the concrete with the open cracks. This crack detection surface is taken to be a simple Coulomb line written in terms of first and second stress invariants, p and q, shown in Fig. 5.1. In a plane stress situation, the failure surfaces is shown in Fig. 5.2.

In the biaxial tension region, some researchers (Tasuji et al., 1978) have noticed a slight increase in the tensile strength when the two principal tensile stresses are equal whereas other researchers (Kupfer et al., 1969) have observed the opposite. In both cases the differences of concrete tensile failure strength with f_t' is not significant enough to necessitate a more accurate failure envelope. Therefore, it is usually assumed that the concrete cracks at f_t' for any stress ratio.

In the case of tension-compression stress state, a parabola cracking envelope developed by other researchers (Kupfer and Gerstle, 1973) is adopted, as illustrated in Fig. 5.2.

a) Elastic strain rate decomposition

The total elastic strain rate (increment) in Eq. 5.1 can be further decomposed as:

$$d\epsilon_e = d\epsilon_{et} + d\epsilon_{pt} \tag{5.13}$$

where $d\epsilon_e$ is the total elastic strain rate; $d\epsilon_{et}$ is the elastic strain rate for the crack detection and $d\epsilon_{pt}$ is the plastic strain rate associated with the crack detection surface.

b) Tension yield criterion

The crack detection surface is taken as the Coulomb line:

$$F_t = \hat{q} - (3 - b_0 \frac{f_t}{f_t'})\hat{p} - (2 - \frac{b_0}{3}\frac{f_t}{f_t'})f_t = 0 \tag{5.14}$$

where f_t' is the tensile failure stress in uniaxial tension, and b_0 is a constant to be defined. f_t, as a hardening parameter, is the equivalent tensile stress. The hardening is measured by λ_t. The relationship of f_t with λ_t is defined in the ***hardening rule***. The stress measures $\hat{p}$ and $\hat{q}$ are defined in the same way as p and q, except all stress components associated with open cracks are not included in these measures: they are invariants in sub-spaces of the stress space.

As can be seen, the concrete hardening is introduced in the particular form (Eq. 5.14). Thus, as $f_t \to 0$, the yield surface (Eq. 5.14) becomes $q - 3p = 0$, which is the cone containing the principal axes of stress in $(p - q)$ space. This indicates that the stress point will drop back onto the nearest principal stress axis as the tension stiffening is exhausted in the state of plane stress.

In the state of plane stress, cracking could be assumed to occur when one principal stress has the value $\sigma_1 = -f_c'$ and the other non-zero principal stress has the value $\sigma_2 = rf_t'$ (r is a scalar factor). Let r_{tc} represents the ratio of the concrete stress reached in uniaxial tension to that in uniaxial compression ($r_{tc} = f_t'/f_c'$), cracking would therefore occur at the point with principal stresses $-f_c'$, $rr_{tc}f_c'$, and 0. Thus,

$$p = \frac{1}{3}(1 - r \cdot r_{tc})f_c'$$

and

$$q = f_c'\sqrt{1 + (r \cdot r_{tc})^2 + r \cdot r_{tc}}$$

Thus, when $f_t = f_t'$, the crack detection surface becomes

$$F_t = f_c'\sqrt{1 + (r \cdot r_{tc})^2 + r \cdot r_{tc}} - \frac{1}{3}(3 - b_0)(1 - r \cdot r_{tc})f_c' - (2 - \frac{b_0}{3})r_{tc}f_c' = 0$$

Therefore, the constant b_0 is obtained as

$$b_0 = 3\frac{1 + (2 - r)r_{tc} - \sqrt{1 + (r \cdot r_{tc})^2 + r \cdot r_{tc}}}{1 + r_{tc}(1 - r)} \tag{5.15}$$

The crack detection surface is illustrated in Figs. 5.1 and 5.2.

c) Flow rule

The assumption of the associated flow rule is also adopted in this crack detection model:

$$d\epsilon_{pt} = \begin{cases} d\lambda_t \dfrac{\partial F_t}{\partial \sigma} & F_t = 0 \text{ and } d\lambda_t > 0 \\ 0 & \text{otherwise} \end{cases} \tag{5.16}$$

Where $d\lambda_t$ is a scalar proportionality factor determining the size of the plastic strain rate associated with crack detection surface, and $\frac{\partial F_t}{\partial \sigma}$ is a vector normal to the current loading surface.

d) Hardening rule

The hardening is measured by the value of λ_t. $f_t(\lambda_t)$ relationship can be defined from the stress-inelastic strain relationship of concrete in uniaxial tension as follows.

By using the tension yield criterion (Eq. 5.14), the flow rule (Eq. 5.16) becomes

$$d\epsilon_{pt} = d\lambda_t \left(\frac{2}{3}\frac{\mathbf{S}}{q} + \left(1 - \frac{b_0}{3}\frac{f_t}{f_t'} \right) \mathbf{I} \right)$$

In uniaxial tension, $\mathbf{S}_{11} = \frac{2}{3} f_t$, and $q = f_t$. Therefore, in uniaxial tension, the hardening rule can be rewritten as

$$d\epsilon_{pt} = d\lambda_t (2 - \frac{b_0}{3}\frac{f_t}{f_t'})$$

Therefore

$$d\lambda_t = d\epsilon_{pt} / (2 - \frac{b_0}{3}\frac{f_t}{f_t'}) \tag{5.17}$$

Upon integration, the above equation gives $d\lambda_t$ from $d\epsilon_{pt}$. Thus, $f_t(\lambda_t)$ relationship can be obtained from the stress-inelastic strain relationship of concrete in uniaxial tension.

5.2.2 Smeared crack approach

Cracking of concrete is one of the important sources of material nonlinearity of reinforced concrete members. Although crack initiation can be introduced easily in the computer model, it is difficult to account for continued propagation of cracks with increase in loading, since it would require continued redefinition of the topology of the model, which complicates the analytical idealization.

The smeared cracking model is used in the present analysis. The smeared cracking model is based on the concept of stress discontinuity while maintaining displacement continuity. This means that individual "macro" cracks are not tracked, rather, constitutive calculations are performed independently at each integration point of the finite element model, and the presence of cracks enters into these calculations by the way in which the cracks affect the stress and material stiffness associated with the integration point. The crack orientation is included to represent the material anisotropy introduced by cracking in the direction of the maximum tensile principal plastic strain increment conjugate to the crack detection surface and orthogonal to the directions of any existing cracks at the same point. Cracking is irrecoverable and remains throughout the rest of the calculation.

5.3 Post-cracking behaviour

Once concrete has cracked, three phenomena are normally manifested, namely, aggregate interlock, dowel action, and tension stiffening. For satisfactory modeling of post-cracking behaviour, these must be incorporated into the nonlinear analysis.

Aggregate interlock or "shear friction" accounts for the transfer of shear force across a crack, when shear displacements parallel to the direction of the cracks occur.

As the crack width increases, the contact area of the concrete on the two sides of the crack decreases and, thus, the shear forces transferred by the aggregate interlock or the shear friction mechanism decrease. In the reinforced concrete structures, reinforcement crossing the cracks tends to prevent the cracked pieces from moving apart and provides significant clamping forces which enhance aggregate interlock mechanism. Moreover, any movement of cracked pieces of concrete parallel to the crack causes the reinforcement crossing the crack to transfer shear forces by dowel action. On the other hand, due to the bond effect, concrete is still capable of carrying tensile stress after the formation of primary cracks. As the load increases, more secondary cracks appear and tensile stresses in the concrete are released gradually.

In the present material model, the open cracks are represented by loss of elastic stiffness. Concrete is assumed to lose strength through a softening mechanism. The concept of damaged elasticity is then used to model the existing cracks.

5.3.1 Fracture energy

The basis of the concrete post-cracking behaviour is based on the brittle fracture concept of Hillerborg (1985). The fracture energy required to form a unit area of crack surface, G_f, is assumed to be a material property. This value can be calculated from measuring the tensile stress (f_t) as a function of the crack opening displacement or crack width (ω), as

$$G_f = \int_0^{\omega_o} f_t d\omega \tag{5.18}$$

where ω_o is the crack width when f_t reaches zero at the end of the concrete tension softening region. Thus, the concrete post-cracking behaviour can be characterized by

a tensile stress displacement relationship, as shown in Fig. 5.3. Since all the calculations in the smeared crack approach are performed independently at each integration point, the characteristic length associated with the integration point is used to compute the average crack opening strain. This characteristic length is taken as the cubic root of the concrete volume associated with an integration point in the finite element program.

5.3.2 Damaged elasticity

Following crack detection, the concept of the damaged elasticity is employed to model the concrete with open cracks. It is assumed that only the material properties associated with the direction normal to the crack are affected and the tangent modulus of elasticity in this direction is set to zero for the material stiffness matrix but the stress normal to the crack is released gradually, as governed by the concrete *tension stiffening* mechanism. However, the tangent modulus of elasticity in the direction parallel to the crack is assumed to be unaffected by the crack. Thus, the cracked concrete is modelled as an orthotropic material. Poisson's ratio is also set to zero after cracking.

The shear modulus of elasticity associated with the existing crack direction is also assumed to be damaged. The degradation of shear modulus is assumed as a function of the cracking strain across the crack.

Therefore, in the state of plane stress the orthotropic constitutive matrix of concrete is defined as:

$$\begin{Bmatrix} df_t \\ df_n \\ df_{tn} \end{Bmatrix} = \begin{bmatrix} E_{ts} & 0 & 0 \\ 0 & E_c & 0 \\ 0 & 0 & \varrho G_o \end{bmatrix} \begin{Bmatrix} d\epsilon_t \\ d\epsilon_n \\ d\bar{\epsilon}_t \end{Bmatrix} \tag{5.19}$$

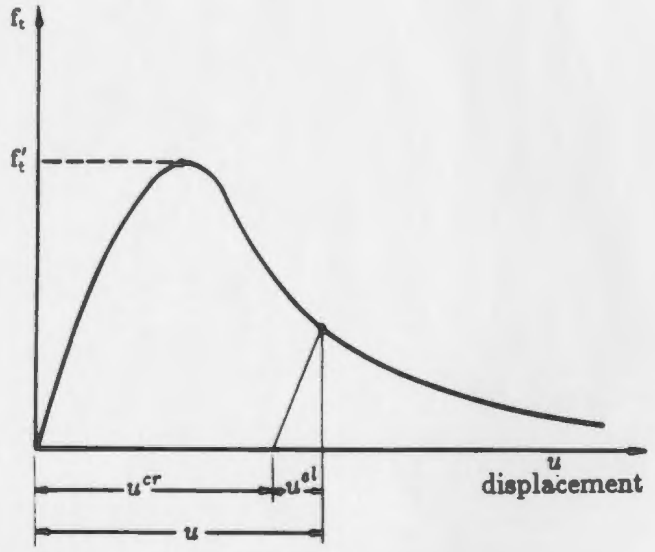

Figure 5.3: Cracking behaviour based on fracture energy (Hillerborg et al., 1976)

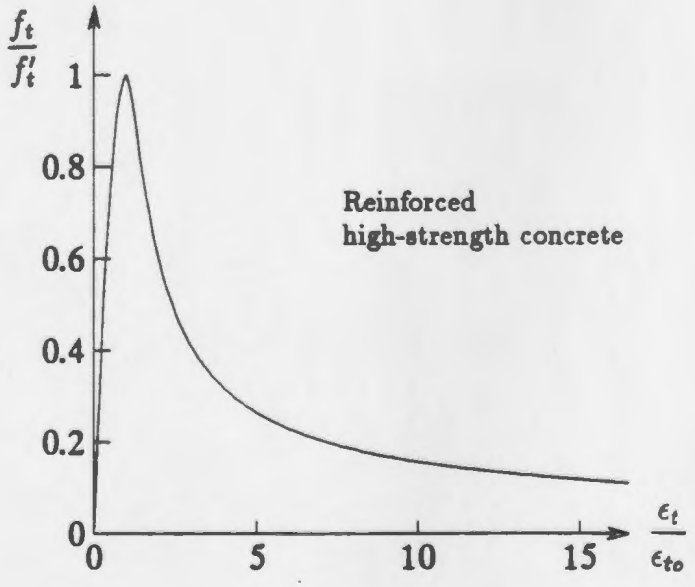

Figure 5.4: Idealization of tension stiffening model for reinforced high-strength concrete

Where, the E_{ts} is the tangent modulus of elasticity associated with the direction normal to the crack, which is defined from the tension stiffening behaviour of concrete; E_c is the tangent modulus of elasticity in the direction parallel to the crack, which is assumed to remain unchanged with open cracks; df_n and $d\epsilon_n$ are the direct stress and strain rates in the direction parallel to the crack; and df_{tn} is the shear stress associated with the cracked plane.

The developed tension stiffening model and shear degradation function are presented in the following two sections, along with the definitions of the other terms employed in the above equation.

5.3.3 Tension stiffening model

In the present study, the tension stiffening effect is modelled by using the descending branch of the tensile stress-strain curve of concrete. The idealization of the tension characteristics of reinforced high-strength concrete, including post-cracking tension stiffening behaviour, based on the direct tension tests of plain high-strength concrete specimens, is proposed as follows,

$$f_t = \begin{cases} f_t'(2x - x^2) & x < 1 \\ \dfrac{f_t' x}{1.3863(x-1)^{1.6655} + x} & x \geq 1 \end{cases} \tag{5.20}$$

$$x = \frac{\epsilon_t}{\epsilon_{to}} \tag{5.21}$$

where ϵ_t is the concrete tensile strain and ϵ_{to} is the concrete tensile strain at f_t'. The concrete uniaxial tensile strength (f_t') is about 5.0% of f_c' as measured from

high-strength concrete specimens tested under uniaxial direct tension. The proposed idealization of the tension-stiffening model for reinforced high-strength concrete is shown in Fig. 5.4.

5.3.4 Shear degradation model

For the simplicity, a linear degradation function is proposed to account for the gradual loss of the concrete shear modulus of the cracked plane with respect to the average crack opening strain across the crack, as follows:

$$G = \varrho G_0 \tag{5.22}$$

$$\varrho = \begin{cases} (1 - \dfrac{\bar{\epsilon}_t}{\epsilon_{sr}}) & \bar{\epsilon}_t < \epsilon_{sr} \\ 0 & \bar{\epsilon}_t \geq \epsilon_{sr} \end{cases} \tag{5.23}$$

$$\epsilon_{sr} = \epsilon_{sr}^u - \epsilon_{to} \tag{5.24}$$

$$\bar{\epsilon}_t = \epsilon_t - \epsilon_{to} \tag{5.25}$$

Where G_0 is the initial shear modulus of concrete in its uncracked state. ϱ is the linear degradation function of shear modulus. $\bar{\epsilon}_t$ is average crack opening strain across the crack. ϵ_{sr} and ϵ_{sr}^u are the total average shear-effective crack opening strain and ultimate shear-effective tensile strain at which concrete shear stiffness is reduced to zero. ϵ_{sr} is proposed to be equal to 0.0012 (about ten times the tensile failure strain) based on our parametric study. The concrete shear stiffness is also assumed damaged for the cracks that subsequently close

$$\varrho = \varrho^{close} \quad \text{for } \bar{\epsilon}_t < 0 \tag{5.26}$$

where ϱ^{close} is the reduction factor of shear modulus related to the cracks that subsequently close during the calculation, which was assumed equal to 0.8 for the high-strength concrete slabs. The simplified idealization of shear degradation model for reinforced high-strength concrete is shown in Fig. 5.5.

5.4 Material properties

The predictions of finite element analysis are strongly dependent on the assumed stress-strain characteristics of the concrete, when the load capacity of concrete structure is not governed by simple yielding of the reinforcement. Realistic mechanical properties of high-strength concrete are significant for any sophisticated finite element material model.

In this study, the experimentally measured complete tensile stress-displacement behaviour of high-strength concrete including tension softening response was incorporated into the material model, as previously described. The model used the uniaxial tensile strength f_t' of $5.0\% f_c'$ and the corresponding tensile strain of 120 $\mu\epsilon$, as recorded from the plain high-strength concrete tested under direct uniaxial tension (refer to chapters 3 and 4).

The complete uniaxial compressive stress-strain relation recorded with the secant modulus of elasticity of 35 MPa at 0.4 f_c', including a concrete compression softening region (Marzouk and Hussein, 1990) was also employed in the material model. Individual values of concrete compressive strength, which were individually measured

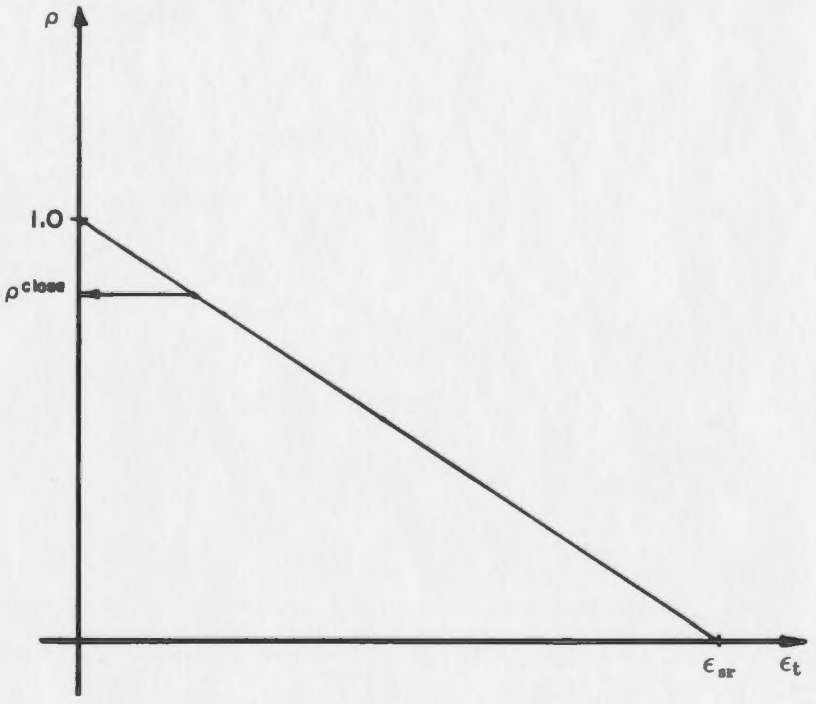

Figure 5.5: Simplified idealization of shear degradation model for reinforced high-strength concrete

from three standard concrete cylinders associated with each slab, were used for different slabs. The recorded average concrete strain corresponding to f_c' were around 0.003 for different slabs studied with ultimate strains measured around 0.0034. The experimentally determined stress-strain relation of high-strength concrete under uniaxial compression is shown in Fig. 5.6. Poisson's ratio of 0.24, reported for high-strength concrete by Chen (1982), was adopted in the material model throughout this study.

Two recorded stress-strain relations measured in our laboratory individually for 10 mm and 15 mm diameter deformed bars (CSA-G30.12 grade 400) were also incorporated into this material model, as shown in Fig. 5.7.

For the normal strength concrete, the uniaxial compressive stress-strain relation recommended by Chen (1982) was selected with Poisson's ratio equal to 0.2. The uniaxial concrete tensile strength f_t' equal to 8.36% f_t' was adopted, as used by Gilbert and Warner (1978).

5.5 Finite element modelling of one quarter slab

5.5.1 Shear-flexible shell element for plain concrete

The material model described earlier is implemented in a general purpose finite element analysis code, ABAQUS (1989), in the context of shear flexible shell element. Many material models are well described directly in this code and a general interface for user specification of material behaviour is also available. This capability has been extensively used in researches on advanced material behaviour. This code also provides various types of elements for one-, two- and three-dimensional problems, such as the truss, plane stress and plane strain, 3-D solid elements, straight or curved beam of any arbitrary cross-section, pipes, springs, interface element, dash-pots, shells and

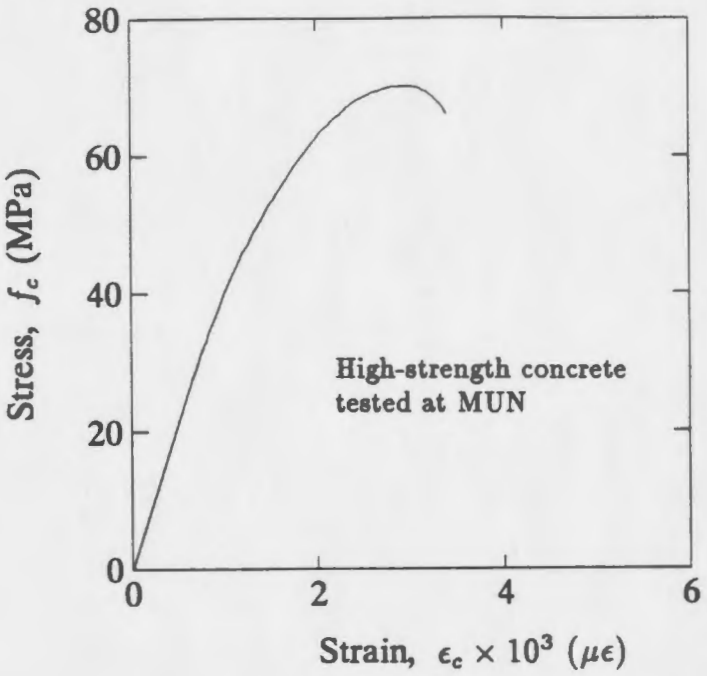

Figure 5.6: Recorded uniaxial compressive stress-strain relation of high-strength concrete (Marzouk and Hussein, 1990)

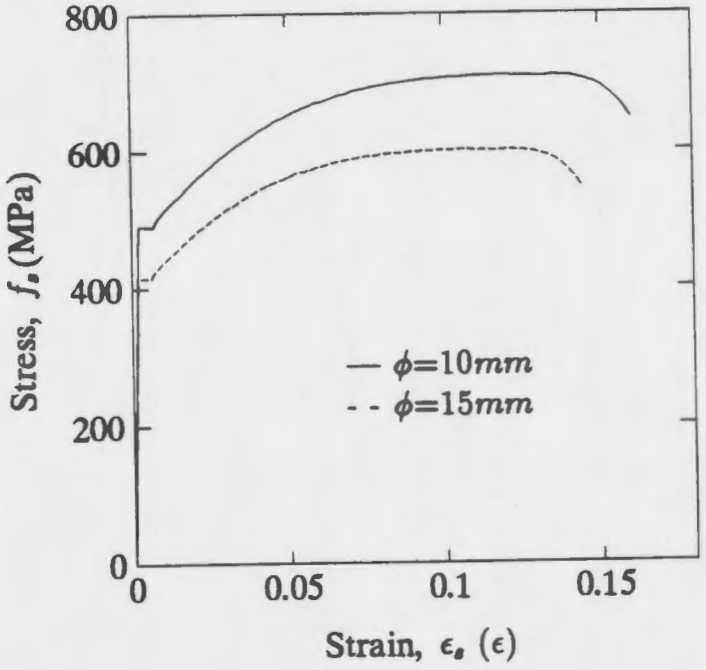

Figure 5.7: Recorded stress-strain relation of deformed steel bars (Marzouk and Hussein, 1990)

user defined elements.

In the shell element library, the general, curved geometries, as well as axisymmetric shells are provided, which contain both "thin" shells—shell elements in which the Kirchhoff constrains are imposed algebraically, and "shear flexible" shells—shell elements in which transverse shear deformation is allowed. The essential idea of shear flexible shells is that the displacement of a point in the shell reference surface and the components of a vector **n** which is approximately normal to the reference surface are interpolated independently. This allows for nonlocking shear and membrane deformation. The performance of these shell elements are further improved by the concept of selectively reduced integration. Thus, the application of such shear flexible shell elements has been extended into the range of thick shell problems.

The cross-section of the shells can be formed by numerical integration, thus, providing complete generality in material modeling. With this option, any number of material points can be defined through the thickness, and material response can be varied from the point to point through the thickness. Moreover, layered shells can be used to model layers of different material, in different orientations, used in the same cross-section.

In this study, 8-node quadrilateral shear flexible shell element with all six degrees of freedom per node taken into consideration is selected to perform the analysis as shown in Fig. 5.8. The displacements of any point through the thickness of the element is defined as a function of the reference surface (midplane) displacements. A reduced 2×2 Gaussian integration rule over the element plane is adopted, whereas a nine-point Simpson-type integration is performed through the thickness. One quarter of the slabs is modelled with 3×3 finite element mesh, as illustrated in Fig. 5.8. The

details of the analyzed slabs are presented in chapter 6.

5.5.2 Representation of steel reinforcement

Reinforcement is treated as one-dimensional strain element, that can be defined singly or embedded in any oriented surfaces in the selected finite element program. The standard metal plasticity approach is used to describe the behaviour of the rebar material. The rebar is then superposed on a mesh of standard element types used to model the plain concrete. This modelling approach allows the concrete behaviour to be considered independent of the rebar. Effects associated with the rebar/concrete interface, such as bond slip, dowel action and tension stiffening, may be modeled, as described earlier.

In this study, the reinforcing steel was simply represented by four layers of uniform thickness located at a constant relative depth inside element, each having independent but unidirectional property. The steel stress-strain relationship (Fig. 5.6) measured from tests at MUN (Marzouk and Hussein, 1990) was implemented in the analysis, which included elastic, yield, plastic and hardening. The uniformly layered representation of reinforcing steel is illustrated in Fig. 5.8.

5.5.3 Spring element for slab edge support

In modelling the slabs simply supported on four edges being free to lift during the tests, the proper simulation of the boundary condition becomes very important in order to obtain the satisfactory prediction of the slab response. Thus, special nonlinear spring elements in the transverse direction are employed along four edges of slabs in the numerical model, as illustrated in Fig. 5.8. The stiffness of spring elements was numerically set to be infinity and zero when in compression and in tension respec-

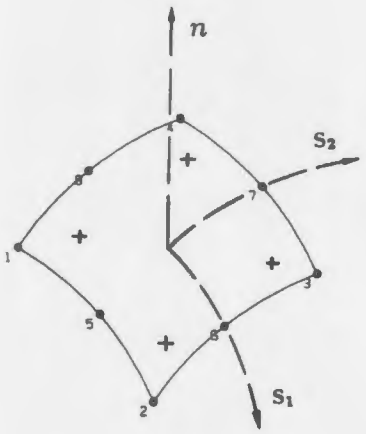

(a) 8-Node quadrilateral shear flexible shell element with the reduced 2 x 2 Gaussian integration over the plane and nine-point Simpson integration through the thickness

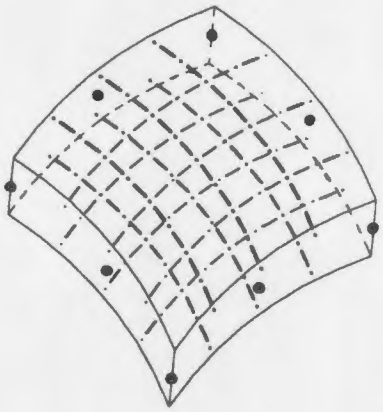

b) Reinforcement idealized as four uniform thickness layers embeded in shell element

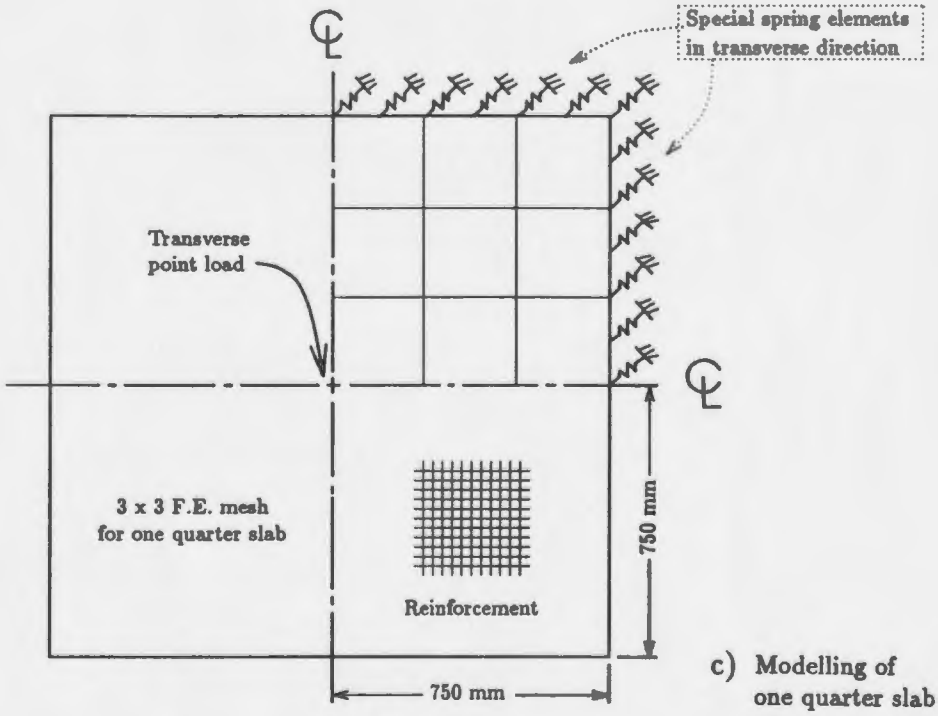

c) Modelling of one quarter slab

Figure 5.8: Finite element model used in the analysis

tively. The effect of different boundary conditions on the slab behaviour is illustrated in the parametric study in the chapter 7.

5.6 Solution strategies

5.6.1 Incremental-iterative method

The computation was performed by incremental loading, with iterations in each increment. The implicit, stiffness method was used. The material calculations used to define the behaviour of the concrete were carried out independently at each integration point in that part of the model made of concrete. The solution was known at the start of the load increment, and the constitutive calculations provide the values of stress and material stiffness at the end of the increment, based on the current estimate of the kinematic solution for the response at the spatial integration point during the increment. The automatic loading incrementation scheme was selected to perform the nonlinear analysis of high-strength concrete slabs throughout this study, as detailed in the following section. Therefore, the nonlinear solution can be more easily achieved with confidence.

5.6.2 Automatic load incrementation

In the nonlinear analysis, the automatic incrementation is commonly used due to the unknown nature of the response, which is based on the convergence rate of the early iteration process at each load increment. The automatic incrementation assumes that convergence will occur relatively smoothly as the iterations progress, so that the number of iterations needed to achieve convergence to the specified tolerances can be reasonably predicted from the rate at which the residuals are reduced from one

iteration to the next during the early iterations.

However, the convergence within an increment is often erratic when the adopted material model involves oriented failure due to concrete cracking, crushing and rebar yielding. Therefore, the automatic subdivision algorithm tends to lead to unreasonably small increments. In order to avoid this problem in this study, the maximum number of iterations allowed per increment was increased to 15 and the automatic incrementation was used only if the convergence was not achieved in the maximum number of iterations allowed. Also, the equilibrium tolerance of 0.2% estimate of maximum load-carrying capacity is chosen in this study in order to achieve accurate prediction. With all these parameters accounted for, the model predictions were obtained in a relatively efficient manner.

5.6.3 Modified Riks algorithm

The modified *Riks* algorithm was selected to effectively obtain the static equilibrium solution for unstable response encountered in concrete, due to concrete cracking in tension, reinforcement yielding, or falling branch of concrete in compression. With this algorithm, the ultimate collapse can be genuinely defined, thus, to reveal collapse mode and to throw light on the ductility or deformation capacity of the structure. This is difficult to achieve with a load control solution strategy. The Riks algorithm is based on attempting to step along the equilibrium path (the load-displacement response curve) by prescribing the path (arch) length along the curve to be traversed in each increment, with the load magnitude included as unknown.

A proportional loading history is normally assumed with this approach; however, any additional constant load vectors can be carried over from previous execution

of the program to the present analysis. With this option, certain non-proportional loading problems can be handled in this program as illustrated in the parametric study (refer to chapter 7).

Chapter 6

Validation of the Finite Element Model

6.1 Introduction

An extensive experimental investigation on the structural behaviour of reinforced high-strength concrete slabs were conducted at Memorial University of Newfoundland (MUN). The test results are presented with new classification, followed by verification of the finite element numerical model formulated in the preceding chapter. The material model implemented in the selected finite element program, recommended in conjunction with appropriate representation of post-cracking behaviour of reinforced high-strength concrete and realistic material properties, is examined against experimental results of slabs tested at MUN with different compressive strengths, slab geometries, reinforcement ratios and yielding stresses.

6.2 Previous experimental work on the behaviour of high-strength concrete slabs

A research program at the Memorial University of Newfoundland is being carried out to study the behaviour of slabs made of reinforced high-strength concrete with silica fume and fly ash. Both experimental and numerical approaches are used. In the previous experimental investigation, tests on fourteen high-strength concrete slabs and two normal strength concrete slabs were conducted. The tested slabs were simply supported along the four edges free to lift under lateral load at the slab center. The load deflection characteristics and failure modes were studied, as reported in detail by Marzouk and Hussein (1991).

In the experimental investigation, the effects of reinforcement ratios, width-thickness ratios, various concrete strength and reinforcement yield strength on the behaviour of high-strength concrete slabs were studied. The reinforcement ratios varied from 0.49% to 2.37%, with the width-to-thickness ratios ranging between 10 to 17. The concrete compressive strength was 66-80 MPa for high-strength concrete and 30-42 MPa for normal strength concrete. Top and bottom reinforcement were provided. The reinforcement consisted of hot-rolled 10 mm and 15 mm diameter deformed bars (CSA-G30.12 grade 400) with recorded yield strength of 496 and 420 MPa and ultimate strength of 690 and 600 MPa respectively. The square specimens with side dimension of 1,500 mm center-to-center of supports were used throughout the study, with one exception where the side dimension of 1,830 mm was selected for slab HS17. In all cases, the slab extended 60 mm beyond the center of the supports. The slab HS17 under investigation is shown in Fig. 6.1.

The thick slabs with some cases of relatively high reinforcement ratios were chosen

based on the wide application of high-strength concrete in offshore structures, where heavy loads are expected. Test results revealed that high-strength concrete slabs behaved differently when compared to normal strength concrete slabs. High-strength concrete slabs exhibited a more brittle failure in general.

The test set-up is given in Fig. 6.2. Typical failure mode and cracking pattern at the ultimate load is photographically presented in Fig. 6.3.

The ultimate load carrying capacities and corresponding deflections of the slabs tested are listed in Tables 6.1 to 6.3, where the geometric and material parameters of studied slabs are also presented. In the present numerical investigation, the test results are used to verify the assumptions and performance of the material model implemented in the finite element program, especially for the heavily reinforced thick slabs made of high-strength concrete with silica fume and fly ash.

6.3 Comparison of F.E. model predictions to test results

6.3.1 General

The finite element numerical model formulated in the preceding chapter was used to analyse the slabs tested, with a plasticity-based material model implemented in the finite element program in the context of the 8-node shear-flexible thick shell element with all six degrees of freedom per node taken into account. The material model incorporated the realistic material properties of high-strength concrete and reinforcing steel from the laboratory testing and the analytical models of reinforced high-strength concrete behaviour after cracking, as developed in this study. A 2×2 reduced Gaussian integration rule was used over the plane of each element, while a

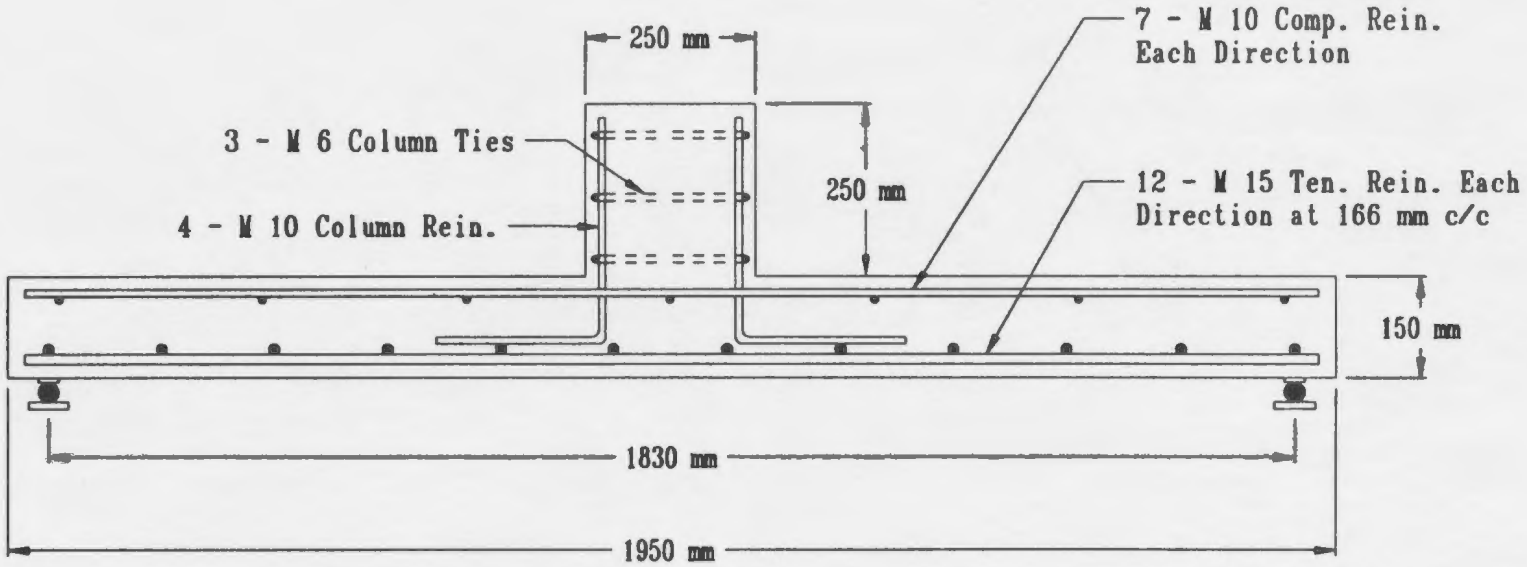

Figure 6.1: Reinforced high-strength concrete slab HS17 under investigation

Figure 6.2: Typical test set-up (slab HS17)

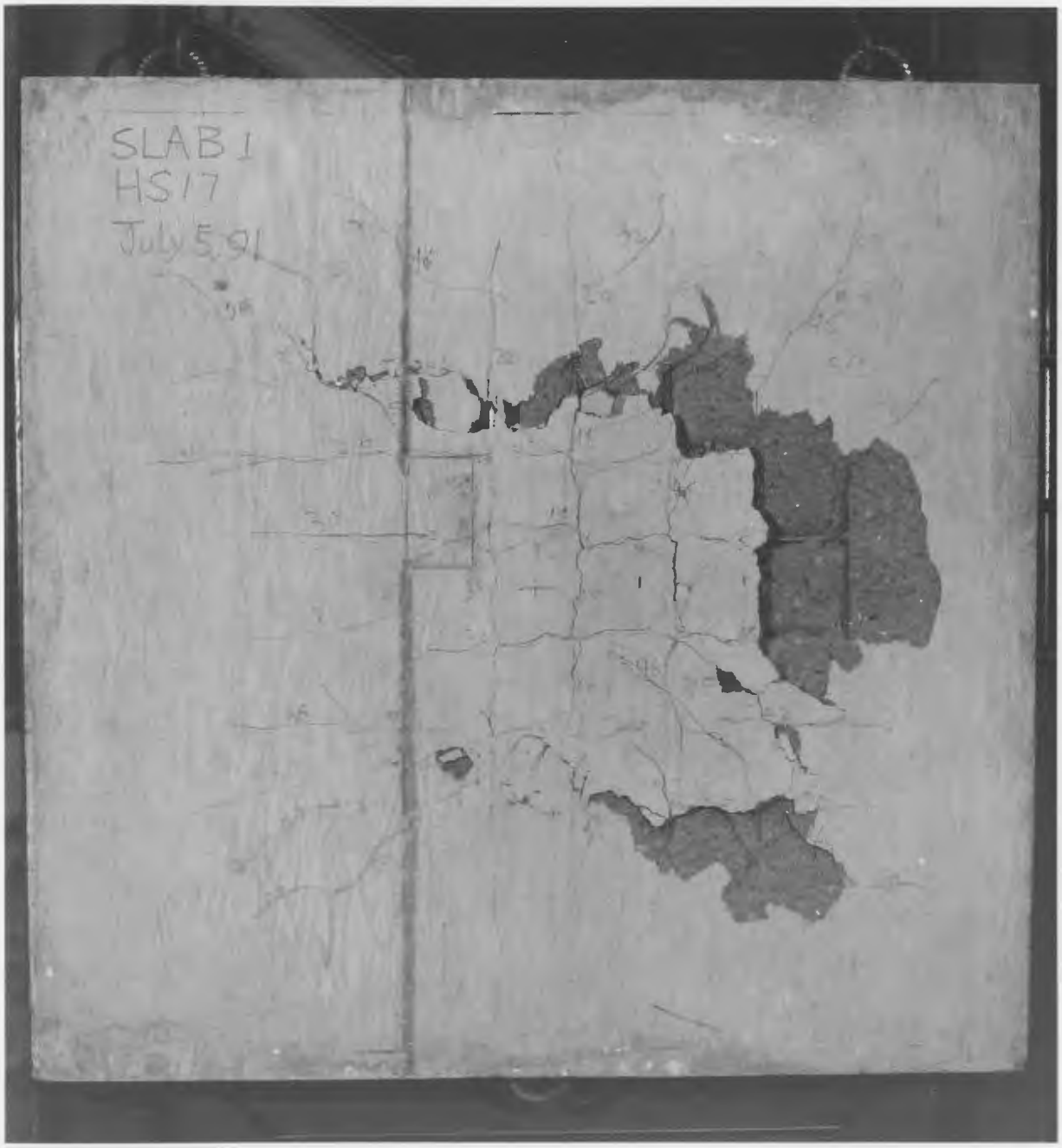

Figure 6.3: Typical cracking pattern of slabs at the ultimate load

nine-point Simpson integration rule was selected through the element thickness to account for severe material nonlinearity introduced by concrete cracking, crushing and reinforcement yielding.

The selection of nine-point Simpson type integration was based on the fact that the predictions of the model were basically same with any more than nine-point integration scheme over the element thickness. Thus, predictions were achieved more effectively and economically with the integration scheme selected.

6.3.2 Model predictions versus test results

The measured and computed ultimate loads and the associated deflections at the center of the analyzed specimens are given in Tables 6.1 to 6.3. For all the high-strength concrete slabs analyzed, the ratios of predicted-to-measured ultimate load ranged from 0.86-1.20, with an average value of 1.03 and standard deviation of 0.09, while the average ratio and standard deviation for the center deflections were 1.08 and 0.132 respectively, with the predicted values varying between 0.87-1.35 of the experimental results.

Generally, the model performed satisfactorily. The load-deflection diagrams obtained with the model followed the test measurements. The cracking and crushing patterns in the model predictions were close to the observations made during tests. The ratios of slab corner deflections to slab center deflections at peak load were also close to the experimental results. Typical load-deflection diagrams of the analyzed slabs are graphically presented in Figs. 6.4 to 6.11.

6.3.3 Discussion

In the previous experimental investigation, as described in the preceding sections, the failure modes of high-strength concrete slabs were classified into three categories: pure flexural failure, ductile shear failure and pure punching shear failure, based on the recorded load-deflection characteristics. The load-deflection diagrams of slabs HS1 and HS11 indicated that they failed by flexure. Nevertheless, none of these slabs reached the state of steadily increasing deflections at constant load, which is characteristic of a normally reinforced concrete specimen experiencing flexural failure. Therefore, the failure of the tested slabs is re-characterized into two basic modes in this study, namely, flexural shear failure and punching shear failure.

6.3.3.1 Slabs in flexural shear failure

Most of the tested high-strength concrete slabs fell into this category: flexural shear failure. The load-deflection characteristics of these slabs are shown in Figs. 6.4 to 6.8, as obtained from tests and model predictions respectively.

For the slabs with low and moderate reinforcement, where flexural shear failure is expected, the model predictions were in a good agreement with the experimental results (Figs. 6.4 to 6.8). The ratios of predicted-to-measured ultimate load ranged from 0.86-1.07, with an average value of 0.99 and standard deviation of 0.06, while the average ratio and standard deviation for the center deflections were 1.02 and 0.10 respectively, the predicted values varying between 0.87-1.18 of the experimental results. The test measurements and model predictions with respect to the ductility and ultimate strength capacity are presented in Table 6.1, where the details of the examined slabs are also given.

6.3.3.2 Slabs in punching shear failure

Slabs HS3, HS9, HS10 and HS13 were identified as failed in punching shear in the experimental investigation. The transverse shear stresses are dominant in these slabs, since they were heavily reinforced in general. It is evident that the performance of the formulated numerical model in this case is relatively less accurate than in the previous case. The ratios of predicted-to-measured ultimate load ranged from 1.07-1.20, with an average value of 1.13 and standard deviation of 0.05, while the average ratio and standard deviation for the center deflections were 1.24 and 0.11 respectively, the predicted values varying between 1.09-1.35 of the experimental results. The load-deflection diagrams from the tests and model predictions are shown in Figs. 6.9 through 6.10.

Although the formulation of the shear-flexible shell element provides five stresses (two in-plane axial stresses, one in-plane shear stress, and two out-of-plane or transverse shear stresses), only the three in-plane stresses are used for the material failure criteria. Such an assumption limits the application of the model to 2-D problems or to 3-D problems where transverse shear stresses are not dominant. Consequently, the model prediction becomes less accurate as the transverse shear stresses tend to be dominant.

6.3.3.3 Normal strength concrete slabs

Satisfactory model predictions were also achieved for the normal strength concrete slabs tested, as shown in Fig. 6.11. The comparison between the model predictions and experimental measurements with respect to the ultimate loads and deflections are listed in Table 6.3.

Table 6.1: Model predictions versus test results of slabs in flexural shear failure

Specimen	h (mm)	ρ (%)	f_y (MPa)	f'_c (MPa)	*Experimental*		*Model*		*Model/Test*	
					Δ_u (mm)	Q_u (kN)	Δ_u (mm)	Q_u (kN)	Δ_u	Q_u
HS 1*	120.	0.491	496	67	25.45	44.50	22.09	43.85	0.87	0.99
HS 2	120.	0.842	496	70	17.56	62.25	19.98	65.23	1.14	1.05
HS 7	120.	1.193	496	74	17.00	89.00	18.30	85.54	1.08	0.96
HS 4	120.	2.370	420	66	14.74	104.50	14.78	110.30	1.00	1.06
HS 5	150.	0.640	496	68	16.90	91.25	16.93	90.11	1.00	0.99
HS 6	150.	0.944	496	70	14.90	122.25	15.64	118.36	1.05	0.97
HS17	150.	1.093	420	67	23.43	127.77	23.91	121.64	1.02	0.95
HS 8	150.	1.111	420	69	13.10	109.00	15.47	116.16	1.18	1.07
HS11	90.	0.952	496	70	27.00	49.00	26.32	42.18	0.97	0.86
HS12	90.	1.524	496	75	26.30	64.50	23.70	62.29	0.90	0.97

Q_u=Ultimate load on quarter slab

*Ratio of strain energy density of tension stiffening to tension softening is 3.0 for slab HS 1 and 1.5 for all other slabs

Statistics:		
Average	1.02	0.99
Stand. dev.	0.10	0.06
Coeff. of var.	9.5%	6.3%

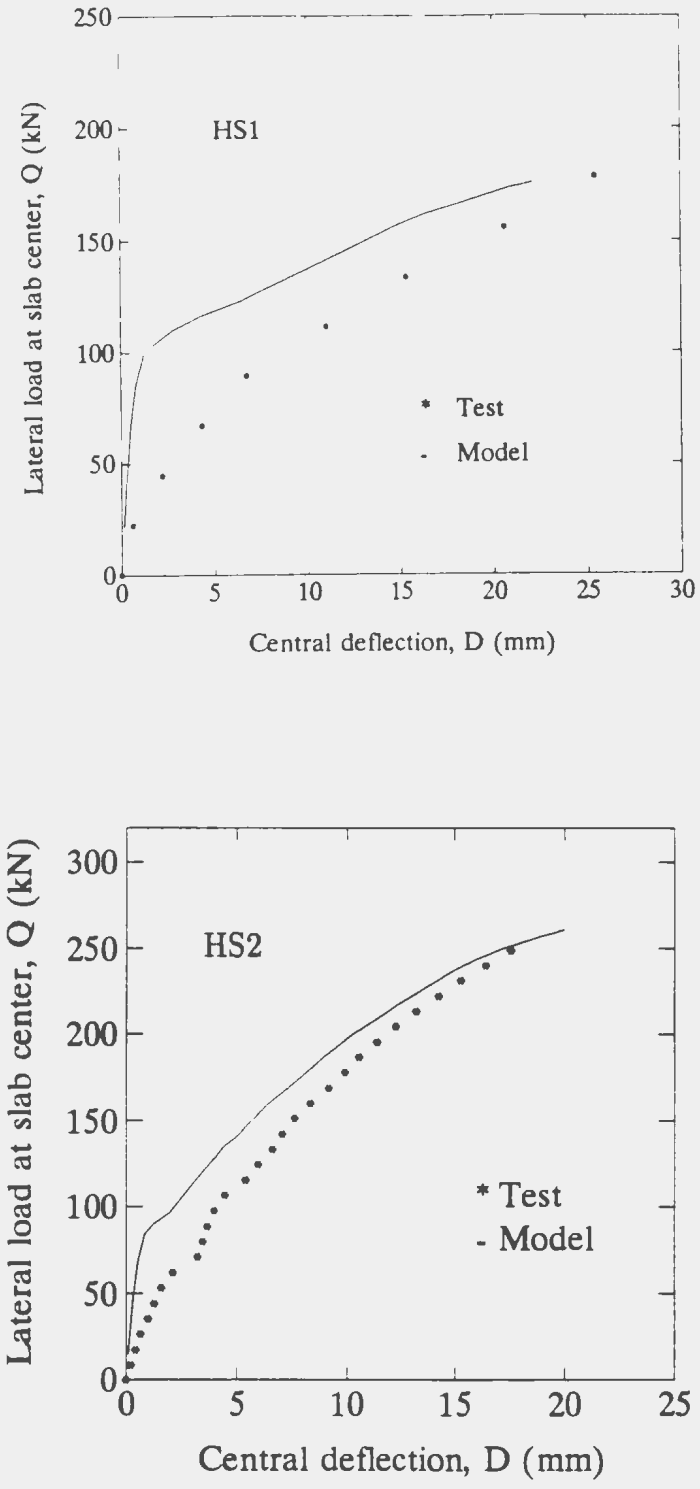

Figure 6.4: Comparison of model predictions to test results of slabs in flexural shear failure (HS1 and HS2)

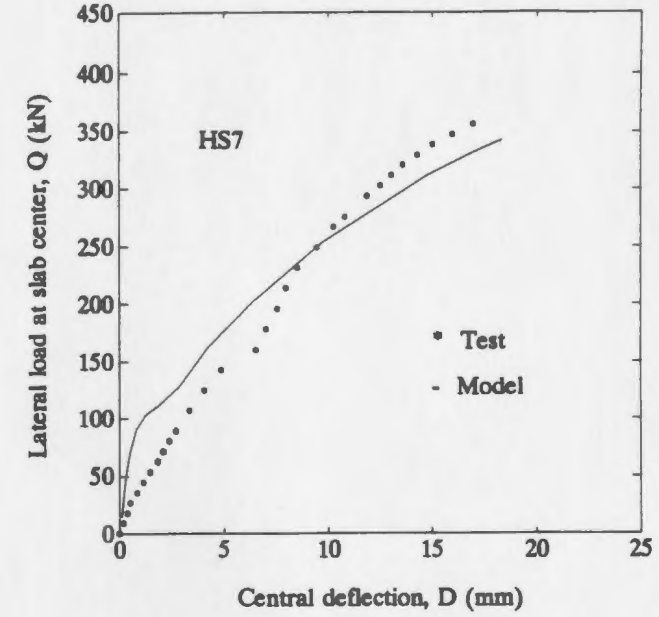

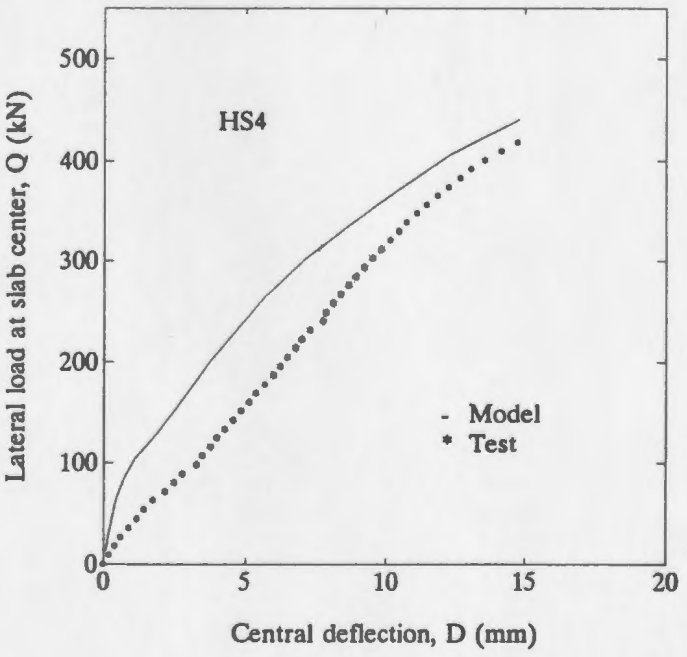

Figure 6.5: Comparison of model predictions to test results of slabs in flexural shear failure (HS7 and HS4)

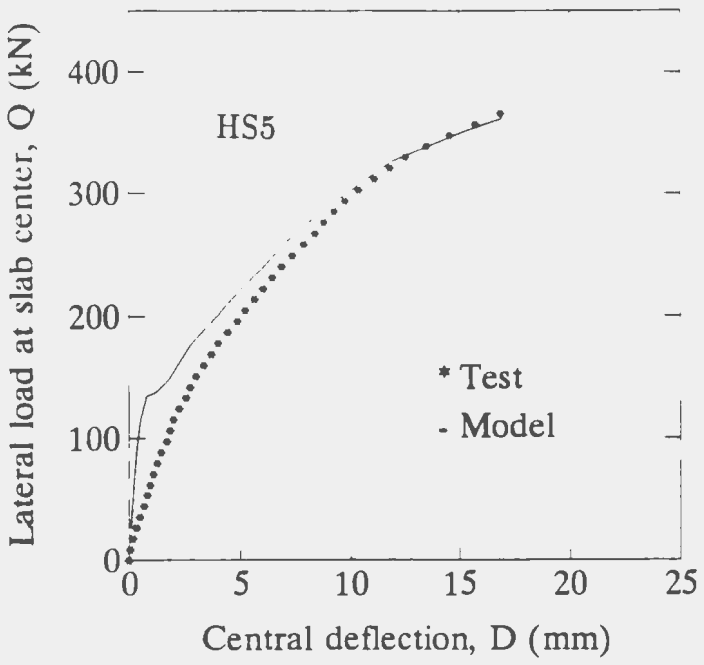

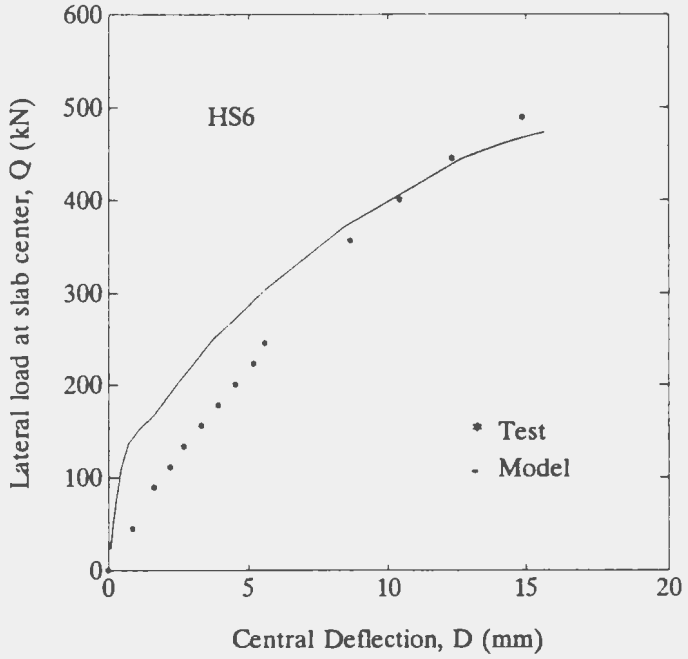

Figure 6.6: Comparison of model predictions to test results of slabs in flexural shear failure (HS5 and HS6)

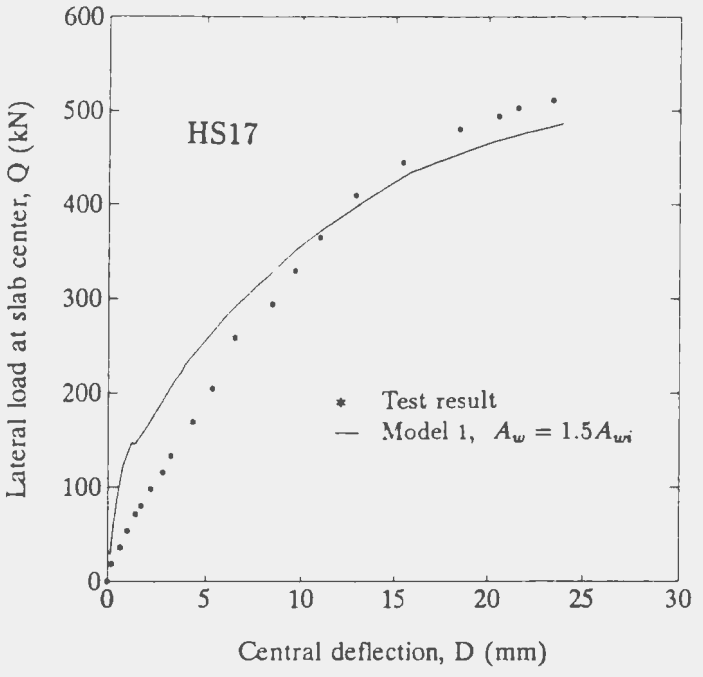

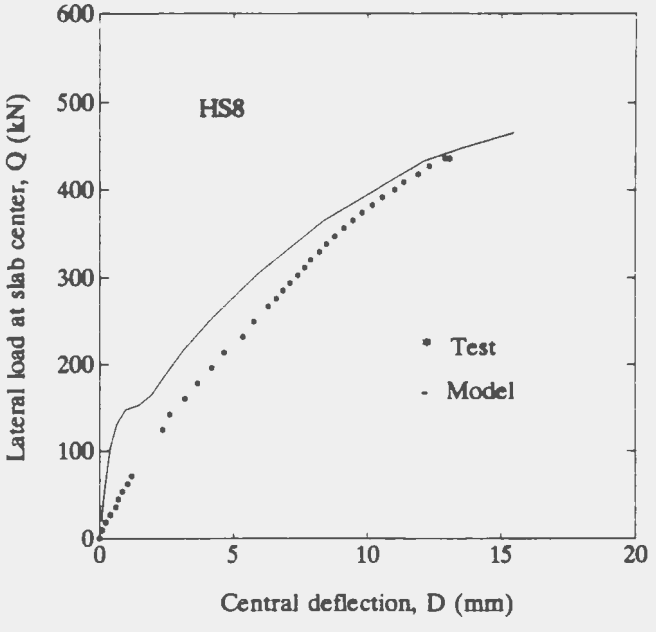

Figure 6.7: Comparison of model predictions to test results of slabs in flexural shear failure (HS17 and HS8)

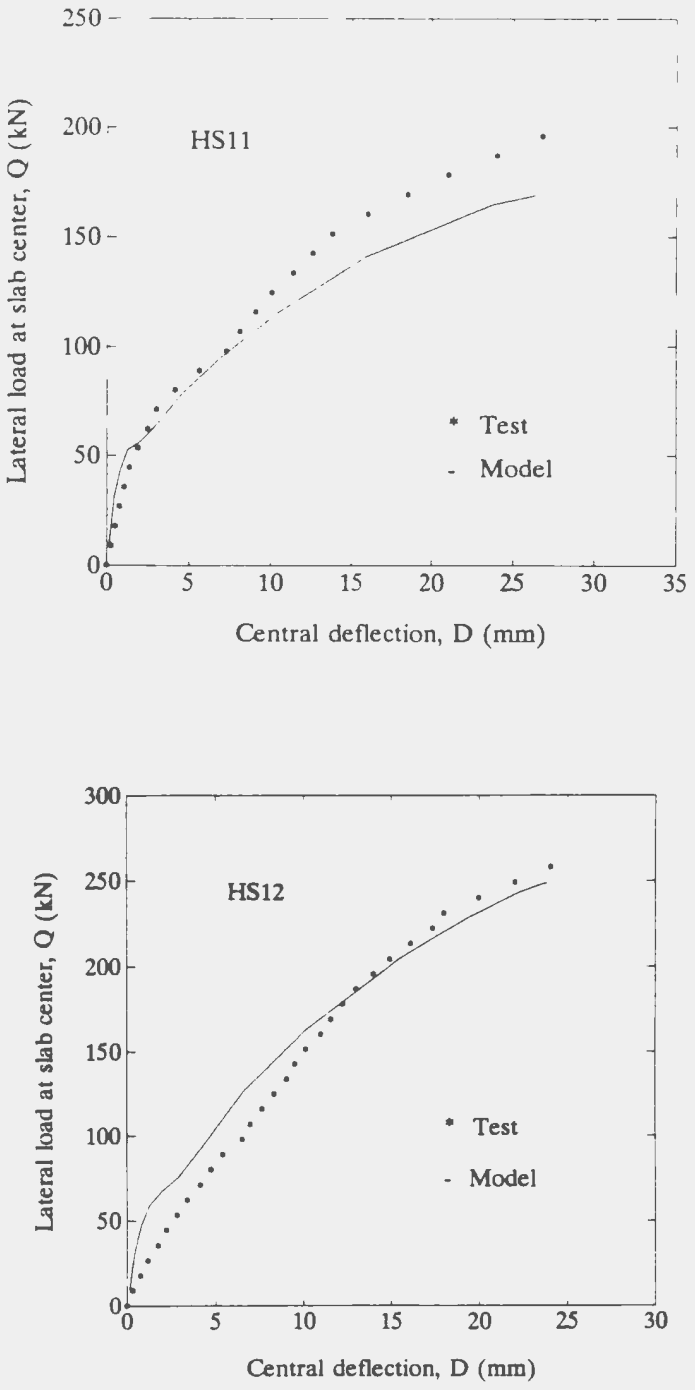

Figure 6.8: Comparison of model predictions to test results of slabs in flexural shear failure (HS11 and HS12)

Table 6.2: Model predictions versus test results of slabs in punching shear failure

Specimen	h (mm)	ρ (%)	f_y (MPa)	f'_c (MPa)	*Experimental*		*Model*		*Model/Test*	
					Δ_u (mm)	Q_u (kN)	Δ_u (mm)	Q_u (kN)	Δ_u	Q_u
HS 3	120.	1.474	496	69	13.10	89.00	17.70	99.68	1.35	1.12
HS 9	150.	1.611	420	74	10.80	135.75	13.94	155.04	1.29	1.14
HS10	150.	2.333	420	80	10.40	161.25	11.33	194.21	1.09	1.20
HS13	90.	2.000	496	68	16.15	66.75	19.82	71.30	1.23	1.07

Q_u=Ultimate load on quarter slab
Strain energy density of tension stiffening
equals 1.5 times that of tension softening

Statistics:

Average	1.24	1.13
Stand. dev.	0.11	0.05
Coeff. of var.	9.0%	4.8%

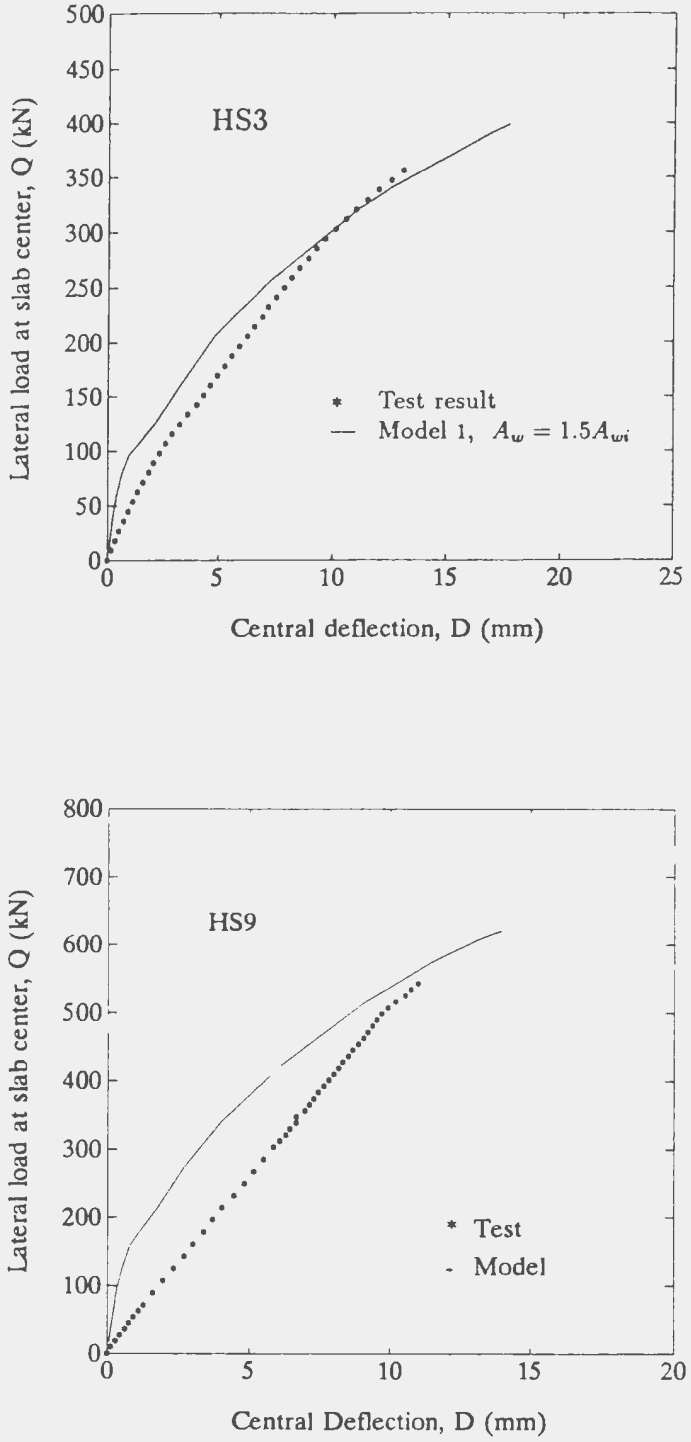

Figure 6.9: Comparison of model predictions to typical test results of slabs in punching shear failure (HS3 and HS9)

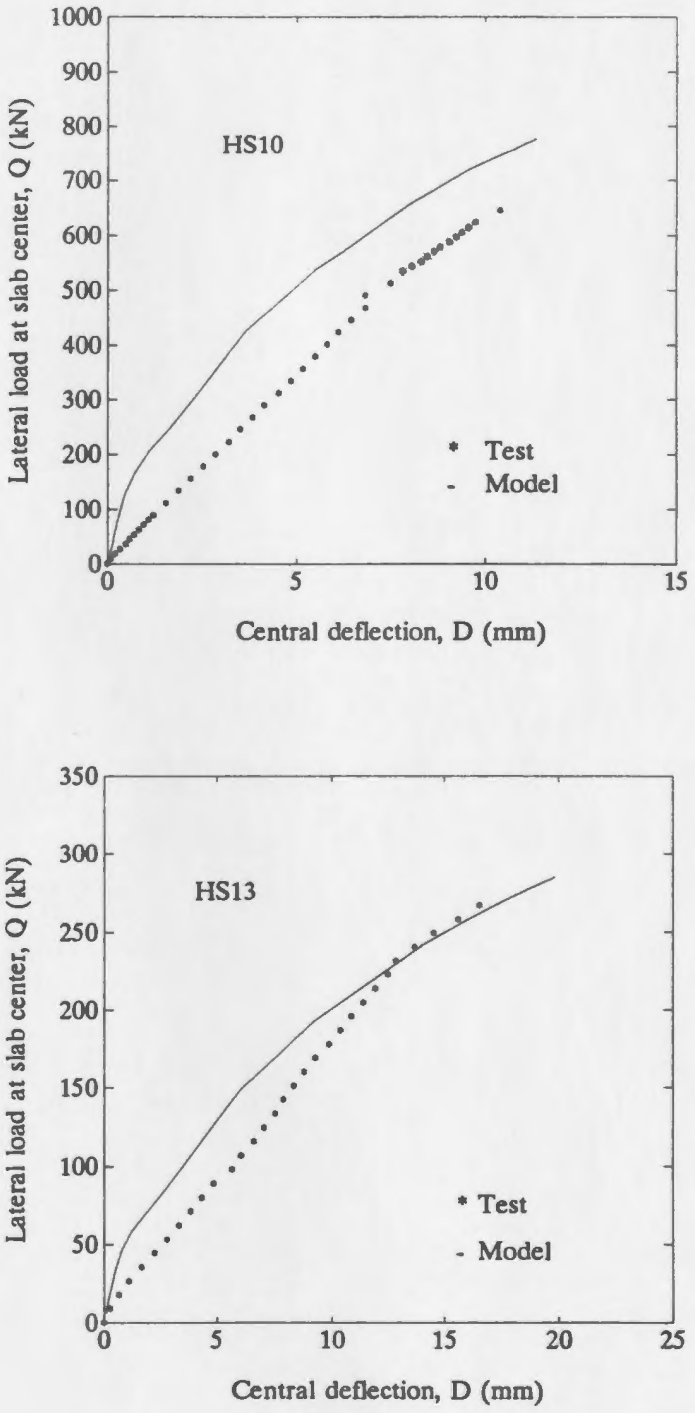

Figure 6.10: Comparison of model predictions to typical test results of slabs in punching shear failure (HS10 and HS13)

Table 6.3: Model predictions versus test results of normal strength concrete slabs

Specimen	h (mm)	ρ (%)	f_y (MPa)	f'_c (MPa)	*Experimental*		*Model*		*Model/Test*	
					Δ_u (mm)	Q_u (kN)	Δ_u (mm)	Q_u (kN)	Δ_u	Q_u
NS 1	120.	1.473	496	42	14.60	80.00	16.01	89.94	1.10	1.12
NS 2	150.	0.944	496	30	13.07	99.00	13.76	100.75	1.05	1.02

Q_u=Ultimate load on quarter slab
Strain energy density of tension stiffening
equals 1.5 times that of tension softening

Statistics:		
Average	1.08	1.07
Stand. dev.	0.04	0.07
Coeff. of var.	3.3%	6.6%

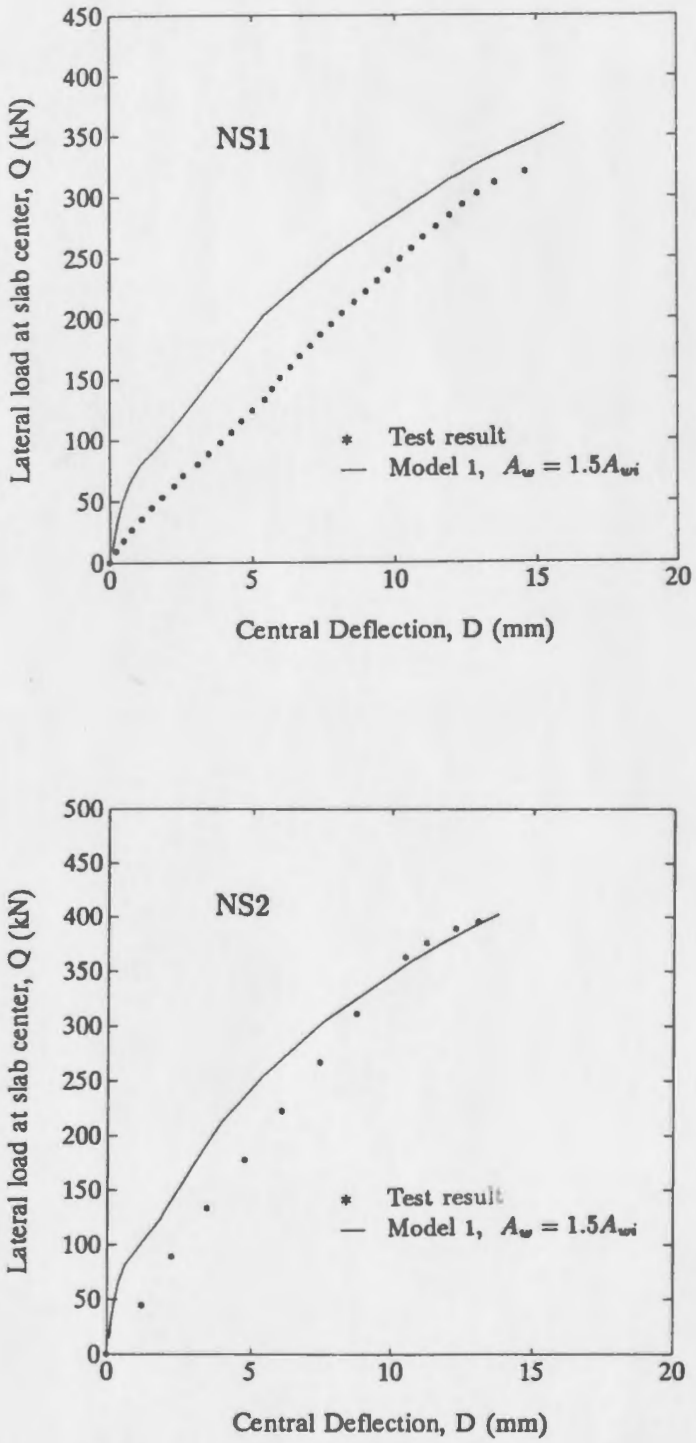

Figure 6.11: Comparison of model predictions to test results of normal strength concrete slabs (NS1 and NS2)

6.3.4 Summary

Based on the comparison of the model predictions to the experimental results, it can be concluded that the formulated finite element numerical model with a plasticity-based material model implemented in the finite element program in the context of the shear-flexible shell element can adequately model the thick high-strength concrete slabs with relatively heavy reinforcement and can be used with confidence to predict the behaviour and the ultimate carrying capacity of such slabs. However, it must be pointed out that the model prediction for slabs failed due to punching shear (slabs HS3, HS9, HS10 and HS13) is less accurate. The satisfactory agreement of model predictions to experimental results are achieved only with the incorporation of the realistic material properties and appropriate representation of post-cracking behaviour of reinforced high-strength concrete, as developed in this research.

Chapter 7

Tension Stiffening Model and a Parametric Study on High-Strength Concrete Slabs

7.1 Introduction

A recommended tension stiffening model is formulated in this chapter, based on the tension softening model (chapter 4) and comparison of finite element predictions to experimental results of reinforced high-strength concrete slabs. A bilinear tension stiffening model is also suggested for the sake of simplicity. The importance of the tension stiffening behaviour of reinforced high-strength concrete is demonstrated in the finite element analysis of the slab selected.

A parametric study is then initiated to examine the structural behaviour of reinforced high-strength concrete slabs under various conditions, in an attempt to extend the range of the experimental investigation. The sensitivity of the material model to the separate material properties is demonstrated, along with the effects of slab boundary conditions, loading stub-column, loading type and sequence.

7.2 Post-cracking tensile behaviour of reinforced high-strength concrete

The experimental investigation on the tension softening behaviour of plain high-strength concrete (Chapter 3) has confirmed that after cracking the concrete between two adjacent cracks is still capable of resisting tensile forces, thereby increasing the average stiffness of the member. In the case of reinforced concrete, it has been found that the concrete tensile capacity after cracking is further enhanced as a result of interaction between reinforcing steel and concrete, as reported by various investigators such as William (1986) and Clark and Speirs (1978). This phenomenon is called as "tension stiffening" in the literature.

It has been well established that the tension-stiffening effect of reinforced concrete is dependent on the percentage of steel, diameter of steel reinforcement, distribution of reinforcement and bond stresses. Also, it has been found that tension stiffening is more pronounced in the reinforced concrete element with low percentage of reinforcement. Thus the tension stiffening effect must be properly represented in the calculation of the structural behaviour of reinforced high-strength concrete slabs, in order to achieve valid numerical predictions.

7.2.1 Tension stiffening model for reinforced high-strength concrete slabs

In this study, a tension stiffening model is recommended, based on the tension softening model (chapter 4) and a parametric study of reinforced high-strength concrete slabs. The analytical expresion of the tension softening behaviour of plain high-strength concrete is modified with respect to the descending branch of the stress-

strain curve in an attempt to reflect the tension stiffening behaviour of reinforced high-strength concrete. A similar approach was used by Prakhya and Morley (1990) for the flexural members of normal strength concrete.

The tension softening model, as developed in the chapter 4, is analytically expressed as

$$y = 2x - x^2 \qquad x \leq 1.0 \tag{7.1}$$

$$y = \frac{x}{\alpha(x-1)^{\beta} + x} \qquad x \geq 1.0 \tag{7.2}$$

where,

y	=	the relative stress f_t/f'_t
x	=	the relative strain ϵ_t/ϵ_{to}
α, β	=	material costants

It is derived in chapter 4 that α and β are 2.84 and 1.6655 respectively, based on the best fit of the developed tension softening model to the experimental measurements of plain high-strength concrete under direct uniaxial tension. The above expressions can also be used to represent the tension stiffening effect of reinforced high-strength concrete, provided the material constants (α and β) are properly related to the enhancement of concrete tension carrying capacity due to interaction between reinforcing steel and concrete.

In fact, the modification of the tension softening behaviour into a tension stiffening model can be easily accomplished by changing the value of the constant α in Eq. 7.2. The change of α values will change the strain energy density or the total area under the curve from A_{wi} to A_w, where A_{wi} and A_w are strain energy density required to

open a crack for plain and reinforced high-strength concrete respectively. The tension stiffening model developed thereafter is shown in Figs. 7.1 and 7.2.

The initial portion of the tension stiffening curve up to a normalized average strain of ϵ_t/ϵ_{to}=4 is shown in Fig. 7.1, along with the test data of plain high-strength concrete under direct uniaxial tension. The normalized strain value of ϵ_t/ϵ_{to}=16 (Fig. 7.2) is used as a cut-off point for the integration process, since the concrete tensile capacity beyond this point tends to be negligible. The same cut-off point was recommended by Massicotte et al. (1990) for normal strength concrete.

A parametric study was carried out to establish the area under the stress-strain diagram, in order to convert the tension softening behaviour (A_{wi}) into the tension stiffening behaviour (A_w). The experimental results of reinforced high-strength concrete slabs tested at Memorial University, as described in the preceding chapter, were utilized in the parametric study to determine the tension stiffening magnitude for reinforced high-strength concrete slabs. Various estimates of tension stiffening enhancement on the tension softening behaviour of high-strength concrete, in terms of strain energy density (A_w) calculated from the tensile stress and average crack opening strain diagram, were examined in this parametric study. It was found that for slabs with high to moderate steel reinforcement ratios, the tension stiffening values can be represented as follows:

$$A_w = (1.20 \sim 2.0)A_{wi} \tag{7.3}$$

For slabs with low steel reinforcement ratios, the tension stiffening values ranged between

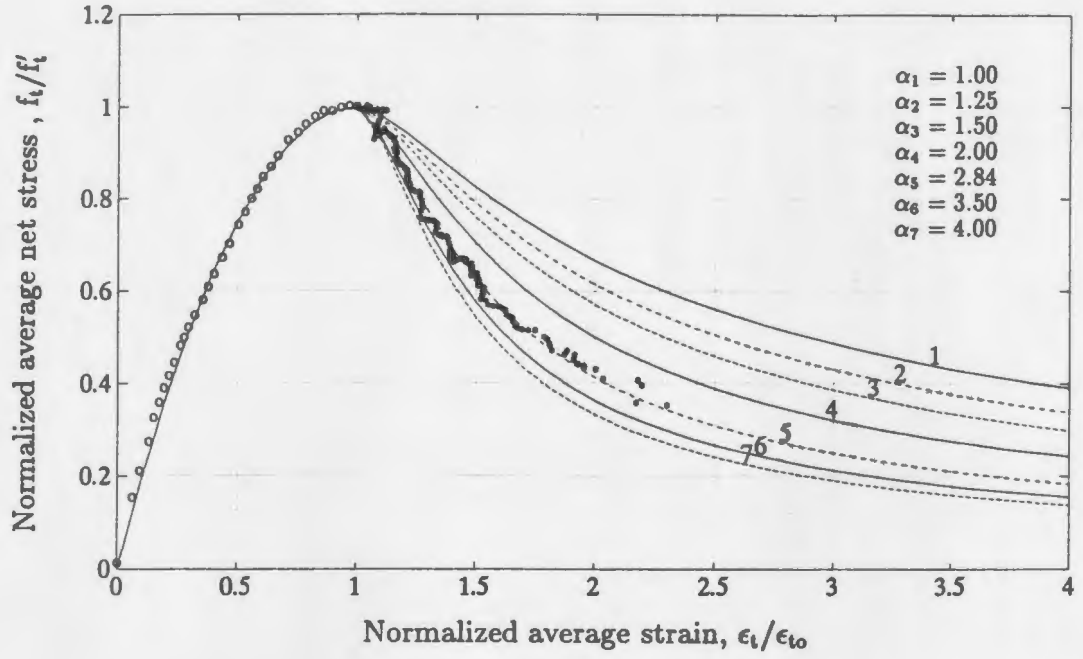

Figure 7.1: Tension stiffening model of high-strength concrete up to four times tensile strain at the peak load

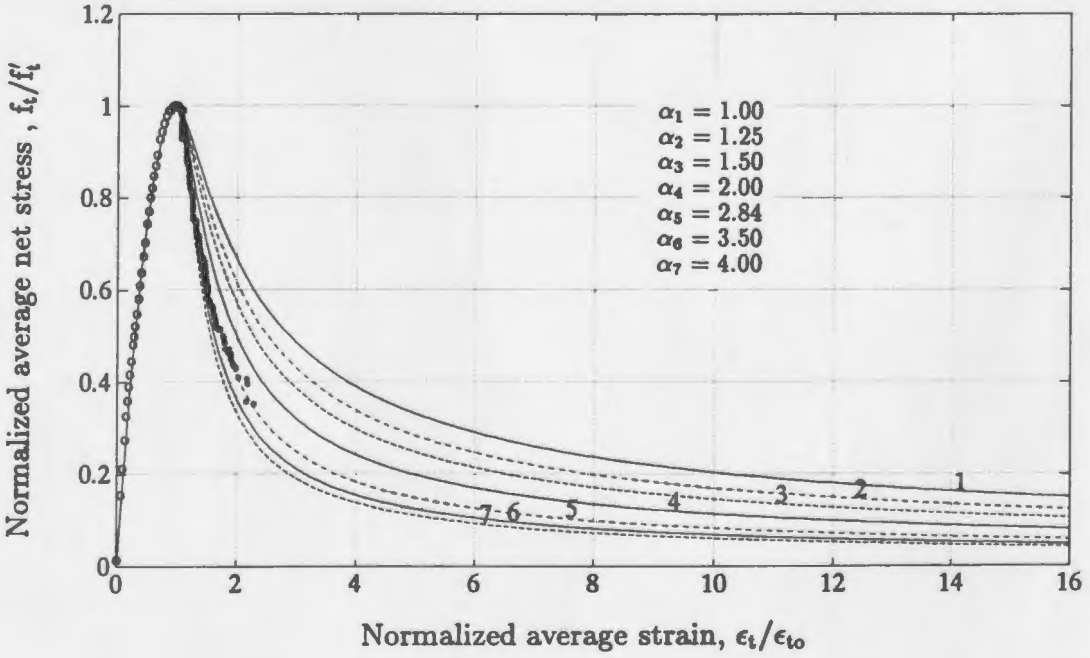

Figure 7.2: Complete tension stiffening model of high-strength concrete

$$A_w = (2.0 \sim 3.0)A_{wi} \tag{7.4}$$

In the validation tests of the formulated finite element model (Chapter 6), the strain energy density (A_w) of reinforced concrete equal to 1.5 times that of plain concrete (A_{wi}) was chosen for all the analyzed slabs except slab HS1, where A_w was equal to 3.0 A_{wi} due to very low reinforcement ratio employed. The model predictions are given in Tables 6.1 to 6.3 in the preceding chapter, together with the experimental results. As can been seen in these tables, the model predictions followed test data satisfactorily. Thus, the tension stiffening value of A_w=1.5×(A_{wi}), can be proposed for moderate reinforced high-strength concrete slabs.

Therefore, the expressions (Eqs. 7.1 and 7.2) can be modified into a tension stiffening model by changing the constant α from α=2.84 to α=1.3863. The tension stiffening model for reinforced high-strength concrete slabs, referred as model 1, is recommended as follows:

$$y = 2x - x^2 \qquad x \leq 1.0 \tag{7.5}$$

$$y = \frac{x}{1.3863(x-1)^{1.6655} + x} \qquad x \geq 1.0 \tag{7.6}$$

where, x and y are same as those defined in Eq. 7.2.

In order to illustrate the effect of tension stiffening values on the structural behaviour of reinforced high-strength concrete slabs, the slab HS5 tested by Marzouk and Hussein (1991) was further examined. Different tension stiffening values were assumed, by multipling the area (A_{wi}) under the stress-strain curve of plain high-strength concrete by factors of 2.6, 1.7, 1.50 and 1.20. The corresponding predictions

of the finite element model are presented in Fig. 7.3, along with the experimental measurement of the slab HS5.

7.2.2 Simplified idealization of tension stiffening model

The continuous tension stiffening model, recommended as given by Eqs. 7.5 and 7.6, may cause difficulties in its implementation in certain finite element program. In such a case, a simplified idealization of tension stiffening model is needed.

In this study, it has been found that a simplified bilinear stress-strain curve can also provide a good result, provided the area under the complete stress-strain curve of high-strength concrete is only about five times the area under its ascending portion, and the appropriate steel reinforcement ratio modification factors represented by Eqs. 7.3 and 7.4 are incorporated.

The simplified bilinear tension stiffening model is commonly adopted in many available commercial software, which is presented in the inset of Fig. 7.4 (referred as model 2). It is similar to that recommended by Bazant and Oh (1983). The significant effect of tension stiffening values on the structural behaviour of reinforced high-strength concrete slabs is also demonstrated in Fig. 7.4, where the bilinear tension stiffening model was implemented in the finite element program. In the same figure, an extremely high tension stiffening value of A_w=5.3A_{wi} was assumed as an unrealistic case to illustrate the strong effect of concrete tension stiffening behaviour.

7.2.3 Discussion

It is found that the post-cracking tensile behaviour of high-strength concrete affects not only the load carrying capacity but also the entire load-deflection characteristics of the analyzed slab, particularly in the serviceability range of the load, as illustrated in

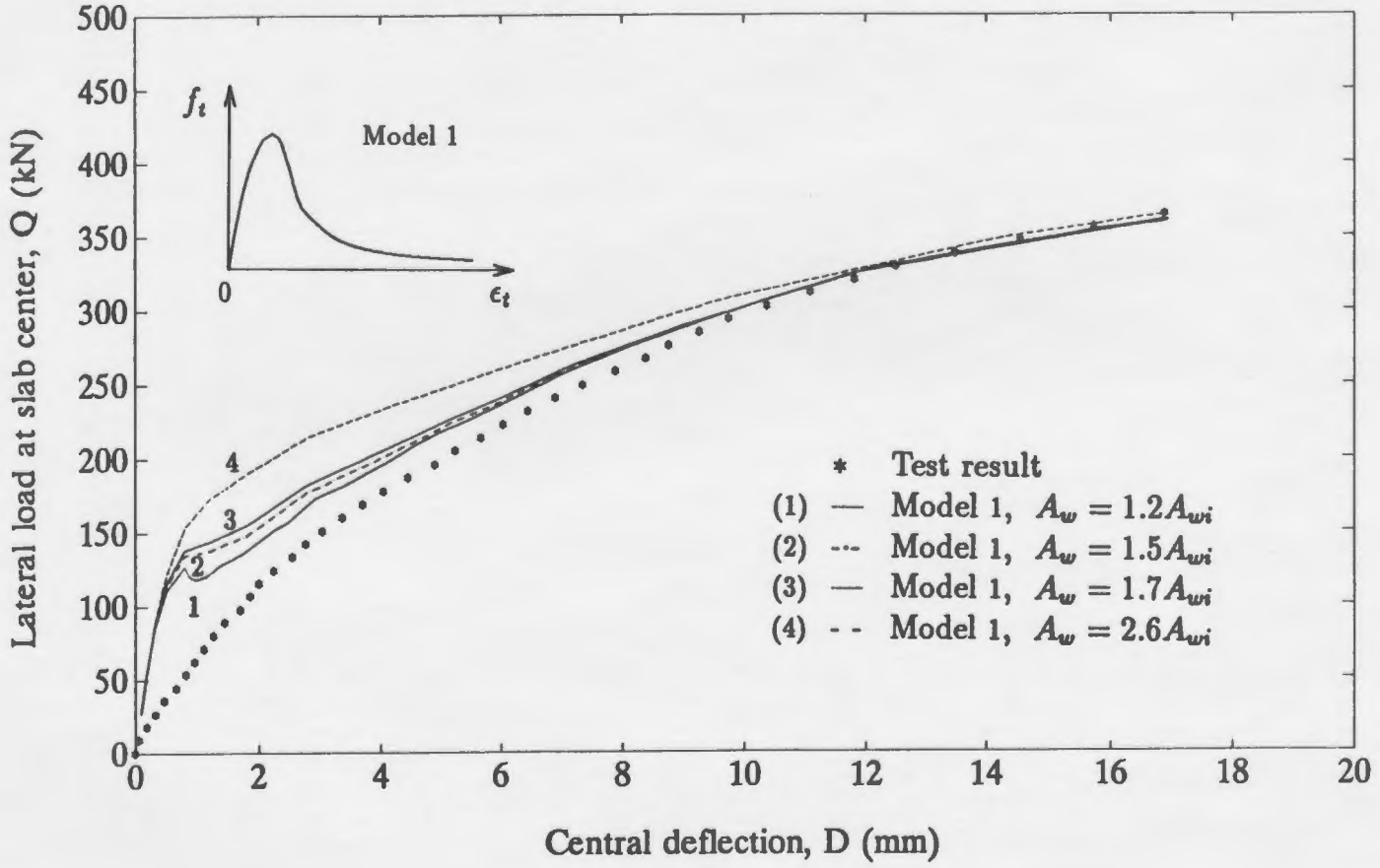

Figure 7.3: Tension stiffening effect on slab HS5, using the recommended tension stiffening model

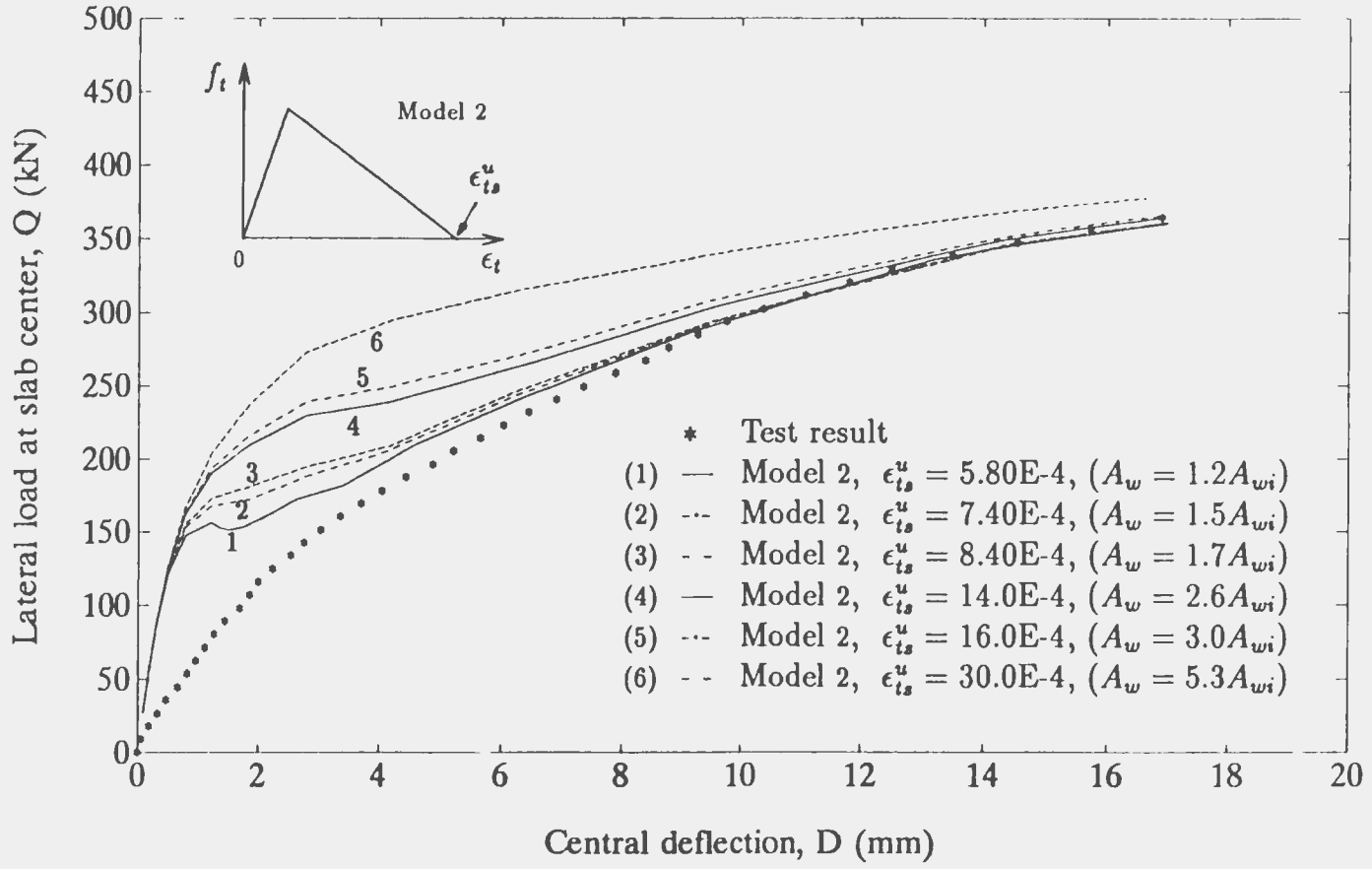

Figure 7.4: Tension stiffening effect on slab HS5, using a simplified bilinear tension stiffening model

Figs. 7.3 and 7.4. Therefore, a correct determination of high-strength concrete post-cracking behaviour is important. There is a great need to perform a comprehensive and detailed study on the concrete tension stiffening behaviour with respect to the percentage of steel, diameter of the reinforcing bars, bond stress, concrete strength, and the distribution of reinforcement. However, this study falls beyond the scope of the present thesis.

7.3 Numerical analysis of reinforced high-strength concrete slabs

A parametric study is initiated in this section to analyze the structural behaviour of reinforced high-strength concrete slabs under various conditions, in an attempt to extend the range of the experimental investigation. The sensitivity of the material model to the separate material properties is demonstrated, along with the effects of slab boundary conditions, loading stub-column, loading type and sequence. The slab HS17 is selected for the parametric study.

7.3.1 Steel yielding stresses and concrete cover

The effects of reinforcement yield strength and concrete cover on the response of the high-strength concrete slab studied are illustrated in Figs. 7.5 and 7.6. The sensitivity of the model prediction to the separate material parameters are clearly demonstrated. The importance of the correct determination of the material properties is clearly indicated.

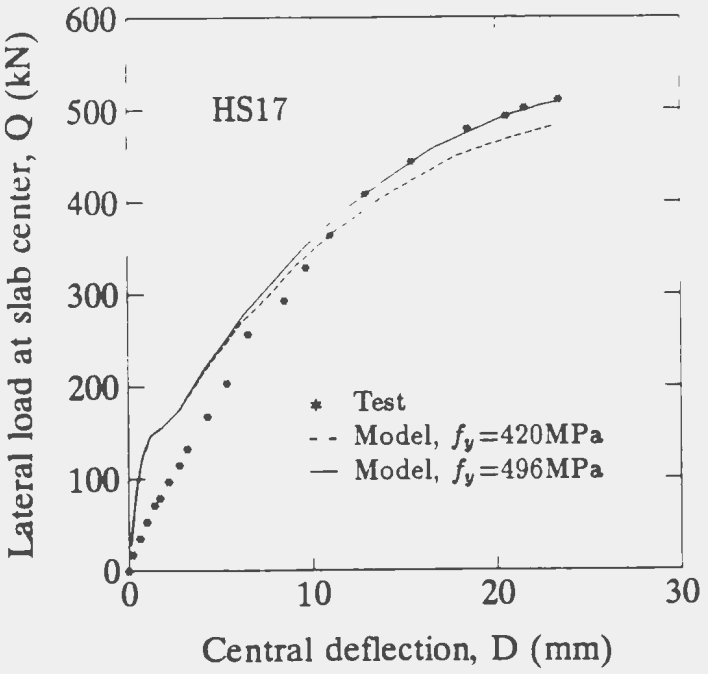

Figure 7.5: Effect of steel yielding stresses, HS17

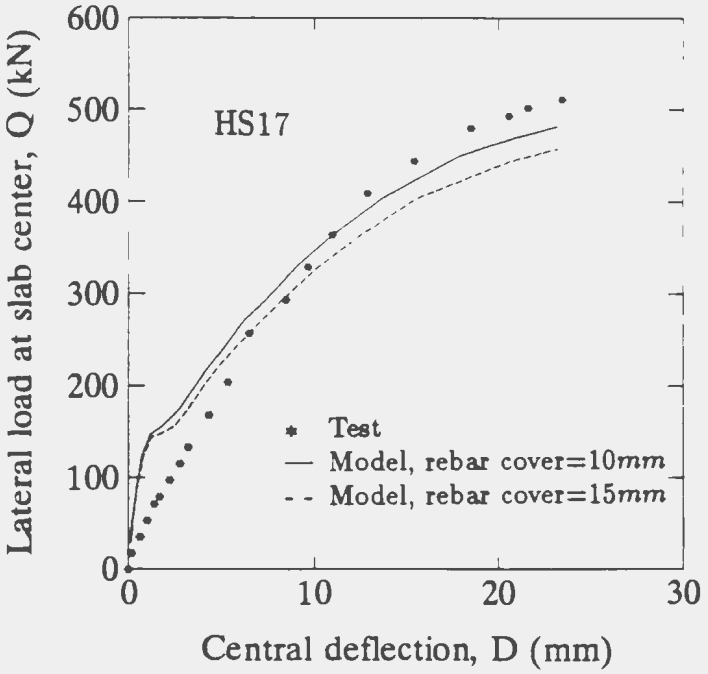

Figure 7.6: Effect of steel locations, HS17

7.3.2 Boundary conditions

The addition of edge restraints as a boundary condition in the finite element numerical model largely improved the load carrying capacity, while the slab ductility was significantly reduced. Both rotational and in-plane translational edge restraints were considered. Figure 7.7 shows the strong effect of the rotational edge restraint on the ultimate lateral load and corresponding deflection as expected for the thick clamped slabs. This behaviour is different from that of slender panels with moderate reinforcement where both the load carrying capacity and ductility were improved with the application of edge restraints (Massicotte et al., 1989).

7.3.3 Loading stub-column

Proper simulation of the loading stub-column also had strong effect on slab response, as shown in Fig. 7.8. The loading stub-column was represented by 3-D brick element with 20 nodes per element, where reduced Gaussian $2 \times 2 \times 2$ integration scheme was adopted. The restraints between the nodes of shell element and brick element were imposed by using the multi-point constraint (MPC) technique, in which constraints between different degrees of freedom of the model can be specified even in nonlinear and inhomogeneous cases in the selected finite element program. Constraints are usually imposed in a model by any of the three methods: penalties, Lagrange multipliers, or direct elimination. In this analysis, MPC's were imposed by directly eliminating degrees of freedom at the nodes where to impose the constraints.

The interaction of loading actuator with the loading stub-column was modeled through the use of interface element, which consists of nodes on the deforming loading stub-column and on the rigid surface of the loading actuator. The accurate represen-

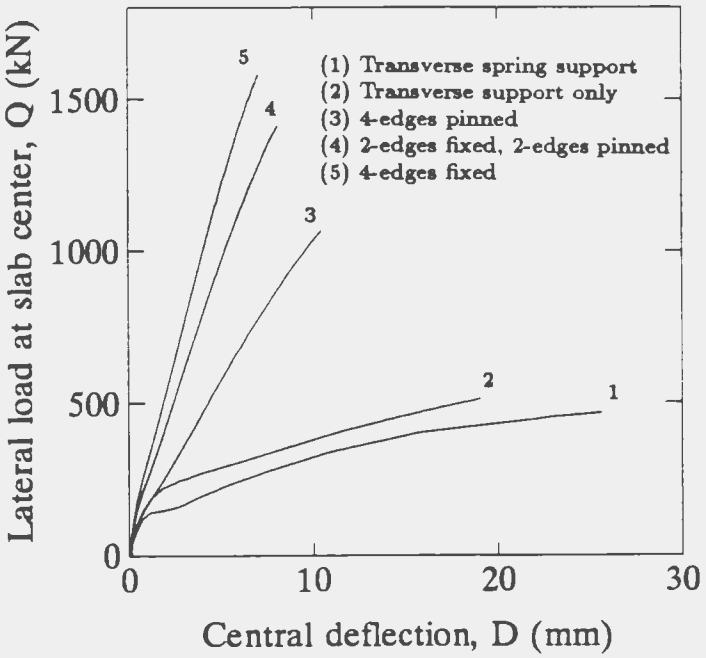

Figure 7.7: Effect of various boundary conditions, HS17

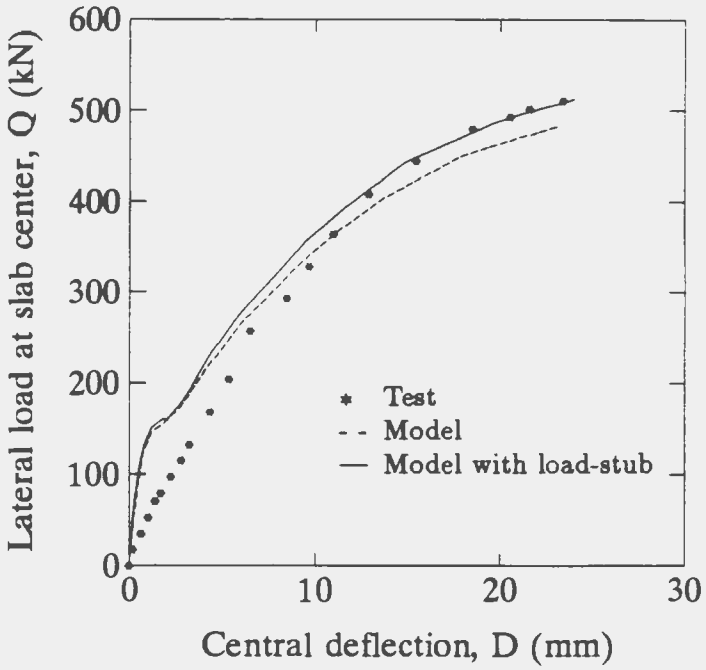

Figure 7.8: Effect of the loading stub-column, HS17

tation of the realistic contact conditions were achieved by using this technique, which produced the relatively better results for the slab analyzed, as shown in Fig. 7.8.

7.3.4 Slabs loaded axially and transversely

The behaviour of normal strength concrete slabs loaded axially and transversely was recently examined at the University of Alberta recently. Their study was conducted on normal strength concrete slab panels with uniaxial concrete compressive strength f'_c of about 35 MPa. The results of these investigations are used to compare with the predicted behaviour of high-strength concrete slabs.

7.2.4.1 Magnitude of the in-plane load

In order to investigate numerically the effect of the in-plane loading on the response of high-strength concrete slab supported on four edges and free to rotate and unrestrained in the in-plane direction, slab HS17 is selected for the parametric study. The uniaxial concrete compressive strength of slab HS17 was 67 MPa; the reinforcement ratio ρ was 1.093%; and the overall dimensions are 1950 x 1950 x 150 mm.

It was found that the lateral load carrying capacity of slab HS17 was generally improved with the application of the in-plane load. It was also observed that lateral load carrying capacity was further improved with the increase of in-plane load magnitude, as shown in Fig. 7.9. The applied in-plane load relative magnitude I_m varied between 0.10 and 0.40, where I_m is

$$I_m = \frac{P}{a \cdot h \cdot f'_c} \tag{7.7}$$

in which P = the total in-plane load; a and h = the width and the thickness of

the slab respectively; and f'_c = the ultimate uniaxial concrete compressive strength. This behaviour indicates that the compressive membrane force introduced by axial in-plane load, enhanced the lateral load capacity in a similar fashion to the prestressing of concrete members. However, ductility was significantly reduced due to the application of in-plane load, but remained basically the same with further increase of in-plane load magnitude. Finally, the analyzed slab failed due to concrete crushing (brittle failure) before the extensive yielding was developed due to the initial compressive strain introduced by the axial in-plane load. Similar results were reported for normal strength stocky panels by Massicotte et al. (1989).

7.2.4.2 Loading sequence

The effect of the loading sequence on slab HS17 is demonstrated in Fig. 7.10. In the first case, the lateral load Q, was applied up to a load of 440 kN, close to the ultimate load capacity of the slab under lateral load alone (Q = 512.0 kN). Then the lateral load was kept constant while the in-plane load was being applied, up to a value of I_m = 0.11. In the second case, the in-plane load was applied to I_m = 0.11 and kept constant while the lateral load was increased until it reached the value of Q = 456.0 kN. This was close to the failure load in the first case, but ductility was significantly reduced. The best performance of the slab was achieved in the third case, where the lateral and in-plane loads were applied proportionally. This produced a lateral load value of Q = 772.0 kN and I_m = 0.19. The lateral load carrying capacity was improved by 75% and the corresponding deflection was also the largest among the three cases analyzed. However, the ductility of the analyzed slab was consistently reduced due to in-plane load, regardless of loading sequence as shown in Fig. 7.11,

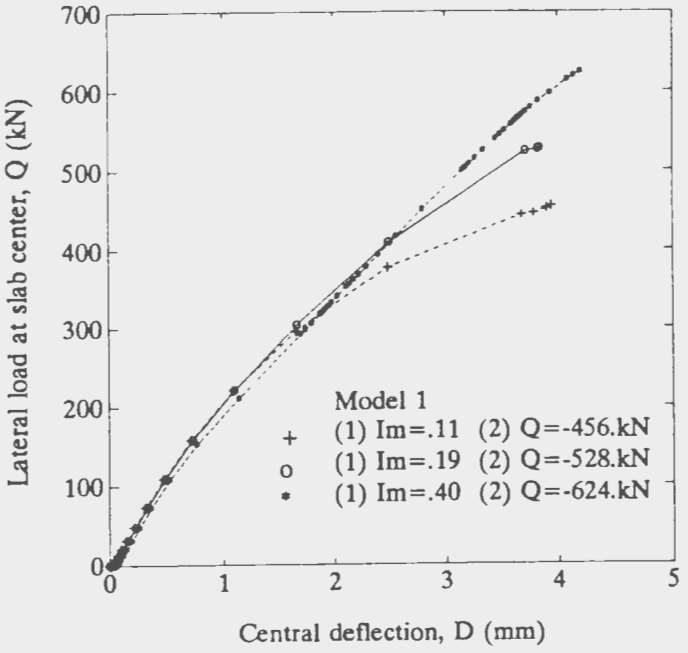

Figure 7.9: Effect of magnitude of the in-plane load, HS17

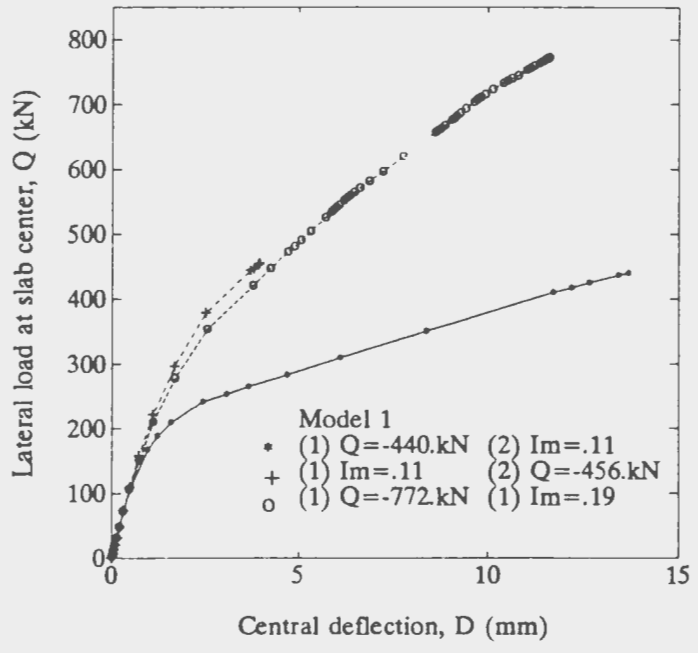

Figure 7.10: Effect of loading sequence, HS17

where the structural response of the the slab under proportional lateral and in-plane loading is compared to that of the slab under lateral loading alone.

It was found that the extensive cracking of such a slab was prevented by the application of the in-plane load. Thus, a more brittle failure is evident. In general, a reduction of about 43% in lateral load carrying capacity was associated with prior application of either P or Q to the slab under both axial in-plane and lateral loads. This indicates the slab response could be very sensitive to the loading sequence.

Massicotte et al. (1989) reported similar effects of the loading sequence on the thick normal strength concrete slabs. It was reported that when lateral load was applied first, lateral deflection was significantly larger than those in the case of proportional loading and the case of applying in-plane load first. This behaviour can be explained due to extensive cracking and the impact of the second order effects.

7.4 Summary

The post-cracking behaviour and the fracture energy of high-strength concrete are different from those of normal strength concrete. The difference is clearly indicated by the stress-strain curve of plain high-strength concrete under direct tensile load, the area under the complete curve (A_{wi}), and the ratio of the total area (A_{wi}) to that under the ascending portion. The total area (A_{wi}) under the stress-strain curve is about five times that under the ascending region for high-strength concrete; the corresponding value is about ten for normal strength concrete. This fundamental difference must be reflected in the analysis of high-strength concrete slabs.

A tension stiffening model is recommended for the analysis of reinforced high-strength concrete slabs. The model is based on the experimental measurements of

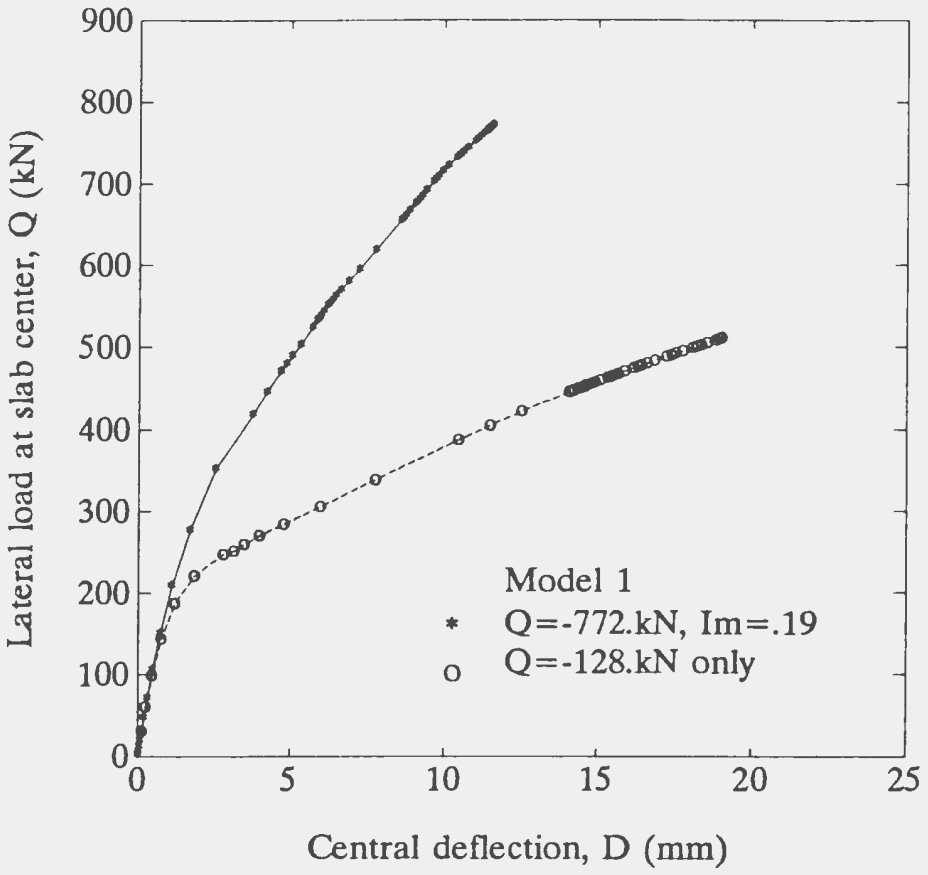

Figure 7.11: Effect of I_m at proportional loading, HS17

strain-softening behaviour of plain high-strength concrete under direct uniaxial tension, and the comparison of numerical predictions to experimental results obtained from the tests on the structural behaviour of reinforced high-strength concrete slabs.

A bilinear tension stiffening model is also proposed for simplification. This simplified idealization is especially useful when the recommended continuous tension stiffening model (Eqs. 7.5 and 7.6) poses difficulties in its implementation in certain finite element programs. However, the strain energy density of high-strength concrete and enhancement of the concrete post-cracking tension capacity induced due to the bond with the reinforcement must be represented in the simplified bilinear tension stiffening model.

Based on the recommended continuous tension stiffening model, a parametric study was carried out to demonstrate the sensitivity of the material model to the seperate material parameters and to examine the behaviour of reinforced high-strength concrete slabs subjected simultaneously to the axial in-plane loads and lateral loads through a loading stub-column with various slab boundary conditions.

It has been found that the post-cracking behaviour of high-strength concrete has a significant effect on the entire load-deflection response. Adequate numerical predictions were achieved only with the incorporation of the realistic stres-displacement characteristics (including strain softening behaviour) of high-strength concrete in both tension and compression. In order to achieve accurate numerical predictions, the realistic yielding strength of steel reinforcement and concrete cover should also be correctly represented in the finite element model.

The effects of edge restraints were significant. The ultimate strength capacity of high-strength concrete slabs was more efficiently improved and ductility was more

severely reduced by the implementation of rotational edge restraints than in-plane translational edge restraints. Proper representation of lateral loading stub-column was also important, which improves both load carrying capacity and ductility of the slab analyzed.

In the case of slabs subjected simultaneously to axial and lateral loads, the membrane compressive stress introduced by in-plane load severely reduces the ductility of the slabs, resulting into a brittle failure. The lateral load carrying capacity was improved with the increase of the in-plane load magnitude for the thick slab analysed.

It is also observed that the loading history has significant effect on slab behaviour. Prior application of small amount of in-plane load leads to approximately the same load capacity as achieved with the prior application of lateral load. Both lateral load capacity and ductility of the thick slab analysed were improved when lateral and in-plane axial loads are applied proportionally. However, the ductility was significantly reduced with application of the in-plane loads, regardless of loading sequence, when compared to that of the slab under the lateral load alone.

Chapter 8

Conclusions

8.1 Experimental study on the tensile behaviour of high-strength concrete

The behaviour of high-strength concrete was experimentally studied under the direct uniaxial tension, flexural tension and cylinder splitting tension. The drawn conclusions from the present experimental work are listed as follows:

1. High-strength concrete exhibits an appreciable post-cracking resistance under direct tension. The descending branch of the complete stress-cracking strain curve is due to the reduction of the effective tensile area and bridging of cracked surfaces through the interaction of aggregates and fibrous crystals. The concrete post-peak softening response is related to widening of a single crack developed across the section.

2. Cracking occurs at the weakest part and spreads gradually across the critical section. After cracking, the cracking strains increase sharply, while the strains on the other parts away from the cracking zone decrease as load decreases. The average cracking deformation along the critical notched section, recorded by 25

mm gage length extensometer, is used throughout this study.

3. The initial modulus of elasticity of high-strength concrete in tension is high, with a mean value of about 50.0×10^3 kN/mm^2, due to the brittle nature of high-strength concrete. The relatively severe nonlinearity of the ascending branch of the average stress-strain curve of high-strength concrete in tension beyond the elastic limit is observed, as indicated by the ratio of the initial modulus to the secant modulus at peak stress.

4. In general, the strain at peak stress (ϵ_{to}) increases proportionally to the tensile strength. The measured values are between 100.5-136.9 $\mu\epsilon$. The recorded tensile strains are more scattered than measured tensile strengths. The tensile strength of high-strength concrete in direct tension is measured to be approximately equal to $5.0\% f'_c$.

5. The developed testing scheme is capable of performing the required tests and yielding a complete stress-cracking deformation response of high-strength concrete in direct tension.

6. Several existing prediction equations for modelling the tension softening response of normal strength concrete are evaluated against the test results of high-strength concrete. Based on the test evidence, a realistic constitutive relationship is recommended for plain high-strength concrete under direct uniaxial tension (Eqs. 4.7 and 4.8).

7. High-strength concrete is a more brittle and stiffer material, with a larger initial modulus of elasticity, compared to normal strength concrete. After the

peak load, the stress-deformation curve of high-strength concrete descends more sharply than that of normal strength concrete. The estimated value of fracture energy density of high-strength concrete is equal to about 5 times the area under the ascending portion of complete stress-strain diagram, while the corresponding value for normal strength concrete increases to 10 times the area under the ascending portion of normal strength concrete stress-strain curve.

8. High-strength concrete is relatively weaker in tension, compared to normal strength concrete. In general, the tensile strength, initial modulus of elasticity and the tensile strain at peak stress increase as the compressive strength increases. However, the tensile strength increases at a much smaller rate as the compressive strength increases. The tensile strength is about 8.0% f_c' for normal strength concrete, while this value decreases to about 5.0% f_c' for high-strength concrete.

9. The measured modulus of rupture (f_r') and splitting tensile strength (f_{ct}') are about 50% and 30% higher than the measured direct tensile strength. As experimentally observed, only the direct tension test could provide the complete stress-deformation diagram in tension beyond the elastic behaviour. All the specimens in both modulus of rupture and splitting tests result in a sudden failure.

10. The empirical formulae for the predictions of f_{ct}' and f_r', as recommended by the ACI Committee 363 (1992), provided a good agreement with test measurments.

11. Low ocean water temperature has severe adverse effect on the f_{ct}' and f_r' of high-strength concrete cured for one day only at room temperature.

8.2 Finite element analysis of high-strength concrete slabs

Based on the good agreement of the model predictions to the experimental results of fourteen high-strength and two normal strength concrete slabs, it is concluded that the formulated F.E. numerical model with an incremental elastic-plastic concrete model implemented in the context of the 8-node quadrilateral shear-flexible shell element can adequately model the thick high-strength concrete slabs with relatively heavy reinforcement and can be used with confidence to predict the behaviour of such slabs with respect to the entire load-deflection response, ultimate load carrying capacity, ductility, and failure mode. The following conclusions are deduced from the present F.E. analysis:

1. The post-cracking behaviour of high-strength concrete has a significant effect on the entire load-deflection response of its slabs. A rational tension stiffening model is recommended, based on the fracture energy concept and comparison of F.E. predictions to experimental results of reinforced high-strength concrete slabs (Eqs. 7.5 and 7.6). For the sake of simplicity, a bilinear tension stiffening model is also proposed.

2. Adequate numerical predictions are achieved only with the incorporation of the realistic stress-displacement characteristics of high-strength concrete in both tension and compression, including strain softening behaviour. The basic mechanical properties employed in analysis are: the tensile strength f'_t=5.0% f'_c; the tensile strain at peak ϵ_{to}=120 $\mu\epsilon$; the compressive strain at peak ϵ_{co}=3000 $\mu\epsilon$; the ultimate compressive strain ϵ_{cu}=3400 $\mu\epsilon$.

3. The realistic yielding strength of rebar and its location should be correctly represented, in order to achieve accurate numerical predictions.

4. The effects of edge restraints are significant. Free uplift along four slab edges must be properly modelled. The ultimate strength capacity of high-strength concrete slabs is more efficiently improved and ductility is more severely reduced by the implementation of rotational edge restraints than in-plane translational edge restraints.

5. Proper representation of the lateral loading stub-column improves both load carrying capacity and ductility of the slab analyzed.

6. In the case of slabs subjected simultaneously to axial and lateral loads, the membrane compressive stress introduced by in-plane load severely reduces the ductility of the slabs, resulting into a brittle failure.

7. The lateral load carrying capacity is improved with the increase of the in-plane load magnitude for the thick slab analysed.

8. The loading history has significant effect on slab behaviour. Prior application of small amount of in-plane load leads to approximately the same load capacity as achieved with the prior application of lateral load. Both lateral load capacity and ductility of the thick slab analysed are improved when lateral and in-plane axial loads are applied proportionally. However, the ductility is significantly reduced with application of the in-plane loads, regardless of loading sequence, when compared to that of the slab under the lateral load alone.

References

- ACI Committee 363 (1992). "State-of-the-Art Report on High-Strength Concrete," ACI 363R-92, American Concrete Institute, 55 p.

- ACI (1985). "Guide for Design and Construction of Fixed Offshore Structures," ACI Committee 357, American Concrete Institute, Detroit.

- ACI (1989). "Building Code Requirement for Reinforced Concrete," ACI 318-89, American Concrete Institute, Detroit.

- ASCE (1982). "Finite Element Analysis of Reinforced Concrete," American Society of Civil Engineers, New York, 553 p.

- Bazant, Z.P., and Kim, S.S. (1979). "Plastic-Fracturing Theory for Concrete," Journal of Engineering Mechanics Division, Proceedings, ASCE, V. 105, pp. 407-428.

- Bazant, Z. P., and Oh, B. H. (1983). "Crack Band Theory for Fracture of Concrete," Materials and Structures, RILEM, 16(93), pp. 155-177.

- Bazant, Z. P., and Oh, B. H. (1984). "Deformation of Progressively Cracking Reinforced Concrete Beams," J. Am. Concr. Inst., 81(3), pp. 268-278.

- Bergan, P. G., and Holand, I. (1979). "Nonlinear Finite Element Analysis of Concrete Structures," Computer Meth. in App. Mech. and Eng., 17/18, pp. 443-467.

- Blick, R.L. (1973). "Some Factors Influencing High-Strength Concrete," Modern Concrete, Vol. 36, No. 12, pp. 38-41.

- Branson, D.E. (1977). "Deformation of Concrete structures," McGraw-Hill, New York.

- Broms, Bengt B. (1965) "Crack Width and Crack Spacing in Reinforced Concrete Members," ACI Journal, Proceedings V. 62, No. 10, pp. 1237-1256.

- BSI BS8110 (1985). "The Structural Use of Concrete, Parts 1 and 2," British Standard Institution, London.

- Cammaert, A.B., and Muggeridge, D.B. (1988). "Ice Interaction with Offshore Structures," Van Nostrand Reinhold, New York, 432 p.

- Carreira, D. J., and Chu, K. H. (1986). "Stress-Strain Relationship of Reinforced Concrete in Tension," ACI Journal, Vol. 83, No. 3, pp. 21-28.

- CEB Model Code for Concrete Structures (1986). "International recommendations," 3rd ed. Cement and Concrete Association, London, 348 p.

- Chen, W.F. (1982). "Plasticity in Reinforced Concrete," McGraw-Hill, New York, 474 p.

- Chen, A.C., and Chen, W.F. (1975). "Constitutive Relations for Concrete," Journal of the Engineering Mechanics Division, ASCE, Vol. 101, No. EM4, pp. 465-481.

- Chen, W.F., and Ting, C. (1980). "Constitutive Models for Concrete Structures," Journal of the Engineering Mechanics Division, ASCE, Vol. 106, No. EM1, pp.

1-19.

- Clark, L.A., and Speirs, D.M. (1978). "Tension Stiffening in Reinforced Concrete Beams and Slabs under Short-Term Load," Technical Report 42.521, Cement and Concrete Association, London, 19 p.

- Cope, R.J. (1986). "Nonlinear Analysis of Reinforced Concrete Slabs," In: "Computational Modelling of Reinforced Concrete Structures," edited by E. Hinton, R. Owen, Pineridge Press, Swansea, U.K., pp. 3-43.

- Cope, R. J. (1984). "Material Modelling of Real, Reinforced Concrete Slabs," In: "Computer-Aided Analysis and Design of Concrete Structures," edited by F. Damjanic, E. Hinton, D. R. J. Owen, N. Bicanic, and V. Simovic, Pineridge Press, Swansea, U.K., pp. 85-117.

- Cope, R.J., Rao, P.V., and Clark, L.A. (1979). "Nonlinear Design of Concrete Bridge Slabs Using Finite Element Procedures," In: "Nonlinear Design of Concrete Structures," Edited by M.Z. Cohn, University of Waterloo, Canada, pp. 379-407.

- Cope, R.J., Rao, P.V., Clark, L.A., and Norris, P. (1979). "Modelling of Reinforced Concrete Behaviour for Finite Element Analysis of Bridge Slabs," In: "Numerical Methods for Non-linear Problems," edited by C. Taylor, E. Hinton, and R. Owen, Pineridge Press, Swansea, U.K., pp. 457-470.

- Crisfield, M.A. (1982a). "Local Instabilities in the Non-linear Analysis of Reinforced Concrete Beams and Slabs," Proc. Instn Civ. Engrs., 73(2), pp. 135-145.

- Crisfield, M.A. (1982b). "Accelerated Solution Techniques and Concrete Cracking," Computer Methods in Applied Mechanics and Engineering, Vol. 33, North-Holland Publ. Company, pp. 585-606.

- Damjanic, F. (1983). "Reinforced Concrete Failure Prediction under Both Static and Transient Conditions," PhD Thesis, University of Wales, Swansea.

- Damjanic, F., Owen, D. R. J. (1984). "Practical Considerations for Modelling of Post-Cracking Concrete Behaviour for Finite Element Analysis of Reinforced Concrete Structures," In: "Computer-Aided Analysis and Design of Concrete Structures," edited by N. Bicanic, and V. Simovic, Pineridge Press, Swansea, U.K., pp. 693-706.

- Darwin, D., and Pecknold, D.A. (1976). "Analysis of RC Shear Panels Under Cyclic Loading," J. Struc. Eng., ASCE, Vol. 102, No. ST2, pp. 355-369.

- Dewar, J. D. (1964). "The Indirect Tensile Strength of Concretes of High Compressive Strength," Technical Report No. 42.377, Cement and Concrete Association, Wexham Springs, 12 p.

- Evans, R.H., and Marathe, M.S. (1968). "Microcracking and Stress-Strain Curves for Concrete in Tension," Material and Structures, Research and Testing (RILEM, Paris), V. 1, No. 1, pp. 61-64.

- Floegl, H., and Mang, H. (1982). "Tension Stiffening Concept Based on Bond Slip." Journal of the Structural Division, ASCE, V. 108, ST12, pp. 2681-2701.

- Floegl, H., and Mang, H. (1981). "On Tension Stiffening in Cracked Reinforced Concrete Slabs and Shells Considering Geometric and Physical Nonlinearity,"

Ingenieur-Archiv, V. 51, No. 3-4, pp. 212-215.

- Franklin, H.A. (1970). "Nonlinear Analysis of Reinforced Concrete Frames and Panels," PhD Thesis, University of California at Berkeley, Ca., U.S.A.

- Gerstle, W., Ingraffea, A.R., and Gergely, P. (1982). "Tension Stiffening: A Fracture Mechanics Approach," In: "Bond in Concrete," Edited by P. Bartos, Applied Science Publishers Ltd., London, pp. 97-106.

- Gerwick, B.C. (1976). "Prestressed Concrete Ocean Structures and Ships," Magazine of Concrete Research, Vol. 28, 54 p.

- Gilbert, R.J., and Warner, R.F. (1978). "Tension Stiffening in Reinforced Concrete Structures," Journal of Structural Division, ASCE, V. 104, ST12, pp. 1885-1900.

- Gjorv, O.E. (1971). "Long-Time Durability of Concrete in Sea Water," Journal of the American Concrete Institute, Vol. 68, pp. 60-67.

- Gopalaratnam, V.S., and Shah, Surendra P. (1985). "Softening Response of Plain concrete in Direct Tension," ACI Journal, Proceedings V. 82, No. 3, pp. 310-323.

- Goto, Y., and Otsuka, K. (1979). "Experimental studies on Cracks Formed in Concrete Around Deformed Tension Bars," Technology Reports of the Tohoku University, V. 44, No. 1, pp. 49-83.

- Guo, Z.-H., and Zhang, X.-Q. (1987). "Investigation of Complete Stress-Deformation Curves for Concrete in Tension," ACI Material Journal, Vol. 84, No. 4, pp. 278-285.

- Haug, A.K., and Sandvik, M. (1988). "Mix Design and Strength Data for Concrete Platforms in the North Sea," ACI SP-109, Concrete in Marine Environment, American Concrete Institute, Detroit, pp. 896-906.

- Hibbitt, H.D., *et al.* (1989). *Theory Manual, ABAQUS*, HSK Corporation, Providence, R.I.

- Hillerborg, A. (1985a). "Numerical Methods to Simulate softening and Fracture of Concrete," In: Sih, D. G. and Ditommaso, A., "Fracture Mechanics of Concrete," Martinus Nijhoff Publ, Dordrecht, The Netherlands, pp. 141-170.

- Hillerborg, A. (1985b). "The Theoretical Basis of a Method to Determine the Fracture Energy G_f of Concrete, Materials and Structures, RELIM, 18(106), pp. 291-296.

- Hillerborg, A., Modeer, M., and Petersson, P.E. (1976). "Analysis of Crack Formation and Crack Growth in Concrete by means of Fracture Mechanics and Finite elements," Cement and Concrete Research, V. 6, pp. 773-782.

- Hinton, E., Abdel Rahman, H. H., and Zienkiewicz. O. C. (1981). "Computational Strategies for Reinforced Concrete Slab Systems," In: "Advanced Mechanics of Reinforced Concrete," IABSE, Delft, pp. 303-313.

- Hoff, C.G. (1985). "The Challenge of Offshore Concrete Structures," Concrete International, Vol. 7, No. 8, pp. 12-22.

- Hughes, B.P., and Chapman, G.P. (1966). "The Complete Stress-Strain Curve for Concrete in Direct Tension," RILEM Bulletin (Paris), New Series No. 30, pp. 95-97.

- Kaplan, M.F. (1961). "Crack Propagation and the Fracture of Concrete," ACI Journal, Vol. 58, No. 5, pp. 591-610.

- Kulicki, J. H., Kostem, C. N. (1972). "The Inelastic Analysis of Reinforced and Prestressed Concrete Beams," Lehigh University Fritz Eng. Lab. Rep. 378B.1, Bethleham, Pa.

- Kupfer, H.B., and Gerstle, K.H. (1973). "Behaviour of Concrete Under Biaxial stresses," Journal of Engineering Mechanics Division, Proceedings, ASCE, V. 99, No. EM4, pp. 852-866.

- Kupfer, H.B., Hilsdorf, H.K., and Rusch, H., "Behaviour of Concrete under Biaxial Stresses," ACI Journal, Proceedings V. 66, No. 4, Aug. 1969, pp. 656-666.

- Lin, C. S., and Scordelis, A. C. (1975). "Nonlinear Analysis of RC Shells of General Form," J. Strct. Div., ASCE, 101(ST3), pp. 523-538.

- Maeda, Y., Matsui, S., and Kojima, I. (1976). "Nonlinear Analysis of Reinforced Concrete Slabs by Finite Element Method," Technology Reports of the Osaka University, 26(1333), Faculty of Engineering, Osaka University, pp. 595-604.

- Marzouk, H.M., and Hussein, A. (1990). "Properties of High-Strength Concrete at Low Temperature," ACI Material Journal, V. 87, No. 2, pp. 167-171.

- Marzouk, H., and Hussein, A. (1991). "Experimental Investigation of High-Strength Concrete Slabs," ACI Structural Journal, Proceedings V. 88, No. 6, pp. 701-713.

- Massicotte, B., Elwi, A. E., and MacGregor, J. G. (1990). "Tension Stiffening Model for Planar Reinforced Concrete Members," J. Struc. Eng., ASCE, Vol. 116, No. 11, pp. 3039-3058.

- Massicotte, B., MacGregor, J.G., and Elwi, A.E. (1989). "Behaviour of Concrete Panels Subjected to Axial and Lateral Loads," Journal of Structural Engineering, ASCE, V. 116, No. 9, pp. 2324-2343.

- Mather, K. (1980). "Concrete Weathering at Treat Island, Maine," SP-65 Concrete in Marine Environment, American Concrete Institute, Detroit, pp. 101-112.

- Mazars, J. (1981). "Mechanical Damage and Fracture of Concrete Structures," Advances in Fracture Research, V. 4, ICFS, Cannes, pp. 1499-1506.

- Mehta, P.K. (1980). "Durability of Concrete in Marine Environment - A Review," SP-65 Concrete in Marine Environment, American Concrete Institute, Detroit, pp. 1-20.

- Mobil Oil Canada Ltd. (1985). "Hibernia Development Project, Environmental Impact Statement," St. John's, Canada.

- Naaman, A.E., and Homrich J.R. (1989). "Tensile Stress-Strain Properties of SIFCON," ACI Material Journal, Vol. 86, No. 3, pp. 244-251.

- Neville, A.M. (1973). "Properties of Concrete," 2nd Edition, John Willey and Sons, New York, 686 p.

- Ngo, D., and Scordelis, A.C. (1967). "Finite Element Analysis of Reinforced Concrete Beams," ACI Journal, Proceedings V. 64, No. 3, pp. 152-163.

- Nilson, A.H. (1968). "Nonlinear Analysis of Reinforced Concrete by the Finite Element Method," ACI Journal, Vol. 65, No. 55, pp. 757-766.

- Parrot, L.J. (1969). "The Properties of High-Strength Concrete," Technical Report No. 42.417, Cement and Concrete Association, Wexham Springs, 12 p.

- Petersson, P. (1981). "Crack Growth and Development of Fracture zones in Plain Concrete and Similar Materials," Report No. TVBM-1006, Lund Institute of Technology, 174 p.

- Phillips, D.V., and Zienkiewicz, O.C. (1976). "Finite Element Non-linear Analysis of Concrete Structures," Proc. Instn Civ. Engrs., V. 61, No. 2, pp. 59-88.

- Prakhya, G.K.V. and Morley, C.T. (1990). "Tension-Stiffening and Moment-Curvature Relations of Reinforced Concrete Elements, American Concrete Institute, Structural Journal, V. 87, No. 5, pp. 597-605.

- Price, Walter H. (1951). "Factors Influencing Concrete Strength," ACI Journal, Proceedings V. 47, No. 6, pp. 417-432.

- Rashid, Y.R. (1968). "Analysis of Prestressed Concrete Presure Vessels," Nuclear Engineering and Design, V. 7, No. 4, pp. 334-355.

- Rots, J.G., Nauta, P., and Kusters, G.M.A. (1985). "Smeared Crack Approach and Fracture Localization in Concrete," Heron, V. 30, No. 1, 48 pp.

- Saucier, K.L., Tynes, W.O., and Smith, E.F. (1965). "High-Compressive-Strength Concrete Report—Report 3, Summary Report," Miscellaneous Paper No. 6-520, U.S. Army Engineer Waterways Experiment Station, Vicksburg, 87 p.

- Scanlon, A. (1972)."Time Dependent Deflections of Reinforced Concrete Slabs," PhD Thesis, University of Alberta, Edmonton, Canada.

- Schnobrich, W.C. (1977). "Behaviours of Reinforced Concrete Structures Predicted by the Finite Element Method," Computers and Structures, V. 7, pp. 365-376.

- Scordelis, A.C. (1978). "Finite Element Modelling of Reinforced Concrete Structures," Symposium on analysis of Reinforced Concrete Structures by the Finite Element Method, Politecnico di Milano.

- Suidan, M., and Schnobrich, W.C. (1973). "Finite Element Analysis of Reinforced Concrete," Journal of the Structural Division, ASCE, Vol. 99, No. ST10, pp. 2109-2123.

- Tasuji, M.E., Slate, F.O., and Nilson, A.H. (1978). "Stress-Strain Response and Fracture of Concrete in Biaxial Loading," ACI Journal, Proceedings V. 75, No. 7, pp. 306-312.

- Terrien, M. (1982). "Acoustic Emission and Post Critical Mechanical Behaviour of Concrete in Tension," Bulletin de Liaison des LPS (Paris), No. 105, pp. 65-72. (in French)

- William, A. (1986). "Tests on Large Reinforced Concrete Elements Subjected to Direct Tension," Technical Report 562, Cement and Concrete Association, London, 56 p.

- Yankelevsky, D.Z., and Reinhardt, H.W. (1987). "Response of Plain Concrete to Cyclic Tension," ACI Material Journal, Proceedings V.84, No. 5, pp. 365-373.

• Yuzugullu, O., and Schnobrich, W.C. (1973). "A Numerical Procedure for the Determination of the Behaviour of a Shear Wall Frame System," ACI Journal, Vol. 70, No. 7, pp. 474-479.